Investigation of Meson Production at COSY-TOF Using the Analysis Framework TofRoot

Dissertation
zur Erlangung des akademischen Grades
Dr.rer.nat.

vorgelegt von

Martin Schulte-Wissermann

geboren in Mainz

Institut für Kern- und Teilchenphysik
Fachrichtung Physik
Fakultät Mathematik und Naturwissenschaften
der Technischen Universität Dresden

2004

1. Gutachter : Prof. Dr. H. Freiesleben

2. Gutachter : Prof. Dr. B. Spaan

3. Gutachter : Prof. Dr. S. Marcello

Datum des Einreichens der Arbeit : 26. 3. 2004

Datum der Verteidigung der Arbeit : 14. 7. 2004

Kurzfassung

Das TOF-Spektrometer am Protonen-Beschleunigerring COSY (Jülich) besticht durch seine experimentelle Vielseitigkeit, da der modulare Aufbau aus ca. zehn Subdetektoren eine individuelle Anpassung an spezifische experimentelle Erfordernisse ermöglicht. Diese Flexibilität erschwert jedoch die Kalibrierung und die Datenauswertung, da die Software nach jedem Umbau angepaßt werden muß. Daher wurde das Analyseframework TofRoot entwickelt, welches durch einen Satz von Strategien eine effiziente und teamorientierte Auswertung ermöglicht, sogar für verschiedene Strahlzeiten. Mit Hilfe von TofRoot wurden drei Reaktionskanäle analysiert, jeweils für zwei Strahlimpulse ($2950\,MeV/c$, $3200\,MeV/c$): Zuerst die elastische Proton-Proton Streuung, welche der Luminositätsbestimmung dient und an Hand derer die Güte des Detektorsystems und der Kalibration veranschaulicht wird. Anschließend folgt die Reaktion $pp \rightarrow d\pi^+$, bei der die extrahierten Winkelverteilungen und totalen Wirkungsquerschnitte sich widerspruchsfrei in die vorhandene Datenbasis einordnen. Schließlich wird die Vektormesonenproduktion ($pp \rightarrow pp\omega$) untersucht, die den wissenschaftlichen Fokus dieser Arbeit darstellt. In diesem Kanal ist die experimentelle Datenbasis dünn und die theoretische Beschreibung bislang unvollständig. Ein gutes Verständnis der ω-Produktionsdynamik ist aber unabdingbar für die theoretische Beschreibung vieler Felder moderner Physik, z.B. des kurzreichweitigen Teils der Nukleon-Nukleon-Wechselwirkung, extrem dichter Materie und des Strangenessanteils im Nukleon. Nach einer detailierten Beschreibung der Analysestrategien werden totale Wirkungsquerschnitte, Winkelverteilungen und Spektren invarianter Massen vorgestellt. Verglichen mit vorhandenen Daten sind alle Angaben mit kleineren experimentellen Unsicherheiten behaftet, und zum Teil erschließen sie zuvor nicht zugängliche Größen. Abschließend werden die Ergebnisse in die vorhandene experimentelle Datenbasis eingeordnet, und ihre Auswirkung auf theoretische Modelle wird diskutiert.

Abstract

The TOF-spectrometer located at the proton accelerator COSY (Jülich) stands out for experimental versatility. This is due to its modular setup: about ten subdetectors can be be arranged to satisfy the individual requirements of specific experiments. However, this flexibility hampers the calibration and the data analysis, since for each new detector setup the software has to be adjusted as well. Therefore, a new analysis framework (TofRoot) has been developed. A set of concepts is used that enables teamwork and leads to an efficient data-analysis, even for different beamtimes. Using TofRoot, three reactions are analyzed - each for two different beam momenta ($2950\,MeV/c$, $3200\,MeV/c$): Firstly, the elastic proton-proton scattering. It is used to determine the luminosity and to extract benchmark results for the detector performance. Secondly, the reaction $pp \rightarrow d\pi^+$is studied. Total as well as differential cross sections are presented, which nicely fit into the word data set. Finally, the vector-meson production ($pp \rightarrow pp\omega$) is investigated which is the main focus of this work. Here, the theoretical and experimental knowledge is presently rather scarce. However, the elementary reaction dynamics is needed as an inevitable prerequisite in many fields of physics; e.g. the short range part of the nucleon-nucleon force, the description of extremely dense matter, the strangeness content of nucleons. After a detailed description of the analysis strategies, total cross sections, angular distributions, and invariant-mass spectra are presented. Some of the findings are completely new, and all provide smaller experimental uncertainties with respect to the available word data set. Finally, the results are embedded into the existing body of data and their implication on the theoretical models is discussed.

Contents

Chapter 1

Introduction

In classical physics, the *observables* such as force, temperature, and length always are of collective nature, i.e. they result though the collective interaction of many individual particles. And, although the actual behavior of each constituent is unknown, (classical) theory describes our macroscopic world rather well. If we observe smaller scales, which through the uncertainty principle are directly related to higher involved energies, we notice that matter is composed of molecules, molecules are composed of atoms, atoms are composed of nuclei and electrons. At this scale, a new concept of physics, *quantum mechanics*, is necessary to describe the observed systems. Today, electrons are believed to be *elementary* particles, i.e. that they are point-like and without an internal structure. In contrast to the electrons, we find that nuclei are not elementary, but composed of nucleons. Finally, examining nature even closer, also nucleons are not elementary: They are composed of quarks. Today, the quarks are considered "fundamental", but whether nature hides even smaller constituents is still unknown.

It is important to realize that the theoretical description of each energy range is conclusive and necessary in its own realm: molecular physics is not at all obsolete through the description of the interactions between nucleons; nuclear models are not replaced with QCD. Quite the contrary, modern physics, up to now, fails to provide a unique and all-describing theory.

1.1 Conceptual and Theoretical Overview

The development of theoretical physics always proceeds hand in hand with the experimental potentialities, which had been subject to a continuing revolution in past. This led to the fields of *nuclear physics* in the first, and *high-energy physics* in the second half of the last century. While one aim in contemporary physics is to push the energy frontier even further, another approach is to look into the existing picture in more detail. Therefore, today, a new field of physics examines the "transition region" between high-energy and nuclear physics in detail: *medium-energy physics*[1].

The conceptual differences and the theoretical approaches of these three fields of

---

[1] Synonymous to *medium energy physics* is *intermediate-energy physics* and *hadron physics*. In addition, the expression *nuclear physics* is used, although the energies involved are far above the "nuclear energy scale".

modern physics will be briefly sketched in the following.

1.1.1 High-Energy Physics

One definition of "high-energy physics" is that it reflects the physics at the highest accessible energies. This, of course, is strongly correlated to the state-of-the-art equipment, and therefore changes with time. In a sense, the Rutherford experiment was "high-energy physics", but for 1915. Today, high-energy physics can also be defined as "the physics of the *elementary particles*", hence (elementary) particle physics.

In high-energy physics the (relativistic) **Q**uantum **C**hromo **D**ynamics ((r)QCD), at present, is the appropriate theory of the strong interaction. It has achieved impressive results in the description of the dynamics at high energies (momentum transfer $|q|^2 > 10^2\,GeV^2$).

The fundamental (fermionic) constituents in QCD are called quarks. They are grouped in three families, with two members each: **u**p, **d**own; **c**harm, **s**trange; **t**op, **b**ottom. To each of these six quarks also the *anti-particle* ($\overline{u}, \overline{d}; ...$) exists, which results in twelve fundamental constituents of QCD. The quarks carry as an additional quantum number the color-charge (red, green, blue, anti-red, anti-green, anti-blue). The interaction between quarks is mediated by the exchange bosons of QCD, the *gluons*. The strength of the resulting (attractive) force caused by the gluons is *increasing* rapidly with the distance of the interaction: The quarks are glued together. This effect is called *confinement*, and is fundamentally responsible for the existence of hadronic matter. The postulate that matter can only be *color-neutral*, restricts the hadron matter to consist of either two quarks (*mesons*, color and anti-color), or of three quarks (*baryons*, red-green-blue). These two species are the building blocks of the (established, hadronic) particle zoo. More complex (theoretically permitted) color-neutral bound states, such as penta-quarks and glue-balls are under heavy experimental and theoretical investigation.

Contrary to the confinement, the binding force between quarks diminishes at small distances (high energies ↔ high momentum transfer). This effect is called asymptotic freedom and leads to a somewhat paradox situation: QCD describes the physics of quarks better the higher the energy of the participating quarks are chosen, and worse, if the energy is small. In fact, one focus of contemporary theory in high-energy physics is to extend the models towards smaller energies.

1.1.2 Nuclear Physics

Frankly put, nuclear physics is the physics of nuclei. Nuclei are composed of nucleons which are bound within a collective potential. This potential is of hadronic nature and is caused by the collective interactions of the nucleons themselves[2]. As an upper energy limit for the scope of nuclear physics the typical binding energies of nucleons in nuclei can be defined. This leads to an energy region up to a few MeV per participating nucleon. At these energies confinement is too strong and the participating wavelengths are too large for quark properties to be visible. The nucleons within a nucleus as well

---

[2] Sometimes denoted as *van der Waals interaction of the hadronic force*, although it rather should be considered to resemble a covalent binding.

as free nucleons behave rather as single particles, i.e. as if they would be themselves "fundamental". However, these "particles" can not be imagined as *bullets* with a certain position (x) and momentum (p) as in classical physics. According to the Heisenberg uncertainty principle:

$$\Delta x \Delta p_x \geq \frac{\hbar}{2}. \tag{1.1}$$

a better knowledge of the position x will diminish the knowledge of the momentum p, and vice versa ($\hbar$ is Planck's constant, and x, p_x can represent any spatial direction). The "particle" properties are rather described by the *mean* values ($\overline{x}, \overline{p}_x$) and the *widths* ($\Delta x, \Delta p$). This leads to the concept of describing particles as waves, or better as *wave packets.* Normally these wave packets (particles) are not free; they interact with their surroundings. This is usually the potential of a nucleus or an external field. The concept of "wave packets in a potential" can be expressed by the Schrödinger equation, which is the theoretical backbone of nuclear physics:

$$-\frac{\hbar^2}{2m}\,\frac{d^2\psi(x)}{dx^2} + V(x)\psi(x) = E\psi(x). \tag{1.2}$$

Here, $\psi(x)$ is the Schrödinger wave function, $V(x)$ a parameterized potential and E the energy of the system. In any practical case, the function $\psi(x)$ has to obey certain boundary conditions, which leads to the general road-map of describing physical phenomena in nuclear physics: given a potential $V(x)$, find a solution to Eq. 1.2 which for $\psi(x)$ and its first derivative $d\psi/dx$ is continuous across any boundary condition. In case of bound states, this equation will in general have solutions only for certain energies E - the *energy eigenstates.*

During the last 80 years this concept has led to extraordinary results in many fields of nuclear physics: e.g. alpha-decay of heavy nuclei, nuclear potentials, description of the deuteron, energy levels of nuclei. Nevertheless, the field of nuclear physics keeps being inspired by many phenomenological approaches, and the description of all nuclear properties "from first principles" is far from being clarified ([May84],[Kra88],[Leo94],[Bet96]).

If we increase the involved energies, Eq. 1.2 fails to appropriately describe the observed physics. This has three main reasons. Firstly, the Schrödinger equation is *non-relativistic*, i.e. it does not incorporate the phenomena arising from particles moving at velocities near the speed of light. Secondly, the number of "particles" is conserved in Eq. 1.2, i.e. this equation provides no means to incorporate the creation of new particles from the energy of the system ($E = mc^2$). Finally, the assumption of a "static" potential is not valid any more - the field itself has to be quantized. Therefore, new theoretical approaches had to be developed in order to extend the description to a higher energy range.

1.1.3 Medium-Energy Physics

Medium-energy physics investigates the phenomena appearing at the intersection between nuclear physics and high-energy physics. The energies are too elevated to be considered nuclear physics ($\approx 1\,\mathrm{GeV}$ compared to some MeV) but still the gap to high-energy physics (10-300 GeV) is broad. The situation can be compared to describing a boiling pot of water: The molecules of the water (nucleons) are still in a defined state, but characteristics of the next “aggregate state” are already visible. Conceptually, the theoretical description of medium-energy physics is fundamentally based on both, nuclear theory and QCD. While, for example, the final state interaction is totally motivated by scattering lengths and hadronic potentials, the OZI-rule and the expectance of sea-quark content ($s\overline{s}$) in the nucleon is ascribed to QCD.

As already postulated by Hideki Yukawa in 1935 [Yuk35], the force between nucleons is transmitted via (virtual) exchange bosons. These bosons were later identified to be *mesons*, where the mass of the mesons (scale of virtuality) governs the distance of interaction: Light pions (π) mediate the long- and medium-distance interactions ($> 0.7 fm$, attractive); heavy mesons (ω, ρ) are responsible for a strong short-range force (repulsive). Mesons not only are the (virtual) mediators of the hadronic force, but they also can materialize (on-shell) in our real world. This leads to (one possible) definition of medium-energy physics: The study of the interaction and the production of hadrons at energies where the reaction partners can be considered to be free and fundamental particles. To achieve a deeper understanding, elastic and inelastic reactions have to be measured, covering as many reactions channels and observables as possible. The observables (total cross sections, angular distributions, spin-observables, Dalitz-plots, invariant mass spectra) have to be measured with high precision by the experiment. Then, theory has to describe the experimental data, giving a comprehensive and consistent picture for virtual and on-shell processes. From this, theory should trigger new experiments predicting physical effects not observed so far.

It is important to notice that the theoretical description is not only important for medium-energy physics itself. In fact, the output is needed in many other fields as a input, e.g. the theoretical models in cosmology and high-energy physics need data on scattering lengths, nuclear resonances, coupling constants and total cross sections as an inevitable prerequisite.

1.2 Experimental Overview

The experimental overview will first briefly cover the field of meson production in general. Some of the accelerator facilities of our time will be sketched as well. After this, focus will lie on the COSY accelerator and the TOF spectrometer. Both devices were used to collect the data presented in this work.

1.2.1 Meson Production in Nucleon-Nucleon Interactions

Meson production has been largely studied in the past using real or virtual photons and in e^+e^- annihilation. Also secondary beams and $p\overline{p}$ annihilation have been used. Since here the projectiles either “vanish” or do not have intrinsic excitation states, the results often are of remarkably high quality. However, “ordinary” matter consists of nucleons only. Therefore only the study of NN-interactions can finally establish the physics of the nucleonic force.

In meson production, we are dealing with large momenta in the entrance channel, but with (very) small momenta in the final meson-baryon system. Therefore, meson production occurs at large momentum transfers, hence probing small distances. Since near threshold only few partial waves contribute, meson production in NN-interactions is an ideal tool to test theoretical models as well as to fix model parameters needed in other fields of physics. However, the experimental and theoretical situation is complicated for inelastic NN-interactions: Firstly, close to the production thresholds the available phase-space is small, yielding small total cross sections. This is a severe obstacle, especially for the observation of heavier mesons well above the (multi) pion threshold. Secondly, as excess energy increases, the nucleons[3] themselves can be excited to nuclear resonances, which opens many possible (intermediate) reaction channels. Finally, at high excess energies many partial waves may contribute, which can severely complicate the theoretical description.

To establish a comprehensive medium-energy theory, high quality measurements are needed, for which two indispensable requirements have to be fulfilled: (1) a detector system with high resolution, and (2) a strong proton beam of low emittance which leads to a high luminosity in the target. The technical development of computer science and detector electronics in the past, allows detectors of sufficient quality today, even with the modest resources of medium-energy physics[4]; and in the last two decades, a new generation of strong focusing synchrotrons have provided high-quality proton beams.

At the beginning of the 1990s, the IUCF[5] [IUCF] revealed a deep lack of understanding in the theoretical description of inelastic NN-interactions. In spite of this, the accelerator was shut down shortly afterwards. The CELSIUS accelerator at the TSL[6] [CELSIUS] reaches a maximum beam momentum of $p_{beam} = 2100\,MeV/c$ which allows measurement up to the η threshold. The detector used (WASA) is of extraordinary quality (4π acceptance, neutral particle detection), but the physical program is severely limited due to the finite beam momentum. Initial studies of the associated strangeness production and of vector meson production were carried out at the SATURNE accelerator located at Sacley. It could provide proton beams well over $3500\,MeV/c$, however it was shut down after December 1997 due to funding difficulties. The most recent machine providing (polarized) proton beams is the COSY accelerator at Jülich. It will be described in more detail in the next paragraph, but it should already be stressed here that COSY, at present, is the *only* facility that enables the study of *nucleon-nucleon* interactions at intermediate energies ($2100\,MeV/c < p_{beam} < 3680\,MeV/c$). The experimental program at COSY today is in the “production phase”, i.e. the frequency of publications is high. Together with the other facilities, a wealth of data has been accumulated during the last decade, which differ to previous measurement with respect to the amount, and the quality, of the data. As an example, the world data on total cross sections for the pseudoscalar mesons is given in Fig. 1.1. While the first measurements aimed at measuring total cross section using unpolarized beams, today, the focus shifts towards more complicated systems, including spin and differential observables; and after covering mainly

---

[3] The target *and* the projectile.

[4] *Modest* compared to the budget and man-power available in high-energy physics.

[5] **I**ndiana **U**niversity **C**yclotron **F**acility

[6] **T**he **S**vedberg **L**aboratory

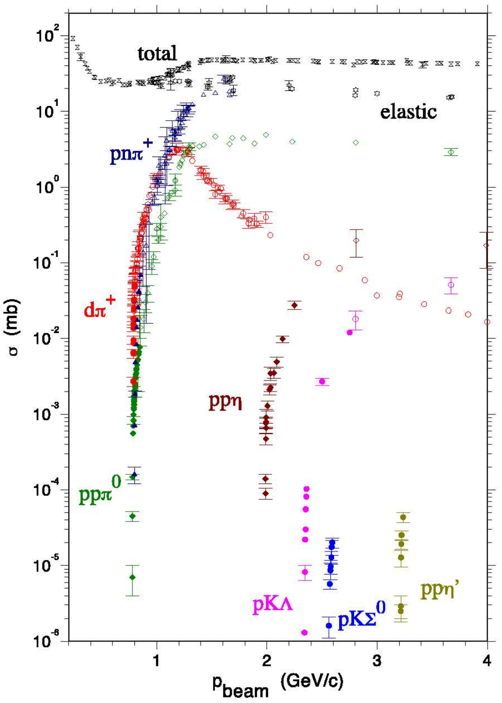

Figure 1.1: *Compilation of total cross sections for (pseudoscalar) meson production near threshold. The open symbols represent older measurements, while the colored symbols are the combined effort achieved at IUCF, CELSIUS and COSY. Directly at threshold, the observed cross sections can be eight orders of magnitude smaller compared to the total reaction cross section.*

(Figure taken from [Mac99].)

the pseudoscalar sector, currently the vector meson production is also an increasing field of interest[7].

The future of medium-energy physics seems to be quite promising as well: The proposed project to extend the GSI facility at Darmstadt is approved and the first planing phase is completed. One of a whole series of new detectors will be the 4π detector PANDA [PANDA]. With more than 10^7 channels it will reach the size of present-day high-energy detectors. First measurements are planned to begin in 2010. Since this is still far in the future, a proposal has been made to install the WASA detector at COSY. This will provide an excellent tool for medium-energy physics, as it would close the gap until, with the advent of the new GSI facility, a new generation of detectors and accelerators will allow an even deeper insight into the nature of hadronic interactions.

1.2.2 The COoler SYnchrotron : COSY

The **Co**oler **Sy**nchrotron COSY (see Fig. 1.2) at the Forschungszentrum Jülich is a storage ring especially designed for the investigation of nucleon-nucleon (NN) interactions [COSY]. Starting operation on the 1^{st} of April 1993 with a proton beam, it presently also accelerates deuterons. The use of light ion beams up to A$\leq$12 is planned. The COSY accelerator is operated with H^- ions pre-accelerated in an isochronous cyclotron. They leave the cyclotron with a kinetic energy of about $40\,MeV$ and are

---

[7] The ω meson production in proton-proton collisions will be covered in the last chapter of this work.

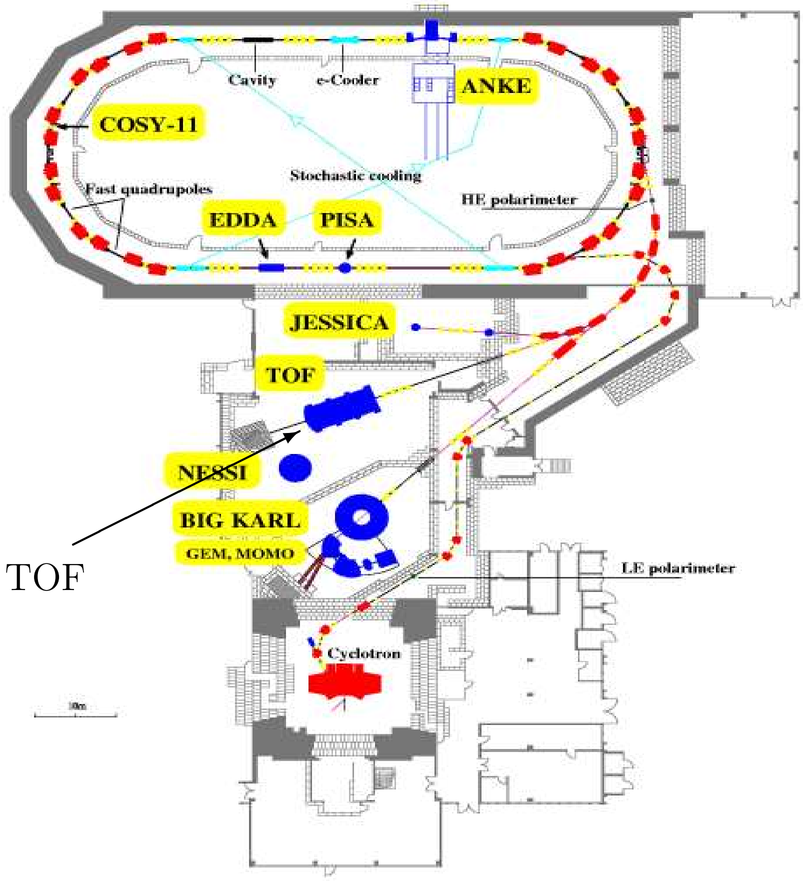

Circumference	184 m
Momentum range	300 - 3500 MeV/c
Acceleration	1 GeV/c per s
Space charge limit	$2 \cdot 10^{11}$ protons
Electron cooling	270 to 645 MeV/c
Stochastic cooling	1.5 to 3.5 GeV/c
Emittance of the beam	1 to 10 π $mm\ mrad$
Momentum resolution	10^{-3} - 10^{-4}

Figure 1.2: *The COSY accelerator at the Forschungszentrum Jülich. After pre-acceleration in the cyclotron the beam is conducted into the main accelerator ring. Stochastic and/or electron-cooling reduces the emittance of the beam. The protons can be utilized in internal or external experiments. Some technical specifications are given [Kil98].*

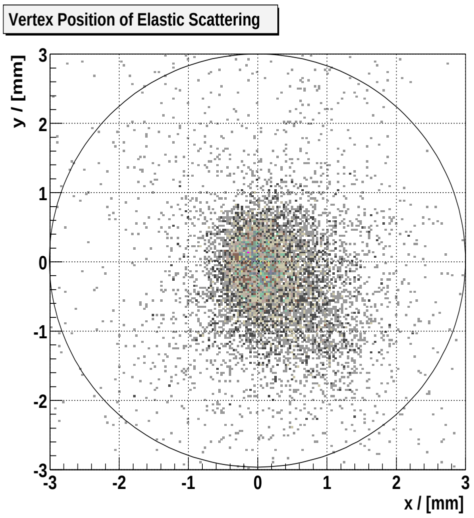

Figure 1.3: *Vertex distribution (x/y) of elastically scattered events measured with the TOF detector. The target (center) was* not *used as additional information in the vertex fit. A convolution of the spatial distribution of the beam and the experimental resolution is shown. Hence, the actual beam is even more narrow and it can truly be considered pencil-like, even after extraction. The smearing at (1,-1) is due to a known effect during the extraction of the beam [Pra01]. The circle represents the diameter of the target (*$6\,mm$*).*

guided via a $100\,m$ long injection beam line to the COSY-ring. Using stripping injection the H^- ions are converted to protons, which then are accelerated (ramp-phase) to momenta of $270MeV/c \leq p \leq 3680MeV/c$. Afterwards the protons either are stored (storing time up to $1h$) for use in one of the internal experiments, or they are extracted to be utilized in external experiments.

While the maximum momentum (COSY-limit) is rather modest compared to high-energy accelerators, the COSY accelerator is outstanding for its excellent beam quality and stability. This is achieved by *cooling* the beam (reducing the size of the phase-space) in two ways. Up to a beam-momentum of 645 MeV/c *electron-cooling* is used, where an electron beam guided in parallel moderates the transversal and longitudinal momenta of the protons. Beyond this value, stochastic cooling initiates: The position of the beam is monitored at one “edge” of the ring, and an electrostatic correction is applied when the beam passes the opposite corner of COSY [Sto98]. Using these techniques, it is possible to achieve a “pencil-like beam” with a diameter $d \leq 1mm$ and an emittance $\varepsilon \leq 1\pi\ mm\ mrad$. The beam distribution after extraction measured with the TOF detector is shown in Fig. 1.3.

The COSY accelerator provides an excellent experimental environment to examine nucleon reactions within excess energies up to $1100\,MeV$ (in the proton-proton frame). This allows the study of nucleon resonances (Δ, N^*), the production of pseudoscalar and vector mesons ($\pi, K, \eta, \rho, \omega, \phi$), multi-pion production as well as the associated strangeness production ($K\overline{K}$ and KY where $Y = \Lambda, \Sigma^{0,+,-}$).

Since 1996, COSY can provide polarized beams as well. This makes it possible to measure asymmetry observables in all the above-mentioned channels. In addition, the use of polarized targets allows to measure polarization-transfer parameters.

1.2.3 The TOF-Spectrometer

The COSY-TOF (**T**ime **O**f **F**light) spectrometer is located as an external experiment outside the COSY accelerator hall. It is a highly modular detector system which

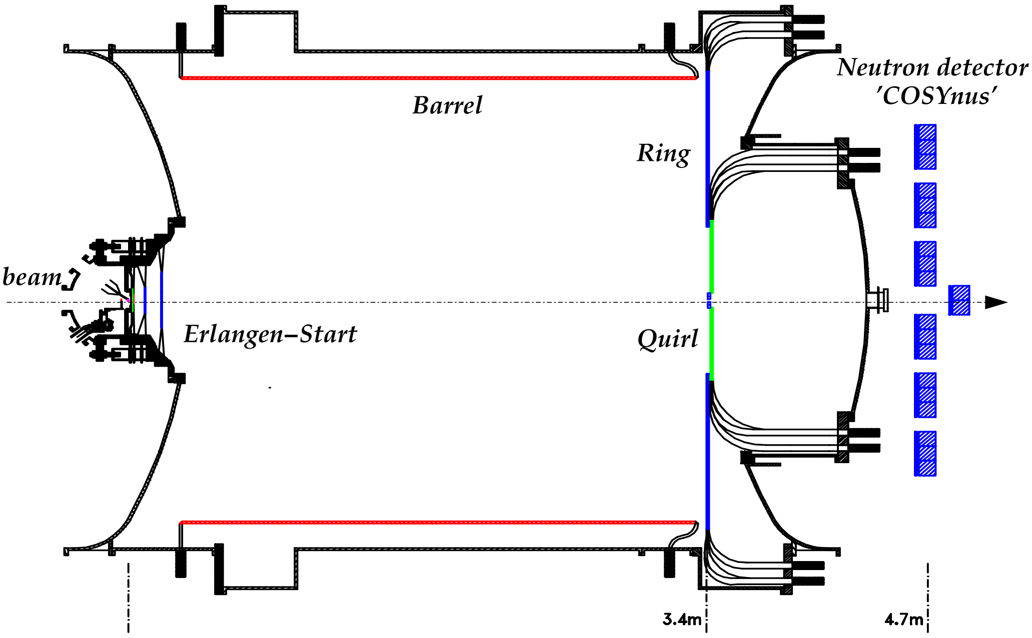

Figure 1.4: *The TOF-spectrometer in the setup of January 2000 (3 m-version). The beam is incident from the left and hits the target (4 mm liquid hydrogen). It then passes through the Erlangen-Start detector which gives a sharp time-signal and also tracking information. (For a detailed picture of the start region please refer to Fig. 4.2.) After a flight-path of ≈ 3 m in vacuum, the particles are detected in the stop detectors (Quirl, Ring, Barrel). No direct particle identification is possible, but the detector rather aims at detecting the full event pattern and therefore allowing a complete kinematical reconstruction. Outside the vacuum vessel the neutron detector COSYnus is placed. The calorimeter is not shown. It was mounted behind the Quirl at the end of 2000.*

stands out for its experimental versatility. The different components (modules, subdetectors) can be assembled according to the specific requirements of an experimental program. This leads to an elevated flexibility, but since the detector setup is different for each beamtime, this of course aggravates the calibration and data analysis.

A view of the detector setup of the January 2000 beamtime, the "3 m-version", is shown in Fig. 1.4. For a detailed picture of the Erlangen-Start-detector system (near target) please refer to Fig. 4.2.

General Technical Requirements for the TOF-Spectrometer

The TOF-spectrometer provides no means to directly determine the four-momentum of a particle[8]. It instead focuses on measuring the velocity vectors of *all*[9] charged reaction ejectiles. In this case, the four-momenta of all participating particles can be

---

[8] Since late 2000 the calorimeter in conjunction with the Quirl-detector provides particle identification for particles below $\vartheta_{lab} = 10^\circ$.

[9] The beam and target information is known → one particle could remain undetected. However, measuring all participating particles allows to apply a kinematic fit.

Detector	Material	Readout	Channels	Softw.Chan.	Group[a]	Installed
Quirl	scinti	tdc&qdc	48+24+24	192	Jül	1995
Ring	scinti	tdc&qdc	96+48+48	384	Jül	1995
Barrel	scinti	tdc&qdc	96+96	384	Ross/DD	1997
Torte	scinti	tdc&qdc	12+12	48	Erl	1995
Microstrip	microstrip	qdc	100+128	228	Erl	1995
Small Hodo	scinti	qdc	96+96	192	Erl	1995
Big Hodo	scinti	qdc(&tdc)	192+192	384(768)	Erl	1998
COSYnus	scinti	tdc&qdc	12+12+4+8	72	DD	1998
Calorimeter	scinti	tdc&qdc	84	168	Tüb	2000
COSY-TOF			1428	2052(2436)		

Table 1.1: *The main COSY-TOF components (sub-detectors).*

[a] Jül = Forschungszentrum Jülich, Ross = Forschungszentrum Rossendorf, DD = Technische Universität Dresden, Erl = Universität Erlangen-Nürnberg, Tüb = Universität Tübingen

assigned using mass hypotheses and energy/momentum conservation. For reaction selection or to improve the output, a kinematic fit can be applied.

This approach is rather different from most experiments in medium-energy physics and leads to specific requirements for the layout of the detector:

- The start/stop sub-detectors must have an optimized time resolution (TOF!).
- All components should be *massless*, i.e. they must be as thin as possible to minimize secondary reactions (small-angle scattering, nuclear reactions, δ-electrons) which lead to a smearing of the tracks or even to the generation of "new" particles participating in the event pattern.
- To detect all particles involved in a reaction, the detector should have an acceptance of preferably 4π in the CMS[10]. Due to the Lorentz factor of the CM in the laboratory frame (boost), for most reactions (especially near threshold) this requirement is fulfilled by covering the forward hemisphere (2π) in the laboratory system.
- Full coverage of the azimuthal angle 2π. This requirement is of paramount importance for experiments which measure polarization.
- Optimized efficiency of all (sub-)detectors near 100%.
- Modular setup ↔ high flexibility.

Detector Components

All (sub-)detectors were designed, optimized, and finally implemented according to the previously stated technical requirements by the collaborating groups[11]. Most

---

[10] **C**enter-of-**M**ass-**S**ystem or **C**enter-of-**M**omentum-**S**ystem: Both can be used synonymously if the relativistic mass/momentum is used ($m_1\vec{\gamma_1} = -m_2\vec{\gamma_2}, \vec{P_1} = -\vec{P_2}$).

[11] IUCF Bloomington (USA), Ruhr-Universität Bochum, Universität Bonn, Technische Universität Dresden, Universität Erlangen-Nürnberg, Forschungszentrum Jülich, Fachhochschule Jülich,

detectors were mounted for the first time between the years 1995 to 1998, although the system never operated with the “full setup” until early 2000. The beamtime of January 2000 and the beamtime series of fall 2002 (including the calorimeter) are so far the experiments with the “most complete” detector.

The main components of the COSY-TOF spectrometer are[12]:

- **The Target:** Optimized for low material. The cylindrical target cell ($r = 3\,mm, l = 4\,mm$) consists of extremely thin material: Main cell, $60\,\mu m$ copper; target windows, $1\,\mu m$ mylar. It is mounted on a $\approx 50\,cm$ target finger with an automated temperature control. It can provide liquid hydrogen as well as liquid deuterium [Jae92][Nake93][Has99].

- **The Start-detector MARS:** Optimized for low material and high time resolution. This start-detector is predominantly used in low-energy experiments ($p_{beam} < 1000 MeV/c$; $pp \rightarrow pp\gamma$, $pp \rightarrow pn\pi^+$, $pp \rightarrow pp\pi^0$). It was not used in the January 2000 beamtime [Mic98].

- **The Erlangen-Start-detector:** Optimized for tracking of charged particles. This start-detector is predominantly used for “high-energy” experiments ($p_{beam} > 1500 MeV/c$) and consists of four sub-detectors: The Torte[13], which gives a (rough) angular and the start time information, is followed by three tracking devices: One double-sided microstrip detector and two double-layer fiber-hodoscopes (see Fig. 4.2) [Wag97].

- **The Quirl:** The Quirl[14] is a detector for position and time information near the beam axis. It consists of three layers of scintillating material and provides pixel information. It covers a angular range from $0.8^\circ < \vartheta < 11^\circ$ ($3\,m$ version) [Dah95].

- **The Ring:** The Ring-detector is constructed in a similar manner as the Quirl. It covers the angular range $11^\circ < \vartheta < 24^\circ$ ($3\,m$ version) [Dah95].

- **The Barrel:** The Barrel consists of 96 scintillating bars with double-sided readout. It covers the remaining polar angles $\vartheta > 25^\circ$ and provides time and position information. Depending on the start-detector geometry the maximal detectable angle varies from $\approx 60^\circ$ to $\approx 80^\circ$ [Böh00].

- **The neutron detector (COSYnus):** The neutron detector is placed behind the vacuum vessel in air and consists of 12 ($200 \times 10 \times 10\,cm^3$) scintillating bars with double-sided readout. It provides an excellent time-of-flight resolution on an active area of 3.4 m^2. The neutron-detecting efficiency is energy dependent, but in general of the order of 10% [Böh98][Kar99].

Forschungszentrum Rossendorf , INFN Torino (Italy), Universität Tübingen, Soltan Inst. for Nuclear Studies (Swierk/Otwock, Poland)

[12] All cover the full azimuth angle (2π).

[13] *Torte* is German for *tart*: The detector consists of 2×12 tart-pieces that form two concentric detector rings.

[14] *Quirl* is German for *mixer*: The detector consists of one straight and two wound scintillator layers (“Archimedian spirals”). The latter two are responsible for the name.

- **The Calorimeter:** The Calorimeter is mounted directly behind the Quirl, but still inside the vacuum tank. It consists of 84 scintillator blocks of about 3 hadronic radiation lengths. In combination with the Quirl, it provides direct particle identification at TOF using the $dE/dx{-}E$ technique. This detector was not used in the January 2000 beamtime [Kre03].
- **The veto detectors:** The three veto detectors (named Hassan, Molnar, and Wolfi) are used to remove events which originate from the beam-halo. All consist of a scintillating plate, where the beam passes undetectedly through a hole. All vetos are mounted “up-stream” with respect to the target [Schr98].
- **Planned and under construction:**
  - A *Straw-Tracker*, consisting of a multilayer of ≈ 3000 straws tubes read out in drift-chamber-mode. Besides optimal tracking of all charged particles, it will be utilized to determine the position of the (delayed) decay vertices of hyperons. Although the active volume will amount to $\approx 1\,m^3$ the mass per unit length will be extremely low (50 mg/cm^2).
  - A *Microstrip-telescope* for improved vertex information in the direct vicinity of the target.
  - A 2*m-target*, which will be placed in the center of the TOF vessel. This will allow an improved solid angle coverage, detecting reaction products up to $\vartheta = 130°$.

A summary of the main TOF components including their material, the number of channels, the date of first commissioning, and the involved group is given in Tab. 1.1. With over 2000 software channels (TDC/QDC), originating from about 10 sub-detectors, the TOF-detector is not a trivial subject at all.

1.3 Structure of this Work

This work covers the *calibration and analysis strategies* of data acquired with the COSY-TOF detector in general, and the *meson production* in particular. Both will be elaborated in detail by using data of a beamtime carried out in January 2000. Here, a proton beam incident on a proton target (liquid hydrogen) was used and the detector setup at this beamtime was as shown in Fig. 1.4. To separate the general calibration and analysis strategies from the actual physics analysis, this work is divided into two parts:

Part I: The Analysis Framework TofRoot

Providing over 2000 readout-channels, the TOF detector is a rather complex device. In addition, the frequent change of the detector setup complicates the calibration and the analysis of the detector data. For each setup, the software has to be adjusted, i.e. the detector geometry has to be incorporated correctly and the routines have to match the actual conditions. To ease calibration and to speed up the data analysis, a set of concepts had been established which led to the efficient implementation of a new analysis framework. This framework is named *TofRoot* and consists of a set of classes and routines which are linked against the currently very popular analysis framework ROOT. Great emphasis is put on “generic programming”, i.e. the software should be able to handle data from whatever beamtime or setup. In this part, the concepts and aims of TofRoot will be given (Ch. 2), then the most important classes will be described (Ch. 3), and finally the calibration procedure will be explained (Ch. 4). The study of this part is strongly recommended for users of TofRoot, but readers only focusing on the physics may skip this part, since the remainder is self-contained and comprehensible on its own.

Part II: Meson Production in Proton-Proton Collisions

The second part covers reactions in proton-proton collisions at beam momenta of $2950\,MeV/c$ and $3200\,MeV/c$. In the beginning, a procedure is developed to extract two-body reactions virtually without background (Ch. 5). Using this, the elastic scattering is analyzed quantitatively which yields an angular distribution with superb resolution[15]. Normalizing this distribution to known high-precision data will then lead to the determination of the (integral) luminosity for this beamtime. The luminosity determination is performed with a very low experimental uncertainty. This is crucial for the subsequent analysis of other reaction channels. Using the same selection criterion as in elastic scattering, the reaction $pp \to d\pi^+$ is investigated (Ch. 6). Total cross sections and angular distributions will be presented which totally agree with previously published data within uncertainty limits. Although the results are limited by the statistical basis, their significance is comparable to that of the world data. Finally, the reaction $pp \to pp\omega$ will be studied in detail (Ch. 7). This channel presently is of great interest to both experimental and theoretical physics, since the reaction dynamics in $pp \to pp\omega$ is of crucial importance for many other fields of theory. A selection criterion is used to enhance this channel over background. Then, missing-mass spectra are determined, from which total cross sections, angular distributions and invariant-mass spectra can be extracted. Finally, the experimental findings are embedded into the existing world data, and the implications of these precise measurements for theory are discussed.

Since three different reactions are covered in this work, which all have different theoretical descriptions, it was chosen to place the theoretical discussion within each chapter. This discussion is rather compressed for elastic scattering and $pp \to d\pi^+$, but detailed and elaborated for the main reaction channel $pp \to pp\omega$.

---

[15] The elastic scattering is then used to extract benchmark results for the angular and time-of-flight resolution of the TOF detector (as obtained after calibration with TofRoot).

Part I

The Analysis Framework TofRoot

Chapter 2

TofRoot

2.1 Introduction

The complexity of software solutions is correlated with the difficulty of the specific problem under consideration. For simple tasks, as adding two numbers, there might be no need for software at all, while to calculate $\sqrt{17}$, a simple program may be adequate. Since this program is so simple, it will most probably have comparable layout, regardless of the programming language used and the experience of the programmer.

The emulation of a "pocket calculator" is a more sophisticated problem. Already here, the list of questions to be answered beforehand is long: programming language, layout, process-related or object-oriented, features, run-time efficiency, extensibility, etc. This simple example illustrates a fundamental rule for software development:

> In the beginning of a project, a ***concept*** is needed to determine how to achieve the final goal. This final goal - the ***aim*** - must also be defined beforehand.

Taking the pocket calculator as an example, additional rules of what the concept should contain will be sketched in the following:

If it is desired that the pocket calculator should be implemented as a GUI[1], then the situation gets more difficult. In this case, the programmer would certainly not edit the graphics "from scratch", but rather use an already existing GUI-library. As complexity grows, other programs, frameworks or tools may be integrated into the development. Hence, the concept must include which *external developments* should (or should not) be integrated.

If the goal is to implement a desktop, of which the pocket calculator is only a miniscule part, then certainly this task is too complicated to be developed by one person alone. Many programmers have to work together. Here, the question arises of how to combine the individual efforts to a common output. Hence, the concept must include how to organize and aid *efficient teamwork*.

As the complexity of software increases, the know-how of the involved programmers also has to be elevated. However, this mandatory know-how, in return, reduces the number of potential co-workers. To enable a "normal user" to utilize the product, *interfaces* between the complex module (the program, framework) and the recipient

---

[1] **G**raphical **U**ser **I**nterface

(the user) have to be implemented. This implies that now two groups are involved with the development: The developers implement and provide the functionality and the users *use* and provide feedback[2]. Hence, the concept must include a strategy for a *user/developer separation*.

Software Development in Modern Physics

Modern high-energy physics is a good example for very complex solutions at the very forefront of software development[3]. Here, typically over 100 individuals are collected into one international collaboration. Software development is organized in groups, where a steering committee divides the work and supervises the results. Each group provides professional solutions to particular problems. This requires a high level of specialization. Priority is set on the development of interfaces (and their documentation), so that the physicists can analyze the data without having to know all the details of *how* the data was manipulated.

In nuclear physics[4] the collaborations are much smaller, and the depth of specialization is less specific. Besides data calibration and analysis each collaborator generally contributes to *many* fields of experimental physics: detector development and setup, beamtime support, data acquisition, electronics, trigger tuning, system operation, and data acquisition. This leads to (very) different skill levels in terms of software programming know-how. Furthermore, instead of one long production run, many "small" beamtimes aiming at different physical reactions are scheduled. The data of each beamtime is then analyzed by "mini teams" (one to three physicists). This often leads to disjunct developments, which results in incompatible code and multiple implementations of routines for solving a similar problem. However, in nuclear physics the complexity of the data analysis is still at a high level. The TOF detector, for example, generates $\approx 100\,GB$ per beamtime originating from about ten sub-detectors with a total of $\approx$ 2000 channels. Therefore, also for modern nuclear physics professional and sophisticated software solutions have to be developed in order to enable *efficient* work, but respecting the special needs and potentials of nuclear physics.

ROOT

From the middle of the 1980s PAW [PAW] was widely used in nuclear and high-energy physics for data analysis. It was originally programmed in `FORTRAN` and designed for the needs and technical possibilities of the time. With the drastic improvement of computing power, and growing amount of raw data in the 1990s, it became clear that PAW had reached its limit (e.g. NA49 [Bru97] with about 10 TB of raw data per run). The planned experiments in the future (LHC, ATLAS, ...) will exceed the amount of produced data of NA49 by a factor of 10^4. New solutions had to be found.

In 1995, René Brun[5] and Fonds Rademakers started the development of ROOT

---

[2] In daily life, we find a lot of examples for this approach: cars and VCRs are very complex objects, where users and developers are separated geographically. Though complex, the user *knows* how to utilize the objects by the provided interfaces (steering wheel, buttons).

[3] E.g. the breakthrough of the Internet, development of the GRID.

[4] From now on, *nuclear physics* will be used synonymously for *medium-energy physics*.

[5] René Brun also was the creator of PAW.

[Bru95], the successor of PAW. ROOT is written in the currently very popular programming language C++. It is designed as a framework (not a program), which means that it is intended to be used as a *tool-kit*. This implies that the user has to have sufficient knowledge of ROOT and C++ to write his/her *own* applications *using* the ROOT facilities.

The ROOT-framework currently consists of over 400 classes, which, among others, aid the user in data I/O, data storage, graphics, fitting, automatic documentation, and histograming. For further information please refer to [Pan03].

C++

Even now (2004!) there still are some polemics about Object-Oriented-programming (OO) in general and the use of C++ in particular. They say C++ would be too complex, difficult, insecure and slow. In fact, all of these accusations are true in the case of misapplication. However, today, C++ is a *quasi-standard* in nuclear and high-energy physics. Most importantly, a lot of tasks can only be solved using the programming techniques provided by C++. OO-programming is a powerful technique to implement very complex software solutions, but it is also easy to “end up in a disaster”. Since ROOT is the standard in nuclear and high-energy physics today - and ROOT is written in C++ - there will be no further discussion about programming languages.

2.2 TofRoot - Concepts and Aims

In early 2000 the TOF-detector was used for the first time with all sub-detectors available[6]. With this upgrade the amount of (readout) channels for the DAQ rose to almost 2000 (see Tab. 1.1). Although this did not overstrain the three existing offline software-packages (Dresden, Jülich, Erlangen) in general, it became clear that a threshold had been reached, where the benefits of further development seemed to be few. It was decided to develop a new software environment to aid all collaborators with offline analysis. The main backbone of the new system should be ROOT, thus **TofRoot** was born.

TofRoot started in the summer of 2000 with M.Schulte-Wissermann and C.Plettner[7]. L.Karsch, S.Dshemuchadse, R. Jäkel, G.Y. Sun, and W. Ullrich joined the team later. The beamtime of January 2000 was partly analyzed with the use of TofRoot, and the beamtime of December 2002 will exclusively use TofRoot.

2.2.1 Mission Statement

As discussed during the introduction to this chapter, any software development should define a final goal (aim) and a strategy (concept) *prior* to the beginning of the implementation. The aim for TofRoot is quite straightforward: A software environment is needed in order to efficiently analyze the data acquired at the experiment. The final system should be transparent, stable, portable, and extendable. In addition the

---

[6] Except the Calorimeter.

[7] Left the collaboration at the end of 2000.

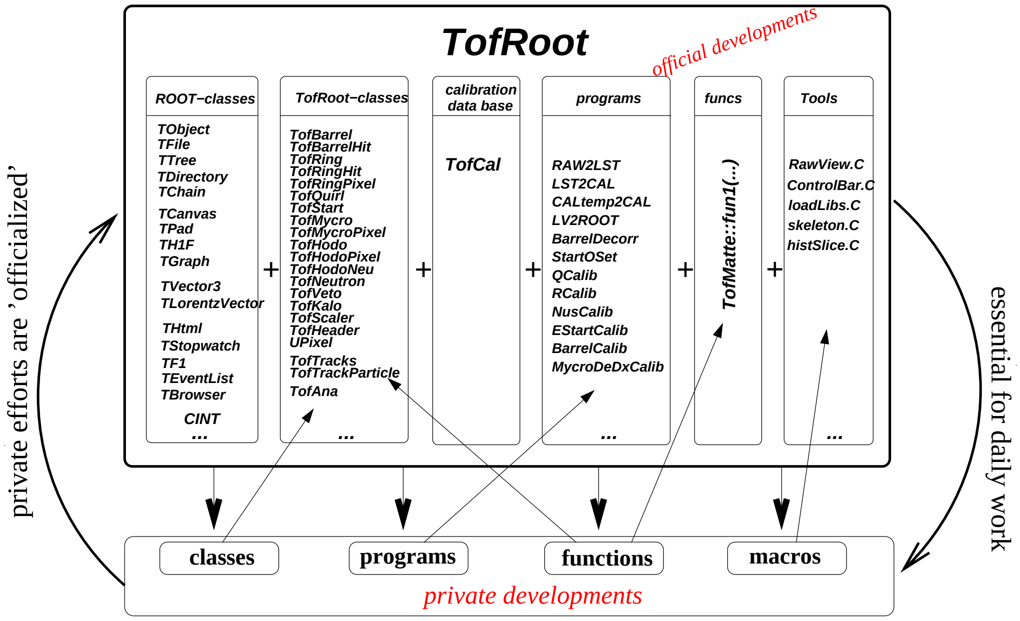

Figure 2.1: *TofRoot: The ROOT framework added with the programs, functions, classes, and macros written especially for COSY-TOF. Using the TofRoot environment assures quick and efficient work. Private developments which have proven to be stable and useful are integrated into the official TofRoot environment.*

software should be able to analyze data of different beamtimes. This is a non trivial aim, since the setup of the TOF detector changes for different beamtimes. In order to achieve this aim, a concept optimized for the special needs of the TOF detector was developed [Schu01]. Most of these concepts are universally valid for all experiments in the field of nuclear physics, and will be discussed in the following.

The analysis of data collected during a beamtime at the TOF-spectrometer is too complex for a single person to be carried out in an acceptable time. Frankly, there are too many channels present, the calibration is too difficult, and finally the physics involved are not trivial at all. This directly implies that *teamwork* is the essential ingredient to obtain positive results. It is important to mention that no programming language, and no analysis framework, will ever enforce teamwork! Teamwork always is related to the willingness and cooperation of the persons belonging to a team. Although a programming language, or an analysis framework, can surely *aid* teamwork by aggravating diverging processes and convincing the individuals of the efficiency of teamwork. TofRoot strongly puts emphasis on these points.

In the past, teamwork was defined as "using the stuff of the guy before me". Since TofRoot had to be developed starting from scratch, real (parallel) teamwork had to be supported (and also used). The software layout had to be designed in a way that everyone *contributes* to an integral effort. Therefore, considering the different programming skills, enthusiasm, and available time of each collaborator, the layout had to be such that distinct parts (of different complexity) could be *separately* assigned to different individuals. These developments are then combined to build the whole system. Each co-worker is *urged* to encapsulate the code into (generic) functions, programs, or classes. Then these new functionalities are *officialized*. This means that the code is supervised, checked for the TofRoot-conventions, and is placed into a special directory (`$TOFROOT_HOME=/usr/local/tof`). After this, the code is used and checked by the whole team. Maintenance still lies in the hands of the original programmer. If an error is found, the error can be removed at one place, and is immediately removed for the whole team. This main concept of TofRoot is shown in Fig. 2.1: What is called TofRoot is the sum of all developments (classes, programs, functions, macros, scripts) residing in `$TOFROOT_HOME` combined with the ROOT-framework itself.

Another main concept of TofRoot is that the official routines must be stable, trustworthy, and easy to call, so that the group members actually *use* them. This seems a trivial aim, but daily life shows the contrary: a psychological barrier often exists to use "alien code". In the TofRoot-environment it is therefore often inevitable to use the official code in order to perform private analysis, i.e the user is *forced* to use the official (and no private) implementations.

Of course a task as complex as analyzing COSY-TOF data also requires sophisticated and professional software-solutions. And given that not everybody has the knowledge and the skill to contribute to these (special) tasks, the direct consequence is that there must be a distinction between *developers* and *users*. Since in nuclear physics everyone is user and developer at the same time, this distinction is made according to the programming skills. Special software-solutions as database programming (`TofCal`), track analysis (`TofTrackParticle`) or loop organization (`TofAna`) are encapsulated (by the developer, the more experienced programmer) into classes and integrated into the official TofRoot-environment. Their functionality, on the other hand, aids the user (the less experienced programmer) to proceed faster with their own, private work. Once the result of this work (the algorithm/function/class) is of general interest, it in return becomes part of the official system. In this way, users can also directly develop as well as developers can use (indicated in Fig. 2.1 by the arrows). This concept is called *(soft) user-developer separation.*

In conclusion, the main advantage of TofRoot is: (1) the ability for efficient *teamwork*, due to the concept of *soft user-developer separation*, and (2) the implementation of sophisticated tools in conjunction with an *enforcement* to use them. The TofRoot concept has proven to be extremely effective and is the main reason for the rapid growth of the TofRoot system.

2.2.2 TofRoot - Necessary Requirements for Success

Considering the final aim - efficient data analysis of COSY-TOF data - a set of requirements had to been defined that would be essential for a positive result. A summary of these requirements, together with a reference where they are described, is given in Tab. 2.1.

ROOT as the Fundamental Framework of TofRoot

ROOT allows to integrate user-defined classes into the overall system. During the development of TofRoot, about 60 classes (container classes, pixel classes, function

Num	page	Description
1	19	ROOT as the fundamental framework
2	25	One fixed data format for all beamtimes
3	20	Separation of data calibration into natural sub-steps
4	22	Calibration of all data (not only subsample)
5	22	Full calibration of whole detector
6	24	One calibration database
7	28	TofRoot coding conventions
8	22	Full data conversion ↔ no data reduction
9	29	Documentation
10	23	Automatization
11	29	Monte-Carlo (LasVegas)

Table 2.1: *Necessary requirements for TofRoot. A description of their implementation is given by following the references.*

class, database class, track class, loop class) were implemented. All are provided to the users in `$TOFROOT_HOME`.

It is important to mention that these classes strongly utilize the functionality of ROOT, as it is very recommended to utilize ROOT-features, where available, instead of private implementations (e.g. `TFile` for data I/O, `TH1F` for histograming, `TF1` for fitting, `TLorentzVector` for relativistic kinematics, ...). On the other hand, no other packages are linked into, or used with the system (GUI, database, 3d-graphics, ...). This keeps the system small and enhances the stability and the portability.

Separation of Data Calibration into Natural Sub-Steps

Formerly, the "usual" way of data analysis was to read raw-data from tape, manipulate it with a program/program-package and then write it to a PAW readable format. The actual analysis was then achieved with the use of PAW. This policy has two main drawbacks:

1. The user has to deal with (at least) two programming languages; C, C++, bash, AWK, perl, Fortran *and* the macro language of PAW.
2. The data is always read from tape which is cumbersome and time consuming. Since the data is always transformed from "raw to end", algorithms with heavy CPU-consumption are prohibited.

With the use of ROOT the first problem is immediately solved, since ROOT itself and the user implementations all are written in one language (C++). The macro language used in the interactive interpreter CINT[8] is also C++. Not only does this free the user of the cost to learn two languages, but macros, rapidly developed in interpreter mode and considered useful, can later be compile to binary executables.

---

[8] The **C INT**erpreter covers about 95% of ANSI C and 85% of C++. It interpretes simple as well as complex macros and also is the interface to ROOT in an interactive session. A major feature is ACLiC, the **A**utomatic **C**ompiler of **Li**braries for **C**INT. It automatically compiles and loads macros used in an interactive session.

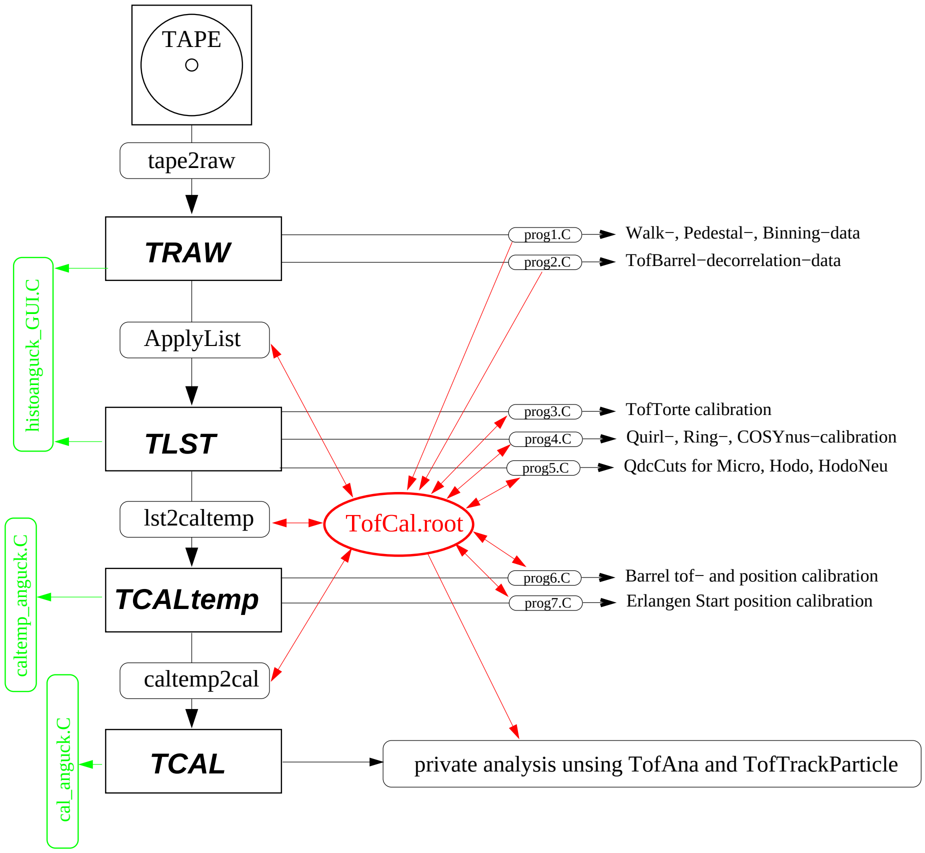

Figure 2.2: *Conversion of detector data from tape using four intermediate data formats* (`RAW, LST, CALtemp, CAL`)*. The CAL-format is fully calibrated and the basis of all data analysis. The calibration database (*`TofCal`*-file, red) communicates with all calibration and conversion routines. The routines automatically read/write calibration data from/to the calibration database. This* official *database is then mandatory for every private analysis using the loop class* `TofAna` *and the track class* `TofTrackParticle`*. To display the control histograms inside the data-files the "viewing-tools" (green) can be utilized.*

The second problem is solved by the TofRoot data-treatment strategy, which separates the calibration and the conversion of data into "natural" sub-steps. This concept is sketched in Fig. 2.2. After being read from tape, the data is converted successively into four different "states" of calibration (formats). The RAW data (only TDC, QDC, channel information) is converted into a LST (LiST) format, where fundamental calibration data is applied. First analysis may start here[9], but usually an additional intermediate data-file (CALtemp) is generated to finally achieve the fully calibrated data-file (CAL). This final file-type is then used for physics analysis. Due to this concept the data is converted step-by-step. CPU-consuming procedures are executed only once (and may run over the weekend), and the output is made persistent, i.e. it is written to file. The subsequent routines start from an already elevated

---

[9] Especially important for online control.

level of calibration/conversion. This is true especially for the final analysis: All calibration/conversion tasks are already fulfilled, thus the data only has to *read* from a file in the calibrated CAL format; all CPU resources remain for the user.

Each of the four formats has a definition (which data is in the file) as well as a definition of the status of calibration (what has already been calibrated). These definitions are valid for all beamtimes. Starting from these intermediate file types, calibration tasks can easily be separated, so that their implementation can be assigned to different co-workers.

No Data Reduction

A very important aim of TofRoot is to provide *all* data to final analysis without substantial reduction. This aim, and providing several intermediate data-samples for each run, of course inflates the amount of needed disk-space drastically. One week of beamtime amounts to about $40\,GB$ of necessary storage media for the RAW format. Taking into account that the needed disc space increases as calibration proceeds, all four formats add to a total of $((40+50+70+80)\,GB =)\ 240\,GB$[10]. This would have been a severe obstacle in the past, but since today 1GB costs less than 1€ this is not a mayor issue anymore. The main advantage of this procedure is obvious: Once converted the data to the final format `TCAL`, the physicist can quickly extend analysis to *all accessible channels*. This approach has strongly aided the analysis of $pp \to d\pi^+$ (see. Ch. 6) and $pp \to pK^0\Sigma^+$ [Kar04].

Calibration of the Full Dataset

According to the previous stated drawback of earlier data analysis, it often was necessary to calibrate the detector with a subsample of the data collected (only few runs). The deduced calibration parameters were then used for the full dataset, assuming that the detector performance was stable.

TofRoot follows a different approach. The calibration routines have to be stable and guarantee an automatic processing of all runs. For each run it should generate the calibration data, a ROOT-log-file and an ASCII-log-file. *All* data in *all* runs are analyzed by the calibration routines, while the correct execution is ensured by the method described on page 23. Examining the calibration data versus the run-number shows a slight, but still important, shift with time (see Fig. 4.1). Therefore, this procedure is inevitable for optimal results.

Calibration of All Sub-Detector

The time scale to implement all calibration routines for all components of the COSY-TOF detector is approximately in the order of ten man-years. This is obviously too long for a single physicist. Because of this, in the past no beamtime was calibrated to the full extent[11]. Compromises always had to be made, e.g. in which calibration-step could be disregarded. This is an severe obstacle in achieving optimal results. TofRoot

---

[10] $240\,GB$ still is cumbersome. In practice, the intermediate file formats are removed, once the conversion has proven to be stable.

[11] Especially when using the complex Erlangen-Start setup.

has the goal to fully cover all components of the COSY-TOF detector.

Due to the utilization of teamwork since 2000, about ten man-years of development have been invested into the implementation of TofRoot. The system now includes calibration routines for all major sub-detectors. A compilation of these efforts is summarized in Tab. 2.2.

Reference	**Task**	**Author**[a]
4.2.1	Walk, Pedestal, Binning	lk,ktb,cp,ul,wu,msw
4.2.1	Curing the de-correlation of the Barrel	msw
4.3.2	Relative alignment of the start-detector	msw
4.3.2	Time calibration of Quirl, Ring	lk
4.3.2	Position and time calibration of COSYnus	lk
4.3.2	Pixel information in Quirl and Ring	lk,cp
4.4.2	Position and time calibration of Barrel	lk, msw
4.4.2	Time correction in the Erlangen-Torte	msw
4.4.1	Cluster and Pixel Information of Erlangen-start	msw
4.3.2	Geometry calibration of Erlangen-start	msw
4.5.1	Track search	msw,lk
4.5.2	Calibration of dE/dx in Microstrip	lk
—	Calibration of dE/dx in Quirl	lk
—	*(u.c.) Calibration of dE/dx in Torte and Barrel*	*(lk,msw,...)*
—	*(u.c.) Calibration of Calorimeter*	*(rj,wu)*
2.2.5	Monte-Carlo simulation (LasVegas/PLUTO)	sd,lk,rj,gys,wu/rj,msw

---

[a] ktb=K.-T.Brinkmann, sd=S.Dshemuchadse, rj=R.Jäkel, lk=L.Karsch[Kar04], ul=U.Lorenz, cp=C.Plettner, msw=M.Schulte-Wissermann, gys=G.Y.Sun, wu=W.Ullrich

Table 2.2: *Listed are all calibration tasks needed to achieve the final (fully calibrated) CAL-format. Except for two routines (u.c. = under construction), all are implemented and used for two beamtimes (2000, 2002). A reference to the description is found in the first, the involved authors are listed in the third column.*

Automatization

Dividing the calibration and the data conversion into different subtasks (programs) urgently requires a method to guarantee the correct execution of *all* routines. It must be ensured that neither a single step is missing, nor that an undetected error occurred. Only a system that is *easy to use* and *"fool-proof"* will be accepted by the collaboration.

The behavior of the TofRoot calibration and conversion programs is determined by start-parameters, provided at execution time (`argc, argv`). Some programs may await a total number of more than ten parameters (beamtime, beam momentum, log-file name, ...). Instead of launching each program manually, which is extremely error-prone, the programs are launched from shell-scripts. An example is given in Fig. 2.3 at the right. Within the shell-script the starting parameters can be edited easily . As a fundamental rule, the run-scripts always take the run-number as a parameter itself, so that each program is executed by a call like (`Run<somename> <runnum>`).

In a next step, run-scripts which read the same format are successively called by

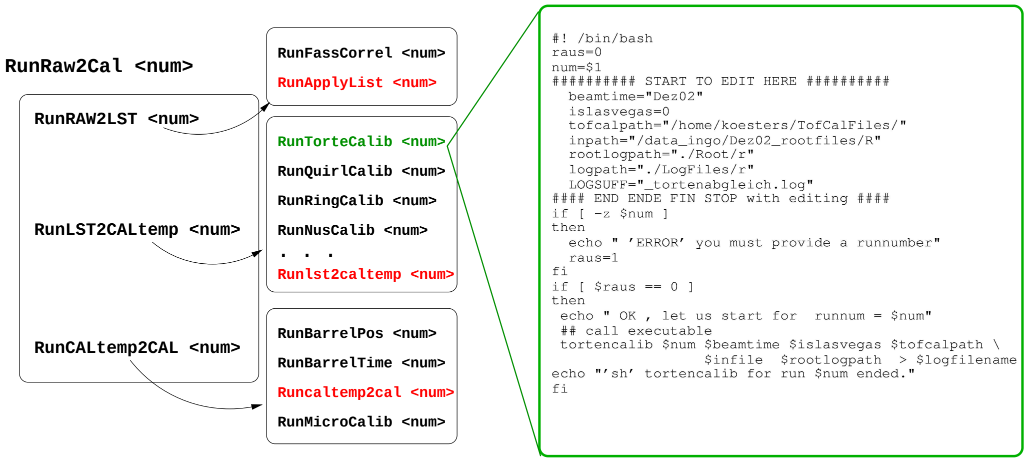

```
#! /bin/bash
raus=0
num=$1
########## START TO EDIT HERE ##########
  beamtime="Dez02"
  islasvegas=0
  tofcalpath="/home/koesters/TofCalFiles/"
  inpath="/data_ingo/Dez02_rootfiles/R"
  rootlogpath="./Root/r"
  logpath="./LogFiles/r"
  LOGSUFF="_tortenabgleich.log"
#### END ENDE FIN STOP with editing ####
if [ -z $num ]
then
  echo " 'ERROR' you must provide a runnumber"
  raus=1
fi
if [ $raus == 0 ]
then
 echo " OK , let us start for  runnum = $num"
 ## call executable
 tortencalib $num $beamtime $islasvegas $tofcalpath \
                  $infile  $rootlogpath  > $logfilename
echo "'sh' tortencalib for run $num ended."
fi
```

Figure 2.3: *Automatic program execution: Each of the TofRoot programs are executed by a shell-script (*`Run<somename>`*) where starting parameters (run number, beamtime, beam momentum, log-file name, ...) can be easily be edited. To ensure the correct execution of all programs in the right order, these scripts themselves are executed by other shell-scripts. As a result, the conversion of a specific run from* `RAW` *data into the final calibrated format (*`CAL`*) can be fulfilled using only one command:* `RunRaw2Cal <runnumber>`.

master-scripts. Finally these master-scripts are called by the super-script, so that the conversion of a specific run from `RAW` data into the final calibrated format (`CAL`) can be fulfilled using one command only: `RunRaw2Cal <runnum>`. This procedure ensures the correct execution of all programs in the right order.

If an error occurs (e.g. missing calibration data), it is documented in the mandatory log-file, and can be observed examining the (mandatory) control histograms. In most practical cases an error in one routine will prevent the writing of calibration data into the `TofCal`-database. This missing information will trigger a chain of errors in all subsequent programs. Hence, the data is only transformed up to the final `CAL`-format when no error occurs in any of the calibration/conversion programs[12].

One Calibration Database

One very big obstacle for teamwork, even within the analysis of one beamtime, is the laziness of coworkers. A very popular method of "sharing" calibration data is to copy it to one's own, private site and then adopt it for private usage. These adoptions are then never synchronized with the team members, so that after a certain time the developments are so disjunct that is is virtually impossible to recombine efforts. Another popular bad habit is to use calibration data which is not directly associated to the observed runs. This may yield quick (preliminary) results, but as analysis proceeds, often this fact simply is forgotten. To avoid this, TofRoot strictly *forces to use the official database* and it also requires that *every run is calibrated.* The database is implemented as a class (`TofCal`).

---

[12] Still, it is *very advisable* to carefully check the log-files, control histograms and the "statistics output" of the loop class `TofAna`.

The central role of the TofCal-database can be seen in Fig. 2.2. All calibration/conversion programs communicate with the database, i.e. needed calibration data is read, retrieved (new) calibration data is written. For final analysis, the user *must* utilize the loop class `TofAna`, as well as the tracking class `TofTrackParticle`. Both require a connection to a `TofCal`-database, and for all practical applications they require a database including all calibration data to a specific run. The only database which fulfills these requirements is the official database.

This approach secures coherent development which is inevitable for rapid teamwork.

2.2.3 The Fixed TofRoot File Format

The COSY-TOF detector is a *modular* detector consisting of three to twelve subdetectors. It also is a very *versatile* detector system, since for each beamtime the detector setup is optimized for the detection of a desired reaction. Thus, also the software representation of the TOF-detector should reflect this modularity and versatility. As a consequence, data files originating from different beamtimes will have different contents. However, for efficient work, previous developments have to be reused without significant changes. This can be achieved, if the involved programs always take a *fixed* an *well defined* file format as input.

Therefore, the file-format must satisfy two conditions: The file-format must be modular and flexible, but at the same time, fixed and well defined. Using ROOT and TofRoot features, a strategy was developed in order to cut this Gordian knot; this will be presented in the following.

ROOT File

A ROOT file is a file written to hard disk in a ROOT data format. For this the class `TFile` is used, which completely covers the data-I/O[13]. A `TFile` can be updated, inspected with a browser, and it can be accessed over the net. Unlike `PAW`, where pure data (numbers) are written into ntuples, `ROOT` follows a different (OO-motivated) strategy. A `TFile` writes *objects*, i.e. instances of classes. All classes derived from `TObject`[14] can easily be written to a ROOT file. Deriving from `TObject` ensures the automatic creation of a *streamer method* which is used to write the class information. Especially a `TTree` object, which is the main ROOT data structure, can be written to file. A `TTree` has a number of branches associated to it, where each branch is connected to a data container (class). The connected classes can be of ROOT itself or user-defined. When the tree is filled (a event), the information of each of the data containers is written into the associated branch. During reading, each data container is filled with the information found for this event. The actual data is then accessed via member functions (Getters/Setters) of the container classes.

This approach is extraordinary flexible and efficient in the analysis of large amounts of data. Not only is there no limitation on the number of participating branches,

---

[13] IO = input-output

[14] This includes all TofRoot and (almost) all ROOT objects; e.g. histograms, functions, vectors, matrices, ...

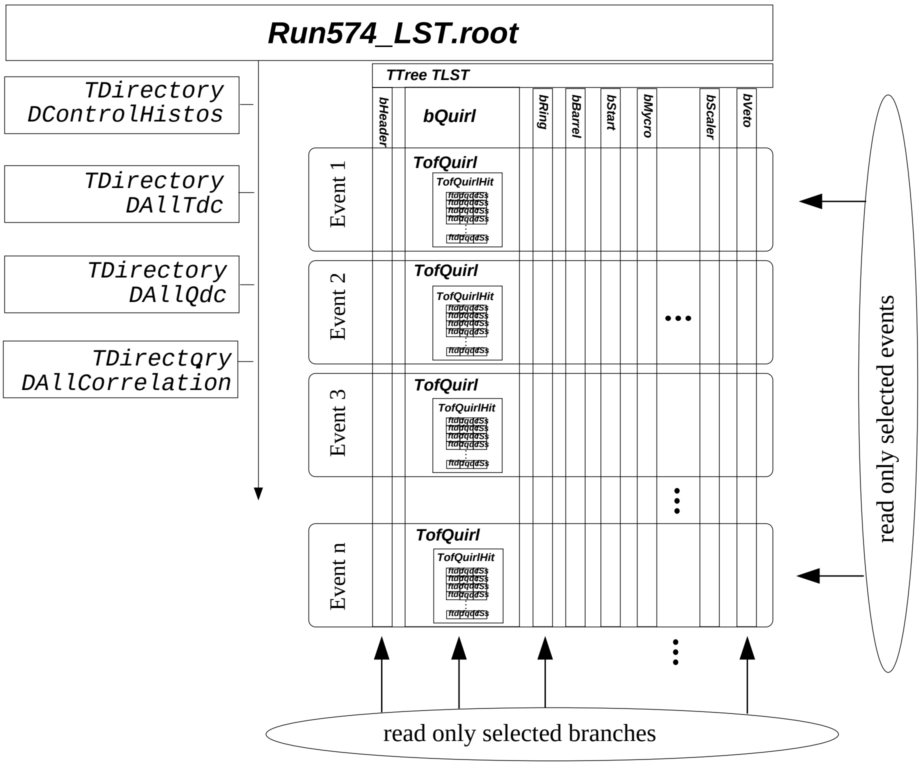

Figure 2.4: *Schematic view of a TofRoot-file. The data is organized in a* `TTree` *where each sub-detector is represented by one branch (the branch* `bQuirl` *is shown in more detail). Each branch is connected to an instance of a data container. The containers embody the actual data, which is written to the branch for each event. Branches can be read separately, and data can be accessed in any order. In parallel to the actual data control-histograms, organized in a directory structure, are written to the file. They are filled during the conversion loop and allow an easy and quick control of the file contents.*

but the involved container classes can themselves have (eventually complex) member functions, which can be used for data processing (calibration, calculation). However, there is the disadvantage that the data containers (in most practical cases) first have to be implemented. The benefits of this approach always has to be balanced against the costs. In the case of TofRoot, however, the benefits are huge and the costs are few.

TofRoot File

For TofRoot a file format was developed using the benefits of `TFile` and `TTree` as described above. The layout of the TofRoot file is shown in Fig. 2.4. Each sub-detector (Quirl, Ring, ...) is represented by a container class (`TofQuirl, TofRing, ...`). Each (instance of a) container class is associated with a `TBranch (bQuirl, bRing, ...)`. Since there is no limitation to the number of branches, only the branches of the detectors actually in use are written into the tree. If in future beamtime a new detector is installed, or some detector component is missing, it only changes the number of branches inside the tree. The overall geometry remains the same. During the connection to a `TFile` the loop class `TofAna` and all calibration/conversion programs check if a branch exists. If a branch is missing, appropriate action is automatically performed.

Control Histograms

A major advantage of `TFile` is the possibility to store histograms in a directory structure[15] along with the actual data. This feature is largely used in the TofRoot files: All programs fill control histograms (the "standard histograms") during conversion/calibration of the data. These histograms (up to 3000) are extremely helpful for checking the data files without the need to re-loop through the entire dataset. For each data format, and (almost) every calibration routine, exists a "viewing macro" which displays the standard histograms interactively.

Reducing the Necessary CPU-Time - Benchmarks

With the use of a `TTree` the user has two main possibilities to speed up data analysis. The first is that the user can read only *desired events*. This could be the case if in an earlier analysis the "interesting candidates" had already been selected. The second possibility is to read only *desired branches*[16]. It is also possible to combine both methods: The user reads only some of the events and at the beginning only a few necessary branches. Then he/she analyzes the event, decides if it is worth further investigation, reads the remaining branches and continues on to the final analysis.

This possibility is extremely helpful, since it frees the physicist from the quandary of either having to wait too long for analysis, or working with an (eventually insufficient) subset of data. Table 2.3 shows benchmark results[17] achieved with the loop class and the code presented on page 37. The event rate does not scale linear with the step size, since "fast forwarding" to next event found in the event list also requires time.

	every event	every 10^{th} event	every 100^{th} event
read whole event	410 $evts/CPUs$	2400 $evts/CPUs$	5900 $evts/CPUs$
read only the track branch	5200 $evts/CPUs$	14000 $evts/CPUs$	23500 $evts/CPUs$

Table 2.3: *Reducing the necessary CPU-time during data analysis - benchmarks.*

---

[15] Similar to an UNIX file system a ROOT file can contain directories filled with an unlimited number of objects and in an unlimited number of levels (sub-directories).

[16] Both features are supported by the loop class `TofAna` (`TEventList` generator, `TBranch` selection; see p. 39).

[17] Processor: 750 MHz Pentium, HD: IDE, 5600 min^{-1}.

2.2.4 TofRoot Coding Convention and Rules

Coding Convention

As every programmer has a private style of programming, it is very important to set up coding conventions for teamwork. Without conventions, debugging will become “worse than chaos”. Besides the coding conventions set up by ROOT,[18] TofRoot itself defines a list of strict conventions. Every code prior to being officialized is checked to see whether it obeys these conventions. The TofRoot conventions are summarized in the following table.

Description	**Example**
All **g**lobal variables (except histograms) start with “g”	**g**ZQUIRL
All detector container pointers start with “ev” (**ev**ent)	**ev**Quirl
All **h**istogram pointers start with a “h”	**h**MyHisto
Provide debug information in every routine	`#ifdef DEBUG ...  #endif`
Provide control histograms in every program	`hQdcQuirl0`
Provide a ASCII log-file for every program	`tortecalib_<runnum>.log`
Provide a HTML documentation for every implementation	`MyClass.C.html`
Use `TMath.h` functions (instead of `math.h`)	`TMath::Sin(TMath::Pi())`
Use `Double_t, Int_t, ...` (instead of `double, int, ...`)	`Int_t i = 0;`
For log-file output use `cout`, for standard output use `cerr`	`cerr/cout`
Use suffix “Deg/Rad” for all angular Getters/Setters	`GetThetaDeg()`
Comments always start with **’I’**nfo, **’W’**arning or **’E’**rror	`cout<<"'W' strange ...  "`
Always call `new` at top level, **never** inside a loop!	`a=newA();for(..){a→a();}`
“Call-by-reference”: indicate the passing of an *address*	`Int_t ara[3]; foo(&ara[0]);`

Units and Reference Frame

For any combined effort, it is necessary to define units and the coordinate system. Otherwise chaos is inevitable. For TofRoot the following is defined:

TOF unit *length*	*mm*
TOF unit *time*	100 *ps* = 1 TDC channel
TOF unit *energy*	MeV (analogously: [momentum]=MeV/c, [mass]=MeV/c^2)
Coordinate system	right-handed: z-axis=beam-axis, x-axis=**“left”**, y-axis=**“up”**
Azimuthal angle	$(0 \leq \varphi < 360°)$, $\varphi = 0$ at $(x, y) = (1, 0)$
Origin $(0, 0, 0)$	in the center of the target

Coding Recommendation

C++ enables the programmer to use very sophisticated programming techniques. The concepts of “information hiding” and “polymorphism” as well as (abstract) base classes, etc. are very useful in many fields of software development. However, when different physicists (with different programming skills) have to work on the same project, either the code must be fail-safe, professional and optimized (speed, memory, log-info), or it *must* be written in an “easy manner”. The complexity of the code should always be scaled to the least experienced co-worker who is involved into the maintenance of

---

[18] http://root.cern.ch/root/Conventions.html

a specific implementation. Every experienced programmer has to keep in mind that even (simple) constructions like `i = i < 0?i : -1;` or `for(i=10;i>0;i--){...}` can convince an unexperienced programmer that something is not correct. Of course there always has to be a compromise between simplicity and complexity regarding the actual problem, but if there is a choice, always use the more simple solution.

Although TofRoot frequently uses OO-features, this concept has also led to the "procedural" layout of the calibration chain. It is much easier to develop a set of single, disjunct programs, as it is to encapsulate everything into a class framework. In this sense TofRoot is a hybrid between a true OO-approach and a conventional program/function collection[19].

Documentation

A very important issue in software development is the documentation of source code. The main features of a program/class/function (and its usage) have to be described as well as single numerical operations within the code. Documentation has to be learned and is not an easy sub-task at all. Too much or not enough documentation may lead to incomprehensible code.

To aid documentation ROOT provides a very powerful tool: the class `THtml`. `THtml` can convert any text document automatically into HTML format. The resulting file can then be read with any standard browser. Using programs or classes as input, `THtml` will, according to some simple rules, generate highlighted function/class descriptions. In addition, it will automatically generate reference links to the ROOT and TofRoot classes. All `TofRoot` classes and programs are documented in this way, and are accessible via the web. Each new development should therefore not only be documented within the source code itself, but also transformed into a HTML-file on the Internet.

Another very useful documentation tool is `SARUMAN`[20] which was invented and implemented by M. Greschner. It automatically documents the "HOWTOs", contributed by the team. Its core is a perl script. Once executed it recursively descends to all subdirectories, thereby reading all files with the suffix ".txt". These files are converted using `THtml` (batch call to ROOT) and an HTML-index is generated for every directory. The converted files are placed in a special directory foreseen for the HTML documentation. This part is only accessible locally, since its content is for internal usage only.

2.2.5 Monte-Carlo

Any system working in the realm of nuclear physics must contain a Monte-Carlo (MC) solution. It can be distinguished between two different "questions" a MC-system should answer: The first, and more simple, question is the numerical reproduction of physical reactions. This leads to (kinematic) information of what to expect in an envisaged experiment (angles, momenta, correlations). This problem is, in general, solved by an event generator in combination with a suitable visualization tool.

---

[19] This is not a bug, but a feature!

[20] **S**ofisticated **A**utomated **R**eally **U**sable **MAN**ual generator

The more complex expectation to a MC-system is that it *completely* reproduces and tests the whole analyzing system, starting from event generation, particle propagation through the detector including secondary reactions, signal treatment, conversion to “data”, calibration of the detector, data-treatment, and final analysis. This is extremely important, because only through this the detector performance *and* the software (reconstruction) efficiency can be deduced.

Both approaches are implemented in TofRoot and are described in the following.

Quick Monte-Carlo: PLUTO

The PLUTO package [PLUTO] is a modern OO-approach to Monte-Carlo analysis. It provides a very powerful event generator including the most recent particle physics input-data[21] as branching ratios and differential observables. It is very easy to use, quick and covers an enormous amount of physical reactions.

An interface from the PLUTO output to TofRoot has been developed where the information is directly converted into `TofTrackParticle`s. The tracks can be smeared (time-of-flight, ϑ, φ) to simulate “real” detector data. Using this, a broad variety of reactions can *quickly* be analyzed. Convenience and speed are the main advantages of this approach. However, since the information from the event generator “bypasses” all calibration/analysis routines and also does not take into account secondary reactions within the detector, it cannot be considered a full MC solution.

Full Monte-Carlo: LasVegas

In 1995, an OO-based Monte-Carlo framework was developed especially for the COSY-TOF detector: LasVegas [LasV]. A major advantage of LasVegas is the implementation of the Archimedian spirals of the Quirl/Ring detectors. Since TofRoot wanted to benefit from this existing package, LasVegas was ported to `Linux` and an interface between LasVegas and TofRoot was developed. Because LasVegas was not developed for the Erlangen-Start and the Calorimeter, these detector components had to be added. The LasVegas developments were accomplished by S. Dshemuchadse, R. Jäkel [Jäk03], and L. Karsch.

LasVegas consists of three main parts: the event generator, the particle propagator, and the signal output.

- An event generator is incorporated into the LasVegas package. It generates phase-space distributed events for a broad variety of reactions. Using an ASCII-interface, it is also possible to use external event generators.
- The particle propagation simulates all possible reactions within the detector *completely*, i.e. the primary particles are propagated through all active and passive volumes, experiencing energy loss and small-angle scattering. Secondary reactions (δ-electrons, nuclear reactions, elastic scattering) are also simulated. *All* reaction products[22] are propagated until they either leave the detector or are stopped to rest.

---

[21] The development of PLUTO has stopped (2003), but will be further maintained by the `PANDA` collaboration.

[22] And recursively also their secondary reaction products.

- The energy deposits in all active volumes are calculated and converted into light output. Finally the light is propagated in the scintillator and transformed into TDC/QDC conversions.

The output of a LasVegas simulation is a TofRoot file in the RAW format, i.e. only pure TDC/QDC-conversions of the triggered channels. The LasVegas data is then calibrated, converted, and analyzed using the very same software as real data. This procedure gives a good understanding of the detector *and* software efficiency.

Especially helpful is the storage of the original event generator information (origin, direction, velocity, type) of all primary particles. In addition, also all decay products and secondary particles are accessible. This information is stored in parallel to the "real" data in the LasVegas class `TofLVEvent` associated with the branch `bLVEvent`. This procedure enables a direct (quantitative) comparison of the reconstructed tracks with the original particle information. This is not only very helpful during code development, but even crucial for optimum results of the final analysis: The acceptance of the detector/software system is determined by the ratio of the number of offered to positively detected events, i.e. by a quantitative comparison of the original event generator information with the found tracks. Only after this, the data can be precisely acceptance corrected (see p. 70, 85, and 105).

Chapter 3

TofRoot - Special Classes

One aim of TofRoot is to keep the system as transparent and simple as possible. However, data analysis in nuclear physics is too complex to do without at least some more sophisticated tools. In TofRoot, these tools are implemented as classes and the associated libraries are automatically loaded for each interactive ROOT session. The makefile which compiles the loop class `TofAna` also includes all necessary "links" to the libraries. Table 3.1 shows the most important classes of TofRoot. All will be described in the following.

Name	**Description**	**Author**[a]
Container Classes	Data storage and (simple) management	msw,cp
TofTrackParticle	Track information and kinematic calculations	msw
TofAna	Loop class - loops over single or multiple files	msw,ul
TMatte	Function collection - helpful tools collected in one place	msw,lk,gys,rj
TofCal	Database containing geometry and calibration data	cp,msw,ul

---

[a] rj=R. Jäkel, lk=L. Karsch, ul=U. Lorenz, cp=C. Plettner, msw=M. Schulte-Wissermann, gys=G.Y. Sun

Table 3.1: *The most important TofRoot classes. The involved authors are listed in the third column.*

3.1 TofRoot Data Containers

Since TOF is a modular detector, designing the software layout modularly seems obvious. This modularity was already described in the previous chapter (see p. 25). The detector data is stored in a `TTree` structure, where each branch of the tree represents a sub-detector of the TOF-spectrometer. Associated with each branch in an *object*, i.e. an instance of a class. These special TofRoot classes store the detector data of each event and therefore are called *data container* classes. A sketch of a container class is shown in Fig. 3.1, where its placement within a data tree is indicated as well (compare to Fig. 2.4).

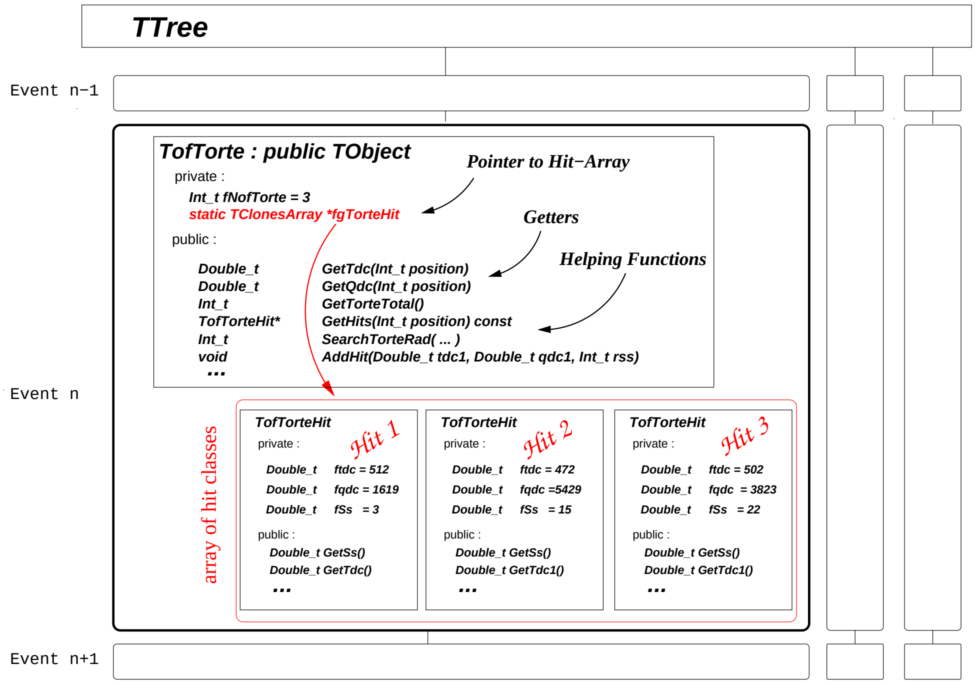

Figure 3.1: *Each container class of TofRoot represents a sub-detector of COSY-TOF. The information of each triggered channel is stored a hit-class which is written to a (TClones-)array. Besides Getters the container classes also (may) provide more sophisticated functions.*

Each sub-detector is represented by a main data-class (`TofQuirl`, `TofRing`, ...). These classes, in general, have as private members the *total number of hits* and the *hit array*. The type of the hit array is a special ROOT class (`TClonesArray`): It stores (identical) ROOT (or TofRoot) objects and is optimized for fast data I/O[1]. For simplicity, the user can think of a `TClonesArray` as an "ordinary" array with a length of the total number of triggered channels. The entries of this array are "hits", i.e. instances of the "hit-classes" (`TofQuirlHit`, `TofRingHit`, ...). Each hit-class contains a triplet of DAQ information associated with a triggered channel (usually a photomultiplier); the TDC, the QDC, and the channel number. The channel numbers are counted for each sub-detector (Quirl=[0,95], Ring=[0,191], ...) and are called *(relative) signal source*: *(r)ss.*

A big advantage of using objects (classes) to store data is the possibility to implement member functions which also *manage* the data. A simple example is how to access the TDC/QDC/rss data by calling the "Getter" of a container class[2]:

---

[1] The use of `TClonesArray` reduces the number of `new/delete` calls by using the standard but not well know C++ operator "new with placement". This speeds up data-IO tremendously.

[2] The function is abbreviated to the core functionality. To view the full implementation please refer to the online documentation.

```
Double_t TofTorte::GetTdc(Int_t pos){
        return((TofTorteHit*)fgTorteHit->At(pos))->GetTdc();
}
```

The desired information is stored in an instance of a hit class which itself is stored in the hit array (`fgTorteHit`). To access the data, first a pointer to the hit-class at a certain position has to be retrieved, then this pointer has to be casted to the type of object found in the array. Only then the “Getter” of the hit class can be called. Doing this for every value would make daily life cumbersome and the code difficult to read; but using `TofTorte::GetTdc(i)` a “normal” user will access the i^{th} TDC in an natural and intuitive way, probably never even noticing the actual implementation. In addition to the simple “Get/Set” functions the main data container classes may also provide more sophisticated algorithms, i.e. functions for data manipulation and calibration.

The Quirl and Ring container classes have a slightly modified layout. Here, pixel information ($\vartheta, \varphi, r, \Delta\vartheta, ...$) is stored in an additional `TClonesArray` which is filled “in parallel” to the hit-array. A special treatment is chosen for the Erlangen-Start detectors. While in RAW and LST format “hits” are collected in data container as described above, in the CALtemp and CAL format arrays of “clusters” (consecutive hits) are collected. The data containers are called “pixel-classes” (e.g. `TofHodoPixel`), because they provide a variety of powerful member functions to calculate pixel properties for any possible cluster combination. This will be discussed in more detail in 4.4.1. However, the overall structure of all data container classes always remains the same: A (main) container class stores an array of classes containing the actual information. In fact, also the architecture of the track-classes is organized in the same manner. This will be described in the next section.

3.2 TofTrackParticle - The Track Class

One of the backbones of the TofRoot analysis is the track class `TofTrackParticle`. While the “ordinary” data container classes store “hit” information (TDC, QDC, cluster, pixel), the track classes are designed to allow quick and easy access to the relevant physical information ($\beta, p, \vartheta, \varphi, ...$). Using the track-class enables the user to concentrate on the “real physics”.

Inherent Track Information

The `TofTrackParticles` are filled during the conversion from the CALtemp to the CAL formate (4.5.1). The pixel informations in the Erlangen-Start detector together with a linear fit algorithm are used to discriminate “physical tracks” from background. If a track passes a χ^2-test, its information is stored in the private members of the track class and written to file. This information includes the direction and the origin (and their uncertainties), the time-of-flight, the χ^2 value, the triggered QDC conversions and where to find the participating clusters/pixels in the data tree. A listing of all private members of `TofTrackParticle` is given in Tab. 3.2. On first sight, storing all QDC-conversions (`fqdcArray`) and positions as well as signal sources (`fposNmeanss`)

Type	Name	Description
Bool_t	fIsRealTrack;	Does this track have pixels in the Erlangen-Start?
Double_t	ftheta;	Polar angle ϑ $[rad]$
Double_t	fphi;	Azimuthal angle φ $[rad]$
Double_t	ftof;	Time-Of-Flight $[100ps]$ (TOF time unit)
Double_t	fchi;	$\sqrt{\chi^2}$ of the track fit
Double_t	fbeta;	Relativistic velocity β
Double_t	fgamma;	Lorentz factor γ
Double_t	faufpunkt[3];	Emission point $(x, y, z)[mm]$
Double_t	frichtung[3];	Direction $(dx, dy, dz)[mm]$
Double_t	ferraufpunkt[2];	Uncertainty of emission point
Double_t	ferrrichtung[2];	Uncertainty of direction
Double_t	fqdcArray[12];	All participating QDC values
Double_t	fposNmeanss[12];	All participating positions and signal sources
Int_t	fzwilling;	Position of a twin (if any)
Double_t	fmass;	Mass $[MeV/c^2]$ (set by user)
Double_t	fenergy;	Energy $[MeV[$ (calculated)
Double_t	fmomentum;	Momentum $[MeV/c]$ (calculated)

Table 3.2: *The private member of* `TofTrackParticle`*. The quantities are evaluated during the track fitting procedure in the conversion of CALtemp to CAL data. All but the last three can directly be accessed using simple "Getter" functions. The last quantities are set according to a user-defined mass hypothesis (*`TofTrackParticle::Eval(Double_t mass)`*).*

seems to only inflate the file with redundant information, since this information is still present in the according branches. However, the cost of increased file size is less then the profit: *autarchy* of the `TofTrackParticle`s. Often it is possible to analyze the data using exclusively the track information, i.e. reading the track branch only. In this case (see Tab. 2.3), the speed of data analysis is enhanced by a factor of eight. If needed, "missing" branches can be loaded by the loop-class for all events, or they can be read "manually" for each single event of interest.

Dynamic Calculation of the Geometry and Kinematics

Besides simple "Getters" `TofTrackParticle` has a large amount of member functions which *dynamically* calculate observables. This has three main reasons:

1. Storing all information known during the track search is prohibited by file size.
2. Many observables simply are unknown when the track is filled: The TOF-spectrometer provides no means for direct particle identification. Only the velocity vectors are measurable and the identification of the particles rather is accomplished during the analysis of the *whole event*, i.e. kinematical constraints together with a mass hypothesis must be used to identify the reaction pattern.
3. Being a modular detector implies that the geometry of the TOF-spectrometer *changes* from beamtime to beamtime. Therefore the geometry can not be placed

Description	Return Value	Function Name	Eval
Default constructor	TofTrackParticle	TofTrackParticle()	-
"Normal" constructor	TofTrackParticle	TofTrackParticle(...)	-
Copy constructor	TofTrackParticle	TofTrackParticle(TofTrackParticle&)	-
Destructor	virtual void	~TofTrackParticle()	-
Diff. of "back-to-back"ness	Double_t	Acolliniaritaet(TofTrackParticle* evTPother, ...)	(✓)
Angular difference to other TP	Double_t	CalcAngleDeg(TofTrackParticle* evTPother)	✓
Calculate the particle in the CMS	Int_t	CalcCMSParticle(TofTrackParticle* evTPother)	✓
$\Delta\varphi$ to other TP	Double_t	CalcDPhiDeg(TofTrackParticle* evTPother)	-
$\Delta\vartheta$ to other TP	Double_t	CalcDThetaDeg(TofTrackParticle* evTPother)	-
Expected TOF from $\vartheta, \varphi, \beta_{TP}$	Double_t	CalcExpectedTof(Double_t betatest)	-
Momentum $\parallel$ to beam axis	Double_t	CalcPPara()	✓
Momentum $\perp$ to beam axis	Double_t	CalcPPerp()	✓
Momentum along the x-axis	Double_t	CalcPX()	✓
The primary vertex of 3 TPs	TVector3	CalcPrimVertex(...)	-
Momentum along the x-axis	Double_t	CalcPY()	✓
TLorentzVector in the lab-frame	Int_t	CalcTLorentz(TLorentzVector* carryLV)	✓
TLorentzVector in the CMS-frame	Int_t	CalcTLorentzCMS(TLorentzVector* carryLV)	✓
Position at the Barrel (internal use)	Double_t	CalcZeta()	-
Clear the class information	virtual void	Clear(Option_t* option)	-
Closest distance of two TPs	Double_t	ClosestDistance(TofTrackParticle* otherTP)	-
Distance to origin	Double_t	DistanceTo000()	-
Calculate E_{TP}, p_{TP} to "mass"	Int_t	Eval(Double_t mass)	-
Flight distance from target to stop	Double_t	Flugdistanz()	-
Emission point	TVector3	GetAufpunkt()	-
Emission point	void	GetAufpunkt(TVector3* carry)	-
Get β_{TP}	Double_t	GetBeta()	-
Get $\sqrt{\chi^2}$ (from the fit)	Double_t	GetChi()	-
Get E_{TP}	Double_t	GetEnergy()	✓
Get error of emission point	void	GetErrAufpunkt(Double_t* errAPcarry)	-
Get error of direction	void	GetErrRichtung(Double_t* errRIcarry)	-
Get γ_{TP}	Double_t	GetGamma()	-
Get mass (previously set by user)	Double_t	GetMass()	-
Get sub-detector hits	Double_t	GetMeanSs(Option_t* which, Int_t subwhich)	-
Get p_{TP}	Double_t	GetMomentum()	✓
Get φ_{TP} (Deg)	Double_t	GetPhiDeg()	-
Get φ_{TP} (rad)	Double_t	GetPhiRad()	-
Get position in `TClonesArray` (Ring)	Int_t	GetPixelPos(TofRing* evRing, ...)	-
Get position in `TClonesArray` (Quirl)	Int_t	GetPixelPos(TofQuirl* evQuirl, ...)	-
Get position in `TClonesArray`	Int_t	GetPos(Option_t* which, Int_t subwhich)	-
Get array with sub-detector info	void	GetPosNMeanSsArray(Double_t* carry)	-
Get Qdc value of sub-detector	Double_t	GetQdc(Option_t* which, Int_t subwhich)	-
Get Qdc values of sub-detectors	void	GetQdcArray(Double_t* carry)	-
Get direction of TP	TVector3	GetRichtung()	-
Get direction of TP	void	GetRichtung(TVector3* carry)	-
Get ϑ_{TP} (Deg)	Double_t	GetThetaDeg()	-
Get ϑ_{TP} (rad)	Double_t	GetThetaRad()	-
Get time-of-flight	Double_t	GetTof()	-
How many "twin-TPs" found	Int_t	GetZwilling(Int_t what)	-
Barrel detector involved?	UInt_t	HasBarrel()	-
(Small) Hodoscope detector involved?	UInt_t	HasHodo()	-
(Big) Hodoscope detector involved?	UInt_t	HasHodoNeu()	-
Microstrip detector involved?	UInt_t	HasMycro()	-
Pixel in Quirl/Ring with 3 layers?	UInt_t	HasPixel3()	-
Pixel in Quirl/Ring with 4 layers?	UInt_t	HasPixel4()	-
Quirl detector involved?	UInt_t	HasQuirl()	-
detector involved?	UInt_t	HasRaute()	-
Ring detector involved?	UInt_t	HasRing()	-
Torte detector involved?	UInt_t	HasTorte()	-
Does a "twin-TP" exist?	Int_t	HasZwilling()	-
Initialize all TP in this scope	Int_t	Init(TofCal* cal, Double_t pbeam, ...)	-
2 hits in the Erlangen-Start	Bool_t	Is2outof3()	-
3 hits in the Erlangen-Start	Bool_t	Is3outof3()	-
β_{TP} <betamax?	Bool_t	IsEvaluable(Double_t betamax = -1.)	-
Is TP outside the target?	Double_t	IsOutsideTarget(Double_t beamrad=1., ...)	-
TP has hits in the Erlangen-Start?	Bool_t	IsRealTrack()	-
Print this TP	virtual void	Print(Option_t*)	-
Fit this TP again using different errors	Int_t	ReFit(...)	-
Fit two track to common origin	Int_t	ReFitTwoTracks(TofTrackParticle *evTPother, ...)	-
Set values (internal usage)	Int_t	Set(...)	-
Set emission point and direction	Int_t	SetAufpunktRichtung(TVector3* v3ap, v3ri)	-
Set β_{TP} and calculate γ_{TP}	Int_t	SetBetaCalcGamma(Double_t beta)	-
Initialize the TP by a `TLorentzVector`	Int_t	SetMCTrack(TLorentzVector* lvtr, ...)	-
Set the direction	Int_t	SetRichtung(TVector3* v3richtung)	-
Set TOF, βTP and γ_{TP}	Int_t	SetTofCalcBetaGamma(Double_t tof)	-
Set a "twin-TP" (internal usage)	void	SetZwilling(Int_t value)	-
Smear a MC-track	Int_t	SmearMCTrack(Double_t dtof, dtof, dphi)	-

Table 3.3: *Using the* `CAL` *format the detector information is converted into track information, which easily can be accessed by the use of the private member functions of* `TofTrackParticle`*. Most of the function names are self-describing, although some are in German (historic reasons). The online documentation found in the net is in English. It is very advisable to use this documentation extensively, since it provides much more information than given in this table. To set the beamtime specific parameters there should always be a call to* `Init(...)` *in global scope to any of the* `TofTrackParticle` *instances first. Some of the member functions also need a call to,* `IsEvaluable(...)` *and* `Eval(...)` *to be usable (see text). These functions are indicated with a "✓" in the last column.*

```
/* 1*/  TofTrackParticle evTP1CMS; // create helping instances
/* 2*/  TofTrackParticle evTP2CMS; // of TofTrackParticles (for CMS-info)
/* 3*/  // exactly two tracks (elastic candidate)
/* 4*/  if(gevTracks->GetTracksTotal()==2){
/* 5*/  TofTrackParticle *evTP1 = gevTracks->GetTrack(0); // get 1st track
/* 6*/  TofTrackParticle *evTP2 = gevTracks->GetTrack(1); // get 2nd track
/* 7*/  if(evTP1->IsEvaluable() && evTP2->IsEvaluable()){
/* 8*/    evTP1->Eval(gMPROTON); // evaluate tracks using the proton
/* 9*/    evTP2->Eval(gMPROTON); // for mass-hypothesis
/*10*/    evTP1->CalcCMSParticle(&evTP1CMS);// calculate corresponding
/*11*/    evTP2->CalcCMSParticle(&evTP2CMS);// tracks in CMS
/*12*/    // when particles 'back to back' within 3deg => elastic
/*13*/    if( TMath::Abs(evTP1CMS.Acolliniaritaet(&evTP2CMS)) <3.0 ){
/*14*/      // get values for further analysis
/*15*/      Double_t  energy1   = evTP1->GetEnergy();
/*16*/      Double_t  momentum2 = evTP2->GetMomentum();
/*17*/      // ... do further analysis  ...
/*18*/      // and fill histograms
/*19*/      hClosestDistance->Fill( evTP1->ClosestDistance(evTP2) );
/*20*/      hThetaDegVsBeta ->Fill( evTP1->GetThetaDeg(), evTP1->GetBeta() );
/*21*/      hThetaDegVsBeta ->Fill( evTP2->GetThetaDeg(), evTP2->GetBeta() );
/*22*/      // ... fill more histograms ...
}}}
```

Figure 3.2: *Example code explaining the usage of* `TofTrackParticle`.

"hard-coded" into the functions which calculate for example the flight-path as a function of the particle angle. In addition, the beam momentum changes for different beamtimes.

To utilize all private member functions, two steps are needed. Firstly, the class has to retrieve the detector geometry and the beam momentum, and secondly, the particle has to be *evaluated*, i.e. the kinematical properties (E, p, γ) have to be calculated using a hypothetical mass assigned by the user. The first is done by a single call to `Init(TofCal*cal, Double_t pbeam)`[3] and the second by invoking `Eval(Double_t masshyp)` for each track. After this, the very comfortable functions to calculate kinematical conversions are accessible (e.g. transformation into the CMS, conversion into `TLorentzVectors`). A summary of all private member functions is listed in Tab. 3.3, where in the last column the necessity for a call to `Eval` is indicated. TofTrackParticles are organized in the same manner as the "ordinary hit classes". All tracks are stored within a `TClonesArray`, which is owned by the track collection class `TofTracks`. The content of `TofTracks` is written to every event in an additional branch of the data tree. `TofTracks` "knows" the number of tracks associated with every event. A "track particle" is retrieved by calling the getter of `TofTracks` which returns a pointer to the track object. This pointer immediately allows to use the

---

[3] The helping parameters within `TofTrackParticle` are all defined `static`, so that *one* call to `Init` is sufficient for *all* particles in a scope.

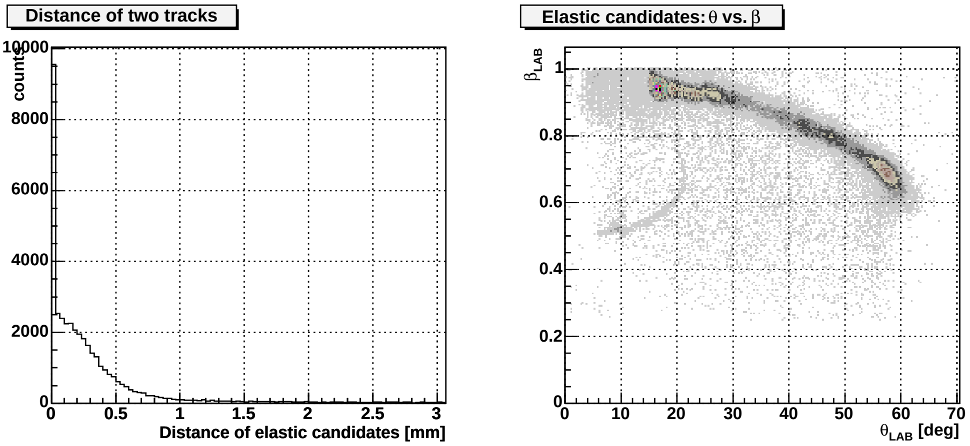

Figure 3.3: *Using the functionality of* `TofTrackParticle`*, a first enhancement of elastic scattered events is possible with very few lines of code needed. Shown above are the two histograms filled with the example code of the previous page. Although a quantitative analysis requires more sophisticated tools (see 5.1) a clear correlation it visible: The majority of events have the same origin within* $0.5\,mm$*; a clear correlation between* β *and* ϑ *is observable (as also is correlated background at* $\vartheta < 20^\circ$ *and* $\beta \leq 0.8$*). (The enhancement at zero in the left picture originates from events where both "tracks" do not have fitting points in the Erlangen-Start. Here, both tracks have their source at (0,0,0), hence the distance between both tracks is zero.)*

member functions, and therefore gives direct access to the physical observables.

Figure 3.2 shows the usage of `TofTrackParticle` by means of a simple example, which can be regarded as a first step to enhance elastic scattered events. First a cut on the total number of tracks is applied (only two tracks → elastic candidate, line 4). After getting the pointer to the tracks (line 5/6), it is checked if both particles are slower then the speed of light[4] (line 7). If true, a mass-hypothesis (proton mass) is used to evaluate the four-momenta (line 8/9) of the particles. Having `Eval`ed particles enables the calculation of the corresponding particles in the CM-frame (line 10/11). An elastic event is defined as an event where both tracks have a deviation of the "ideal back-to-backness" (180°) within 3° (line 13). The physical data is retrieved just by calling the member functions of TofTrackParticle, which then are either copied to local variables for further analysis (line 15-16), or directly filled into (previously defined) histograms (line 19-21). The resulting histograms are shown in Fig. 3.3.

The example demonstrates that the use of `TofTrackParticle` is extremely efficient and easy. The user can directly start the physical analysis, without having to implement the very time consuming and error-prone methods as Lorentz transformation and geometrical calculations. Since the number of needed lines-of-code is small, the size of the source files remain (relatively) manageable as well.

---

[4] Since due to the time-of-flight resolution β *can* be $>$ 1 and $\lim_{\beta \to 1} \gamma = \infty$, it is very advisable to check the track for $\beta < 1$.

3.3 TofAna - The Loop Class

To analyze data, the user has to loop over the `TTree` found in a specific data file. This requires opening the file, obtaining the tree/branches, creation of the data container instances, and the connection of these instances to the branches of the tree. In practice, the loop will include more than one file (one run). Here, the situation is even more complicated since the steps described above have to be carried out for all files. This is not an easy procedure for a beginner, and in general is solved by “copy-and-paste”. Even an experienced programmer will spend considerable time setting up the loop, which prevents immediate proceeding with the actual analysis. To aid the user and to minimize the time needed for such “standard” processes, the loop class `TofAna` was developed. `TofAna` performs all necessary standard steps in order to perform a loop over one or several files. In addition it offers a broad variety of helpful features.

Among others these are:

- Data loop, either for one or multiple files.
- Creation of data containers, connection to the data tree(s).
- Opening and closing of the calibration file.
- Correct calibration data for each run (also if several runs are in one file).
- Reading/writing of *all* or *user selected* branches.
- Reading/writing of *all* or *user selected* events (TEventList).
- Reading/writing of *all* TofRoot data formats (RAW, LST, CALtemp, CAL).
- Run statistics.

These features are extremely helpful for efficient work. Tests with students (having absolutely *no* knowledge about C++ and the TOF-detector) have shown that it takes less than two hours until the student autonomously can declare, define and fill histograms[5].

Getting Started

The implementation of the loop class is distributed over several files, all located in `$TOFROOT_HOME (=/usr/local/tof)`. The files are listed in Tab. 3.4 and can be classified in three groups:

1. The main implementation of the loop class (`TofAna.h, TofAna.C`) is *official*, i.e. not editable to a normal user. Here, all functions which provide and control the loop are located; they can be completely used as a black box.

---

[5] Using TofAna a summer student has programmed two new routines to determine pedestal and binning calibration data within merely two weeks. Both routines are now in official use.

File Name	**Description**
`TofAna.h`	Declaration of "general" and "user" functions (*not editable*)
`TofAna.C`	Implementation of "general" functions (*not editable*)
`UserTofAna.C`	The "user" function implementation
`UserTofAnaDefs.h`	The histogram declaration
`UserInitHistos.C`	The histogram initialization
`mainanaUser.C`	The "main()" function and runtime control
`Makefile`	The makefile (for the loop class and the main program)

Table 3.4: *The* official *and* user *files of the loop class* `TofAna`.

2. User functions are *declared* in `TofAna.h`, but defined only as a dummy in `UserTofAna.C`. Here, the user will place the actual code. To standardize the treatment of the histogram declaration and definition, two other files are forseen (`UserHistoDefs.h, UserInitHistos.C`).

3. The loop will be executed as a compiled program. The file `mainana.C` contains the `main()` function, and a section to influence the execution mode. The `Makefile` compiles the loop class as well as the main function.

To use the loop class, the user first copies all but the `TofAna.h/C` files to his own, private site. An extensive description of how to use these files is found at the beginning of each file . Firstly, the files should be renamed to meaningful names, but leaving the "body" untouched[6]. Then, the makefile has to be edited according to these changes. After this, the `mainana<mytask>.C` file should be edited. A separated section is found in this file, where the behavior of the executable is controlled by "steering parameters". This selects the input/output file names and paths, the treename, the branches to read/write and if an `TEventList` should be used/created. After this, the code should compile and the executable can be launched for the first time[7].

Starting the Analysis

The files `UserTofAnaDefs.h` and `UserInitHistos.C` are foreseen for the histogram declaration and definition. A detailed description and many examples make this part rather self-explanatory. The actual user-code (the algorithms) is implemented in `<mytask>TofAna.C`, where nine functions can be edited. These functions are listed in Tab. 3.5.

In `UserInitRun()` actions should be placed which have to be accomplished prior to analyzing a run, mainly the initialization of user-defined objects and the setting of parameters. This function is called at each "run switch". During the loop, the branches of each event are read according to the settings in `mainana<mytask>.C`.

---

[6] For example: `mv UserTofAna.C mytaskTofAna.C`.

[7] Since no code has been implemented so far, the data is only read from the file. According to the "write-options" set in `mainana.C` the data might be copied in total or reduced to specific branches, however.

The course of action then is explained best by looking at the source code of `TofAna::HandleEvent()`:

```
if(UserCut1()){
   if(UserCut2()){
      if(UserCut3()){
         UserRoutine1();
         UserRoutine2();
         UserRoutine3();
         if(fmakeelist){foutelist->Enter(gevt);}// mark entry in event list
         if(fwritetree){fouttree->Fill();}      // fill tree
}}}
```

The `UserCut[1-3]` functions determine whether the analysis proceeds: if the user returns `kFALSE`, then the analysis of this event is stopped. If all three user-cuts are passed, all three UserRoutines are executed. The actual analysis should be placed here (calculations, filling of histograms). The passing of all the user-cuts also enters this event into an event list[8] and fills the output tree, if these features had been chosen in `mainana<mytask>.C`.

After each event, `UserEndEvent()` is called (regardless of the `UserCut` return values). At the end of the loop `UserEndOutput()` is called. This is the place to implement actions that are desired before ending the executable (write an ASCII-list, write an additional ROOT-file, ...). Before terminating the execution, `TofAna` will write run-statistics to standard output and to a log-file (events/CPUs, total events, total runs, cut-statistics).

Function Name	**Description**
`UserInitRun()`	Initialize global variables and pointers
`UserCut1()`	Analysis only proceeds if return value is `kTRUE`
`UserCut2()`	Analysis only proceeds if return value is `kTRUE`
`UserCut3()`	Analysis only proceeds if return value is `kTRUE`
`UserRoutine1()`	Place to implement code
`UserRoutine2()`	Place to implement code
`UserRoutine3()`	Place to implement code
`UserEndEvent()`	Called after each event
`UserEndOutput()`	Called at the end of the loop

Table 3.5: *The* user functions *of the loop class* `TofAna`*.*

3.4 TofCal - The Calibration Database

The calibration of a beam time collects a wealth of calibration data (offsets, factors, functions). For the application of these data during analysis, two main problems arise:

---

[8] Subsequent analysis can use this list which (eventually) speeds up analysis tremendously.

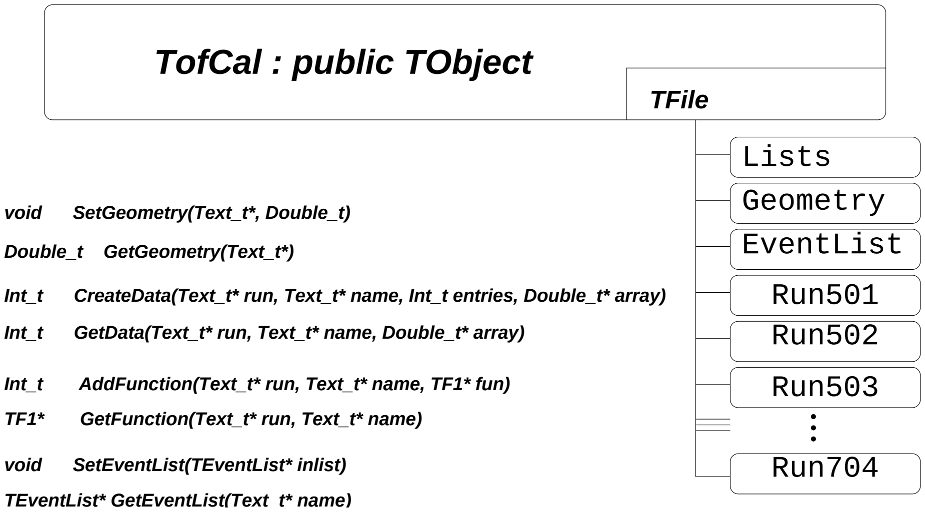

Figure 3.4: *All calibration data is stored in one calibration file (database). Its representation is the class* `TofCal`*. I/O are* "named doubles" *and* "named arrays of doubles"*,* functions *and* `TEventList`*s. A directory structure is used to separate general and run-specific calibration data.*

1. **The *amount* of calibration data:** For a completely calibrated beamtime the total number of calibration constants is in the order of 10^6.
2. **The *management* of calibration data:** It has to be guaranteed that for all runs the full set of calibration data is available. During calibration, conversion, and analysis it has to be ensured that always the correct calibration data is used.

To solve both problems, TofRoot provides the interactive database class `TofCal`[9]. `TofCal` strongly follows the philosophy sketched in the second chapter: A sophisticated and "complex" class layout is used which reflects the complexity of the problem. Yet, the database is accessed easily using *interfaces*, or often may be invoked unconsciously. For example, a `TofCal` object is automatically created when the loop class `TofAna` sets up the loop. The container classes requiring the database are then automatically initialized correctly.

Setup of the Calibration Database TofCal

The TofRoot calibration file uses the versatility of `TFile`, but it adds some special functionality. The data is organized in a file system like structure as sketched in Fig. 3.4. The directory `Geometry` contains all geometric information as sub-detector positions, as well as physical constants (e.g. speed of light, mass of the proton). In the directory `Lists` all calibration arrays constant for all runs are stored, and event lists are collected in the directory `TEventList`. A main feature of `TofCal` are the "run-directories", where run-specific constants are stored. They are dynamically generated

---

[9] 70% by C. Plettner, 30% M. Schulte-Wissermann; rewritten in 2003 by U. Lorenz

and filled during the calibration chain, while the calibration routines communicate with the TofCal-file (see Fig. 2.2). Using the current run number, they automatically read and write calibration values from/to the correct "run directory" of the `TofCal` database. This approach ensures the presence of the full set of calibration constants, for each data file calibrated/converted to the final CAL format.

Usage of the Calibration Database TofCal

Within the `TofCal` class, the calibration constants are stored as *named doubles* or *named array of doubles*, i.e. a name (string) is associated to each value (double, array of doubles). A value is retrieved from the database by simply addressing the name. Data that is constant for all runs is accessed by calling `GetGeometry`[10], while calibration data associated to a specific run is accessed with a call to `GetData`. In the latter case, the "run directory" has to be added to the parameter list:

```
// a value constant for all runs
  Double_t zQUIRL = cal->GetGeometry("zQUIRL");
// a calibration array specific to a single run
  Double_t qdccuthodo[192];
  cal->GetData("Run551","qdcCutsHodo",&qdccuthodo[0]);
```

In addition, `TofCal` provides the possibility to store (and retrieve) calibration *functions*[11], which is extremely useful for Quirl/Ring and Microstrip calibration. The event lists can also be accessed manually, but for most practical cases the automatic management provided by `TofAna` will be sufficient.

3.5 TMatte - The Function Collection

Helpful functions are collected within the TofRoot framework inside the function collection class `TMatte` (matte [ger.][coll.]=math). A list of all functions is shown in Tab. 3.6. The decision to use a class, instead of a function library, was made for three main reasons:

- Having an instance of `TMatte` allows a natural and intuitive usage in compiled executables as well as in an interactive session.
- Some functions of `TMatte` need external input (geometry information). Using classes, an easy way to provide this input is possible: The information is stored in the `TofCal` database and passed to `TMatte` invoking the constructor (`TMatte::TMatte(TofCal* cal)`).
- Automatic online documentation using `THtml` works best for classes.

`TMatte` is an ideal example to explain the TofRoot concept of *soft user-developer separation*: `TofAna` provides a default `TMatte` object (i.e. the pointer `gtmatte`) which is "ready-to-use" in all applications. A new user therefore quickly gets familiar with

---

[10] According to this definition also the speed of light and the mass of the proton is a *geometry*.

[11] Implemented by L. Karsch and C. Plettner

Description	**Return Value**	Function Name
Constructor	TMatte	TMatte()
Constructor using TofCal-object	TMatte	TMatte(TofCal* cal)
Copy constructor	TMatte	TMatte(TMatte&)
Destructor	virtual void	˜TMatte()
Distance of a point to a track	Double_t	AbstandPunktGerade(Double_t* point, TVector3 ap, TVector3 ri)
Beam momentum	Double_t	BeamMomentum(Option_t* beamtime, Int_t runnum)
φ in the barrel (Deg)	Double_t	CalcBarrelPhiDeg(Int_t relss)
φ in the barrel (rad)	Double_t	CalcBarrelPhiRad(Int_t relss)
Calculate $\beta = \beta(p)$	Double_t	CalcBetaFromMomentum(Double_t momentum, Double_t mhyp)
$\Delta\varphi = \Delta\varphi(\varphi_1, \varphi_2)(deg)$	Double_t	CalcDPhiDeg(Double_t phi1Deg, Double_t phi2Deg)
$\Delta\varphi = \Delta\varphi(\varphi_1, \varphi_2)(rad)$	Double_t	CalcDPhiRad(Double_t phi1Rad, Double_t phi2Rad)
Two-body momenta assignment	Int_t	CalcPEinsPZweiDeg(...)
Point of closest approach	Int_t	closestApproach(TVector3* Apunkt1, TVector3* Apunkt2, ...)
Test for elastic scattering	Int_t	CouldBeElastic(TofTorte* evTorte, Int_t howmuch, Int_t maxhit)
Standardized log-file output	Int_t	Cout(Option_t* desc, Int_t nof, Option_t* opt1, Double_t val1, ...)
Get the root-daemon password	Int_t	GetRootdPass(...)
Is track outside target?	Double_t	IsOutsideTarget(TVector3* v3aufp, TVector3* v3ri, ...)
A liner fit	Double_t	linear_fit(...)
Geometric helper (internal use)	Double_t	LotFussPunkt(...)
The normal vector to a plane	Int_t	normaleZuEbene(TVector3* dir1, TVector3* dir2, TVector3* nor)
Print this class	void	Print(Option_t* opt)
Print the Microstrip detector	Int_t	PrintMycroRing(TofMycroStrip* evMy, ..)
Print a `TLorentzVector`	void	PrintTLorentzVector(TLorentzVector* lv, ...)
Align the Torte-Detector	void	TorteAbgleich(TofTorte& evT, Double_t* toff1, Double_t* toff2)
A track search (historic)	Int_t	trackSearch1(...)
The track search (correct version)	Double_t	trackSearch2(...)
Read a standard ASCII-list	Int_t	ReadAsciiList(Option_t *filename, ...)
Update a standard ASCII-list	Int_t	UpdateAsciiList(Option_t *filename, ...)
Write a standard ASCII-list	Int_t	WriteAsciiList(Option_t *filename, ...)

Table 3.6: `TMatte`- *the function collection*

this object and its features. Due to its functionality the personal progress is accelerated and will lead to new developments more quickly. Once this implementation is of general interest, it can be encapsulated into a function and placed into the function collection. In this way, all co-workers can contribute to a common effort.

Chapter 4

Calibration

4.1 Introduction

The data stream produced by the DAQ[1] system at a beamtime generally consists of plain integer numbers which are written to tape in a binary format[2]. The layout of this format focuses on representing the *readout hardware* (crate, module, slot) of the DAQ electronics. This is very important for data acquisition and online debugging. However, for use in offline analysis this format is rather cumbersome and redundant. Therefore, the first step in any analysis is to transform the DAQ data into a convenient offline format. The offline format should focus on representing the *detector hardware*, i.e. from which (sub-)detector the signals originate. In addition, the offline format should be compact, easy to use, portable, and enable to easily convert the raw detector-information (TDC/QDC) into physical observables ($tof, \vec{\beta}, \vartheta, \varphi, \vec{P}, \frac{dE}{dx}, ...$).

Schematically, this conversion can be formulated as:

$$observable = foo(TDC_1, ..., TDC_n, QDC_1, ..., QDC_n, para_1, ..., para_n)$$

where *observable* is any physical observable, $foo(...)$ is a numerical algorithm, $TDC/QDC_{1,...,n}$ represent detector data, and $para_{1,...,n}$ is a *parameter* list. A parameter in general will be a cut-off value, an offset, or a factor. Hence, to obtain (i.e. calculate) a physical observables two main steps have to be undertaken:

- The calibration parameters have to be determined.
- The algorithm ($foo(...)$) has to be implemented.

The whole process leading to the desired physical observables is called *calibration/conversion of the detector data*. Only after this can the “physics analysis” be started. Calibration is the fundament of all data analysis and is anything but an annoying bagatelle. In the past, the time needed for the calibration of TOF data amounted to at least 70% of the total time spent on data analysis. A major aim of TofRoot is to drastically improve this situation by providing a variety of auxiliary means (tools) and by standardizing the algorithms as well as the calibration offsets.

---

[1] **D**ata **A**c**Q**uisition

[2] Until Jan00 TDAS [Schoe97], now EMS [EMS]

Regarding the complexity of calibration/conversion of TOF spectrometer data (≈ 2000 channels in 10 sub-detectors), the question of how to *efficiently organize* this process is of great importance. Efficiency, in this context, regards two different points of view; firstly, the *efficient development* of the needed routines, and secondly, the *numerical efficiency* of the calibration chain (needed CPU-time). Both is guaranteed in TofRoot through the use of four intermediate file formats (RAW, LST, CALtemp, CAL; see Fig. 2.2):

- The contents and the architecture of these file formats are strictly defined. Having these fixed file-formats as input, calibration routines can fulfill self-contained tasks independent of the beamtime. Furthermore, their implementation can easily be assigned to different co-workers.

- CPU-consuming algorithms during the conversion from one format to the proximate are executed only once. Subsequent analysis therefore proceeds from an already elevated level.

Starting with the RAW format, the conversion from one format to the proximate is always a two step process. The first step is to *accumulate* the calibration data and store it in the `TofCal` database. This is done by calibration routines (mainly programs) which are launched successively. The second step is to then *apply* the calibration data: The data is read from one format, converted using the data found in the `TofCal` file, and written to the proximate format.

The calibration of the TOF-detector data using TofRoot will be described[3] using the beamtime of January 2000 as an example. The data of this beamtime is then used for data-analysis in the second part of this work.

4.2 The RAW Format

The first step in data analysis is to convert the data collected in Jülich into a TofRoot format. This is a simple conversion process, where the data is read from tape and the TDC/QDC conversions and rss (**r**elative **s**ignal-**s**ource = photo-multiplier-ID) values are filled into the according container classes. In addition, a header class (`TofHeader`, associated with the branch `bHeader`) is filled with the event number, the trigger pattern, and the run number. Scalers are written to a special `TofScaler` class (branch: `bScaler`). The tree with the filled branches is then made persistent, i.e. written on the hard disk. No cuts are applied (no data reduction) and the data is not manipulated in any way[4]. The contents of the RAW-files can be analyzed easily using the loop-class `TofAna`. For quick and easy control, all "standard histograms" (each TDC/QDC channel, correlation spectra) are written to the *same* file (see Fig. 2.4). These histograms can easily be displayed interactively using the TofRoot-tool `histoanguck_GUI.C`.

---

[3] This word is to be taken literally: The amount of calibration routines prohibits a deeper discussion. For further information or to view the actual implementation, please refer to the online documentation found at `http://kp.phy.tu-dresden.de`.

[4] To be consistent with the other formats, the TDC/QDC values are converted from Int_t to Double_t.

4.2.1 Calibration Routines Reading the RAW Format

Walk, Pedestal, Binning Calibration

The first step in each offline analysis is the walk, pedestal, and binning correction. For the January 2000 beamtime, the calibration values were acquired using the old offline framework (XD). Meanwhile, routines for these calibration steps were developed[5] and have already been used for the 2002 measurement series.

Although very important, these three calibration steps are rather standard tasks and are described in detail in [Jac01].

Curing the De-Correlation of the Barrel Detector

In the beamtime of January 2000 the DAQ had a severe problem with the Barrel detector: While the TDC information was correctly written to the event n, the QDC information was written to the event $n + i$ ($n, i =$ integer; $i \in [0, 10]$). Since the RAW format is a one-to-one translation of the DAQ data, this behavior also became manifest in the RAW-file. Due to the possibility of `TTree` to read data in any order, it was easy to scan the data for this effect. While starting with correlated TDC-QDC pairs, at some event the de-correlation occurs. The routine then scans the next events until the QDC-values are found. The event-number where a de-correlation occurs for the first time (n) and the “de-correlation depth” (i) are stored in the `TofCal` file. This information is used to remedy the de-correlations during the conversion to the next (LST) format (`ApplyList`).

QDC-Cuts (Quirl, Ring)

The DAQ system only writes non-zero TDC values into the data stream if the signal surpasses an individual discriminator threshold. This is different for QDCs: due to the charge integration of the baseline, QDCs always show a (positive) conversion. All QDCs contribute to the data stream which leads to a narrow, and “non-physical”, peak at small QDC values in the raw spectra; the so-called pedestal. To not thwart the DAQ, the writing of the pedestal is suppressed online. In general this suppression is very modest, so that still much more QDC than TDC values are written to tape. In addition the Quirl/Ring hodoscopes have a slight tendency for (physical) cross-talk. Light leakage and δ-electrons may trigger a (small) signal in a neighboring channel. Both effects lead to severe problems during offline analysis: Firstly, the number of hits exceeds the number of actually detected particles, and secondly, the writing of useless pedestal data also inflates the amount of needed disk-space.

Therefore, individual minimal QDC-conversions (cut value) for each channel have to be determined. In principle it would be possible to find a heuristically motivated calibration routine which examines the histograms and automatically generates a QDC-cut-value for each channel. But tests have proven that for this task the human eye is much more error-proof than automatic evaluation. A simple, but effective macro has been implemented[6] which displays the Quirl/Ring QDC-histograms one-by-one. Us-

---

[5] By two summer students

[6] By L.Karsch

ing the mouse, a “click” into the histogram defines the cut-value, which then is written to an ASCII-list and into the TofCal-file. After this, the next histogram automatically appears to the physicists eye. Considering that we have to analyze $(192 + 96 = 288)$ channels, this procedure needs less than 30 minutes ($6s/histo$) to evaluate the QDC cut values for the Quirl and Ring detector.

4.3 The LST Format

Generally speaking, LST format means that the first calibration **LiST**s are applied. The name has historic character: It originates from the time when calibration data was extracted from ASCII-lists (and not from the TofCal-file). For a “simple” experimental setup (low energy, no Erlangen-Start) the LST format can be considered as the real basis for data analysis. Since the LST format is easy to produce, it is largely used *online* at a beamtime as well. Detailed checks for the sanity of the detector system and first (physics) analysis use this format as input. However, for more complex setups (e.g. January 2000) and detailed analysis, additional calibration is inevitable. Here, the LST format should be considered just as one of the four TofRoot data formats.

4.3.1 Converting RAW to LST: Apply Standard Lists

The program `ApplyList` converts RAW into LST format. It reads the calibration data from the `TofCal` file and applies the walk, pedestal, and binning correction. In addition, the data is purified from background using the QDC-cuts (Quirl/Ring), the coincidence of TDC/QDC pairs, and the total amount of hits in the event.

A summary of what is accomplished by ApplyList, and therefore found in *any* LST file, is given in Table 4.1.

1	Apply the walk-, pedestal-, and binning data
2	Remedy the Barrel de-correlation
3	Invert the TDC value if the DAQ was operated in common-stop mode
4	Add a random number ([0,1[) to each TDC/QDC value to avoid digitalization
5	Apply QDC cuts for Quirl/Ring detector
6	First pixel search in Quirl/Ring (up to 2 pixels per detector)
7	Remove all hits with (`TDC<=0 || TDC>TDCoverflow || QDC<=0`)
8	Remove all events with “pathologic” number of hits (e.g. $>$ 20 hits in the Barrel)
9	Write scaler-events into the TofCal database
10	Provide log-file output (ASCII)
11	Fill all standard histograms

Table 4.1: *Tasks fulfilled by* `ApplyList` *(RAW2LST). This* definition *is valid for* all *LST files and* all *beamtimes.*

4.3.2 Calibration Routines Reading LST format

TDC Alignment of the Torte Detector

The Torte (torte [ger.]=tart) detector consists of two consecutive scintillating rings, each divided into 12 “tart-pieces” [Wag97]. The two “sub-tarts” are twisted by half a “tart-width”, resulting in an overlap of each segment with two in the other layer. The Torte is the first detector encountered by the reaction products and provides the TDC reference for all time-of-flight measurements. In order to calculate the-time-of flight (TOF) of a given particle, it is necessary to subtract the time (TDC) of the stop component from the time (TDC) of the Torte detector. Since the Torte consists of two consecutive layers, a (charged) particle will in general produce two hits. To improve the time-resolution, the Torte-TDC value can then be calculated to be the arithmetic mean ($TDC_{mean} = (TDC_1 + TDC_2)/2$) of both TDC conversions. However, due to different cable lengths and different transit time in the photomultipliers, the time information of each segment is shifted by some constant offset. To align all Torte-TDCs, it is necessary to correct this effect and to shift the TDC values by 24 (individual) offsets. After this, all TDCs will have the same (within resolution) conversion for an event which occurred at the same time.

To evaluate these offsets, the TDC *differences* of all *overlapping* segments are filled into histograms. This yields 24 time differences between the segments, from which the 24 TDC offsets can be determined in a self-consistent way. As the result, the time of flight now can be calculated using:

$$\mathtt{tof} = \mathtt{TDC_{Stop}} - ((\mathtt{TDC_i} + \mathtt{off_i}) + (\mathtt{TDC_j} + \mathtt{off_j}))/2.;$$

Using the LST format as input, helping functions as `TMatte::TorteAbgleich(...)` and `TofTorte::SearchTorteRad(...)` are implemented to easily retrieve the needed values ($\mathtt{TDC_i}$ and $\mathtt{TDC_j}$). These functions also are frequently used in the subsequent calibration routines.

The determination of the TDC-offsets is carried out for each run calling the program `tortenabgleich`. The advantage of calibrating each run rather then taking constant offsets for the whole beamtime, is shown in Fig. 4.1, where the shift of a Start calibration value (relative to run 551) is monitored over all runs of the January 2000 beamtime. It shows a significant shift of over two channels. Considering that the time-of-flight accuracy[7] should be well below one channel, using constant offset values would make this aim difficult to reach.

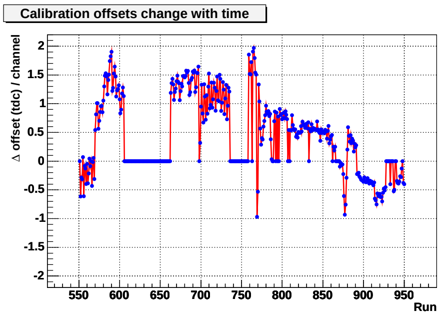

Figure 4.1: *Torte TDC offsets: Example of calibration offsets changing with time.*

---

[7] Error of the mean value, not the RMS.

Quirl and Ring Calibration

The Quirl and Ring detectors consist of three consecutive layers of scintillating material: a "straight-layer" and two (left/right) "wound layers" [Dah95]. In most cases a particle will trigger a signal in all three layers, which defines a "three-hit" pixel. However, due the spacing of the segments and to crosstalk, some events may have only two or even four hits (two/four-hit pixel). The relative signal sources (rss) of the triggered layers have an isomorphic relation to a pixel with a radius r and an azimuthal angle φ. The correlation between these rss-multiplets and r, φ is achieved by the use of look-up-tables[8]. A first pixel search was already performed during the conversion to the LST format (`ApplyList`). However, the search is limited to a maximum of two pixels (particles) per sub-detector, and may be sufficient in low-energy experiments ($\approx 800 MeV/c$) where only few particles are involved (e.g. $pp \rightarrow pp\pi^0, pp \rightarrow pp\gamma$). It is not sufficient for experiments near the COSY-limit ($\geq 2500 MeV/c$). Here, too many reaction products are involved, hence a limitation to only two pixels would critically cut into "event space".

An expansion of the pixel search to more than two pixels per event is not trivial, since the chance of assigning combinatorial ("ghost") pixels grows rapidly. A completely new pixel search, in conjuction with an improved calibration, has been implemented[9] which also utilizes the time information (TDC) of each layer: The transition time through the detector can be neglected. Therefore, a *true* pixel will have the same time information in all triggered layers. Prior to using the time information of the Quirl/Ring detectors, both detectors have to be time-calibrated: Firstly, an internal TDC-alignment of all layers has to be accomplished and secondly, corrections for the different radial distances to the readout devices have to be applied. These two steps are implemented in calibration programs (`quirltof/ringtof` and `quirlabgleich/ringabgleich`) and the result is stored in the TofCal database[10]. A true pixel is now defined as a combination of two, three, or four rss's found in `UPixel` *and* a consistency of the time information of all layers. The found pixels are stored in the class `T<Quirl/Ring>Pixel`, which is written to a `TClonesArray` in parallel to the hit-class (`TofQuirlHit`). A set of useful member functions as `GetPhiDeg()`, `GetThetaRad()` and `CalcXYZ(...)` allow quick and comfortable analysis.

The time calibration of all Quirl/Ring channels (all three layers) has another major advantage. It is now possible to use the (combined) TDC information of *all* layers ($TDC = (TDC_1 + TDC_2 + TDC_3)/3.$), which considerably improves the time resolution of the stop-signal, hence the resolution of the time-of-flight. The average TDC value is easily obtained using the function `Tof<Quirl/Ring>Pixel::GetMeanTdc(...)`.

COSYnus - the Neutron Detector

The neutron detector COSYnus detects neutral particles in $200 \times 10 \times 10\, cm^3$ scintillating bars, which have the forward region covered by thin "veto paddles" to discriminate

---

[8] In TofRoot the tables are wrapped in the `UPixel` class which resides in the `libReko.so` library (by C.Plettner)

[9] By Leonhard Karsch as described in [Kar04].

[10] The possibility to store *calibration functions* in a `TofCal`-file is extremely comfortable here.

against charged particles. The detector is time- and position-calibrated by several calibration routines exclusively implemented by L.Karsch. Since the COSYnus detector was not used for this work, for further information please refer to [Kar99] and [Kar04].

First Barrel Calibration

For the (first) calibration of the Barrel, elastically scattered events are used. Elastic scattering events have the advantage of a high total cross section[11]. This leads to a high abundance of this reaction type in the data and therefore minimizes statistical uncertainties during calibration. Another advantage is that they are *two-prong* events: Assuming the reaction to be an elastically scattered proton-proton event, momentum conservation enables the *calculation* of all physical quantities (ϑ_2, $\vec{p}_{1,2}$, $\mathtt{tof}_{1,2}$), if the polar angle ϑ_1 of *one of the elastic partners* is measured[12]:

$$\vec{p}_1 = p(\vartheta_1, p_{beam}) \tag{4.1}$$

$$\vec{p}_2 = \vec{p}_{beam} - \vec{p}_1 \tag{4.2}$$

$$\vartheta_2 = \arctan(\sqrt{p_{x_2}^2 + p_{y2}^2}/p_{z_2}) \tag{4.3}$$

$$\mathtt{tof}_{1,2} = tof(p_{1,2}, geom, m_p) \tag{4.4}$$

where m_p is the mass of the proton (mass hypothesis) and *geom* is the "geometry" of the detector setup, respectively.

Due to the setup of the TOF detector (January 2000), the two prongs of elastically scattered events lead to either Ring-Barrel or Barrel-Barrel coincidences. These coincidences are used to calibrate the Barrel detector in two steps:

1. Ring-Barrel coincidences are used to calculate the *expected position* and the *expected time-of-flight* in the Barrel detector. Input to this calculation is the polar angle measured in the Ring detector. The output of the calculation ($\vartheta_B, \mathtt{tof}_\mathtt{B}$) is compared to the value measured by the Barrel. The calibration offsets of the Barrel are shifted until measured and calculated values coincide. Ring-Barrel coincidences only cover the angular range of $\vartheta_B > 45°$ in the Barrel.

2. The forward region ($25° < \vartheta_B < 45°$) is calibrated using Barrel-Barrel coincidences. The Barrel information thereby is obtained using the calibration list derived in the first step. Both prongs are measured with considerable uncertainty and "heuristically motivated" methods are used to simultaneously adjust the calibration values.

During the development of TofRoot it became clear that using the "track-information" of the Erlangen-Start allows a calibration of much higher quality. The calibration obtained here will be used as a starting point for the (final) Barrel-calibration, which takes the CALtemp format as input (see p. 58).

---

[11] In fact, to not dominate the data stream the "elastic trigger" is scaled down by a factor of 2^8 during normal data acquisition.

[12] see 5.1

QDC-Cuts for the Erlangen-Start

The Erlangen-Start (Microstrip, Big- and Small-hodoscope) provides only QDC readout[13]. This has a severe drawback: It is not possible to purify the triggered hits by requiring a coinciding TDC-conversion. Since the QDC-cuts applied during data acquisition are modest pedestal suppression cuts, the mean number of hits per layer is in the order of ten. The combination of both layers then leads to a possible number of pixel per event and sub-detector in the order of 100, which is as impractical as physically wrong.

As a first step to remedy this situation, QDC-cuts are determined for each channel by a macro similar to the Quirl/Ring QDC-cut determination (see 4.2.1). The numerical values of the cuts are stored in the `TofCal`-file and applied during the next conversion step `LST2CALtemp`.

Search for "Defunct Channels" in the Erlangen-Start

Some channels in the tracking-devices of the Erlangen-Start do not operate properly ("defunct channels"). Although the number of defunct channels (about seven in the beamtime of 2000) is small compared to the ≈ 800 total channels, it is important to know which channels are affected:

1. For particular analyzes, a missing channel may considerably change the performance of the spectrometer: A defunct channel near the beam axis will have a large effect for ejectiles kinematically constrained to small angles; polarization measurements crucially rely on azimuthal symmetry. Therefore, for acceptance correction, the defunct channels have to be known and incorporated in the Monte-Carlo-simulation.

2. During the conversion to the next format (CALtemp), *consecutive* hits in the layers of the Erlangen-Start detectors will be combined to clusters. In particular for the Microstrip detector, the knowledge of defunct channels is important: The charge freed by a particle passing through a defunct segment is divided between the two active neighboring channels. Without proper treatment, this would simulate the physical presence of *two* particles, but both at a wrong position.

To evaluate the defunct channels, the hits in all three Erlangen-Start-detectors are counted[14]. Channels with a total count less then 1% of the average value are defined as defunct. The retrieved information is stored in the `TofCal` database and later used in cluster analysis and for Monte-Carlo simulation.

4.4 The CALtemp Format

The CALtemp (**CAL**ibrated **temp**orarily) format was introduced because, at a certain point, the implementation of TofRoot became too complex to be organized in an efficient, team-oriented way. Simply put, too many developments were pushed in

---

[13] Since October 2002 one of the hodoscopes (the Big-hodoscope) is also equipped with TDCs.

[14] For convenience, this routine is currently implemented at the beginning of lst2CALtemp.

parallel. A “secure haven”, i.e. a defined and frozen data format, had to be agreed upon, from which further developments could be pushed forward.

The *definition* of the CALtemp format - accomplished conversion and provided calibration data - is shown in Tab. 4.2. The “standard histograms” can be observed using the macro `caltemp_anguck.C`[15].

1	Torte offsets applied
2	Defunct channels found and stored in `TofCal` database
3	Quirl, Ring and COSYnus are calibrated
4	Hits in the Microstrip are converted to clusters/pixels
5	Hits in the hodoscopes (big/small) are converted to clusters/pixels
6	Log-file-ASCII output
7	Standard histograms

Table 4.2: *Definition of the CALtemp format.*

4.4.1 Converting LST to CALtemp: Preparing the Erlangen-Start

The conversion of the LST to the CALtemp format is performed using the program `lst2CALtemp`. The main task of this program is to prepare the Erlangen-Start-data for the track-search routines used in the next (and final) conversion step. A detailed drawing of the Erlangen-Start is shown in Fig. 4.2.

TDC Alignment of the Torte-detector

Up to now, the TDC-offsets determined in 4.3.2 had to be applied manually, before using the TDC-information of the Torte-detector. Beginning with the CALtemp format this is not necessary any more: The Torte offsets are applied to the TDC-values and written *with these changes* to file. This means, that starting with CALtemp, the user can utilize the found TDC-values *as is*, i.e. without having to deal with any TDC-offsets.

Cluster in the Erlangen-Start

Due to cross-talk, or by particles *physically* passing through neighboring fibers/strips, a charged particle (often) will trigger more than one channel in each layer of the Erlangen-Start detectors. The cluster-search therefore scans each event for *consecutive* hits and combines them to clusters. In the hodoscopes, clusters of up to three hits are searched for, while in the Microstrip a cluster can consist of a maximum of four hits. More than three (four) consecutive hits are divided into separate clusters. The cluster information is stored in a cluster-container-class (e.g. `TofHodoCluster`), which contains the cluster information as well as all information of the original hits. Besides purifying the data, using clusters offers another advantage: The QDC-values of each

---

[15] This tool is very recommendable, especially when converting data of a new beamtime or comparing Monte-Carlo data with experiment.

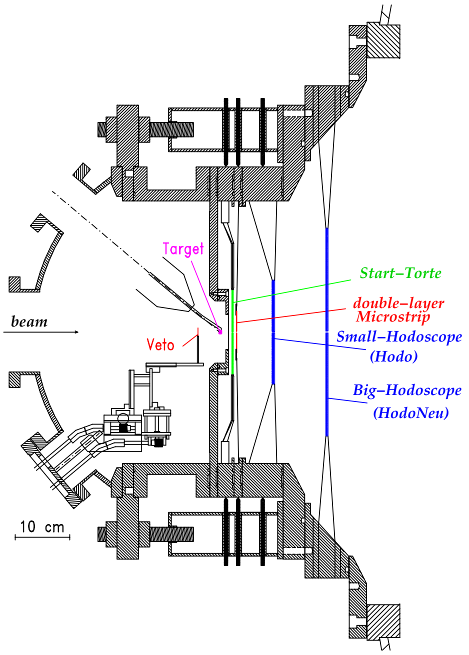

Figure 4.2: *The Erlangen-Start detector is a modular tracking device which consists of four sub-detectors: The Start-detector (Torte) for "start-time" information and the three tracking devices: the double layer* μ*-strip detector (Microstrip) and two fiber hodoscopes; the Small- and the Big-hodoscope (in TofRoot called: Hodo and HodoNeu).*

The Torte consists of 2×12 *scintillating tart pieces. Its efficiency is near 100% in an angular range from* $\sim 3^\circ < \vartheta < 76^\circ$*. The double-layer Microstrip placed in direct vicinity to the Torte provides a high-precision position information. The first layer consists of 100 "tart" segments, while the second consists of 128 concentric rings. The small and the big hodoscopes consist of two crossed layers, each* $(2 \times 2\,mm^2$ *scintillating fibers, 96+96/192+192). The geometric acceptance for track-reconstruction reaches* $\vartheta \approx 45^\circ$ *and the efficiency of each tracking-detector is* $\approx$*90%.*

hit of a cluster can be used to calculate the *mean* hit-position within a detector layer:

$$\texttt{meanRSs} = \frac{\sum_{\mathrm{i}=0}^{\mathrm{n}} \mathrm{QDC_i} * \mathrm{rss_i}}{\sum_{\mathrm{i}=0}^{\mathrm{n}} \mathrm{QDC_i}}, \tag{4.5}$$

where `meanRSs` is the weighted average of the relative signal sources; n is the number of hits in the cluster; and QDC_i, rss_i are the conversions and channel numbers of the i^{th} hit, respectively. Using `meanRSs`[16], removes the discrete (hit) structure of the Erlangen-Start-detectors and leads to a continuous (cluster) distribution.

Pixel in the Erlangen-Start

Let us consider three charged particles passing a two-layer detector. In an ideal case, three separated clusters within each layer will be triggered. Through the use of simple combinatorics, we find $(3 \times 3 =)$ 9 possible points of intersection: nine possible pixels. This ambiguity is not reducible considering only one detector alone[17]. In fact, only the *combination* of all detector information, as done during the track search, can clarify the picture (see p. 60). To store *all possible* pixels (cluster combinations) in a pixel-class is prohibited simply by file size. Therefore a different approach was chosen, enabling *dynamic calculation* of pixel information on-the-fly: The found clusters (e.g. `TofHodoCluster`) of each layer are written to a pixel-class (e.g. `TofHodoPixel`),

---

[16] Which are not integer, but `Double_ts`!

[17] In principle, the QDC-values could be used: In the Microstrip the charge should be divided to equal part on both layers; in the hodoscopes the signal height should be related to the energy deposit of the particle (type, velocity) and the distance to the photomultiplier. This should be subject to further studies.

where the clusters are stored in `TClonesArrays`[18]. With this, the pixel-class has access to the information of all clusters, in particular to the `meanRSs`s. The intersection of two clusters (two `meanRSs`s of two layers) define a pixel, and the properties of this pixel ($\vartheta, \varphi, ...$) can be parameterized as a function of the `meanRSs`s of both clusters. To access the pixel properties, the pixel class provides a variety of powerful and sophisticated member functions, e.g. `CalcPhiDeg`($\texttt{rss}_\texttt{x}, \texttt{rss}_\texttt{y}, ...$), `CalcXYZ`($..., \texttt{rss}_\texttt{x}, \texttt{rss}_\texttt{y}, ...$)), and `FindBestPixel(`$\vartheta, \varphi$`,...)`. These functions will be largely used during the position calibration of the Erlangen-Start described in the next section, as also during the track search.

4.4.2 Calibration Routines Reading the CALtemp Format

Position Calibration of Erlangen-Start

The numerical backbone of most functions calculating pixel properties is `CalcXYZ`(...), which calculates the pixel position within the TOF-detector coordinate system. The knowledge of (x,y,z) enables the calculation of other pixel properties by simple algebra. For example, the polar and azimuthal angles can be calculated according to:

$$\vartheta \quad = \vartheta(xyz) \quad = \arctan(r/z) = \arctan(\sqrt{(x^2 + y^2)}/z) \tag{4.6}$$

$$\varphi \quad = \varphi(xyz) \quad = \arctan(y/x) \tag{4.7}$$

However, the calculation of the pixel-position (x,y,z) itself is not trivial, and is implemented as a three-step process:

1. The *relative* hit position (x,y) within a Erlangen-Start-detector coordinate system is calculated using the `meanRSs`s of both triggered clusters. This is a simple numerical problem[19].
2. The relative position has to be shifted/rotated according to the *global* position/angle of each detector, i.e. as it is physically mounted in the TOF-spectrometer.
3. An additional correction due to the finite dimensions of the scintillating fibers is necessary. This will be discussed in the next section.

The global position of each Erlangen-Start-detector is parameterized by four calibration constants: the *shift* of the sub-detectors with respect to the target center ($\Delta x, \Delta y, \Delta z$), and the *twist* ($\Delta\varphi$). Of course, these global positions are known prior to the experiment through manual measurements and engineering drawings, but their accuracy is far from being sufficient: In fact, the determination of the (global) position - within an uncertainty in the order of a *tenth of a millimeter* - is of paramount importance for the subsequent track-search routine.

To calibrate the positions of the Erlangen-Start detectors, the member functions `Tof<Mycro/Hodo/HodoNeu>::CalcXYZ(...)` provide a very helpful feature, which

---

[18] This is the same architecture as the so far used `TofHodo/TofHodoHit` constellation (see 3.1).

[19] Position of n^{th} fiber: $x_{rel} = x_0 - n \cdot d_F$
($n =$ `meanRSs`; thickness of a fiber: $d_F = 2mm$; position of fiber 0: $x_0 = 95\,mm$, $n = [0, 95]$)

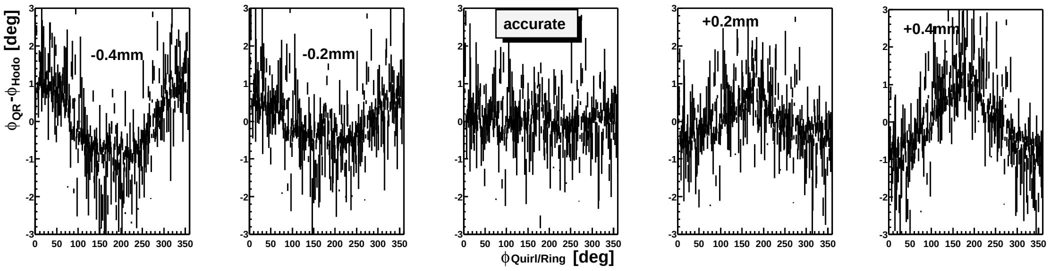

Figure 4.3: *The position calibration of the Erlangen-Start-system using the hodoscope as an example. Shown is the angular difference ($\Delta\varphi = \varphi_{Q/R} - \varphi_H$) between the Quirl/Ring and the hodoscope measurements. The "exact" position is shown in the middle, whereas for the other plots the x-position was shifted by* ± 0.2 *and* $\pm 0.4\,mm$*, respectively.*

schematically can be sketched as:

$$\overrightarrow{xyz} = xyz\ (\ \overbrace{rss_1, rss_2}^{\text{cluster info}},\ \underbrace{\Delta x,\ \Delta y,\ \Delta z,\ \Delta\varphi}_{\text{fixed \& provided by }\texttt{TofCal}},\quad \overbrace{dx,\quad dy,\quad dz,\quad d\varphi}^{\text{additional offsets during calibration}}\quad)$$

The two $rss_{1,2}$ are the actual input (`meanRSs`) and the global positions (the Δs) are taken from the `TofCal` database. However, these positions will be slightly wrong, beginning the analysis of a new beamtime. Therefore, additional offsets ($d_{x,y,z,\varphi}$) can add to the global positions; they are provided "manually" and are used only for calibration.

The general concept of the position calibration of the Erlangen-Start is to compare the angles (ϑ, φ) measured in the stop-components (Quirl/Ring/Barrel) with the values found in the Erlangen-Start. The differences (e.g. $\Delta\varphi = \varphi_{Quirl} - \varphi_{Hodo}$) are monitored in histograms, which then are filled for different sets of "additional" offsets. This leads to an iterative process until, finally, the optimum position of each detector is deduced. Figure 4.3 shows the result. Here dx (the additional offset) is set to $-0.4, -0.2, 0.0, 0.2$ and $0.4\,mm$, while all other positions are at optimum. The picture shows the dramatic effect of even a small misalignment: Varying one offset by $0.2\,mm$ results in an error of the azimuthal angle in the order of $\pm 1°$.

Additional Correction for the Hodoscopes

The hodoscopes consist of two crossed layers of scintillating fibers, where each fiber has a cross section of $2\,mm^2$. Due to these finite sizes of the fibers, particles with inclined angles need an additional correction as shown in Fig. 4.4: The particle (black arrow) hits the first layer (x) "in parallel" with the fiber, which is only possible if it passes the central fiber. Hence the x-information provided by this layer is zero ($x = 0$). Due to the inclined angle, the particle passes two fibers of the y-layer. Since the position (`meanRSs`) is calculated from the weighted average of the QDC conversions, the measured y-position will lie between both fibers. A look at Eq. 4.6 reveals that, in this case, the determination of the radius ($r = \sqrt{x^2 + y^2}; x = 0$) is totally dependent

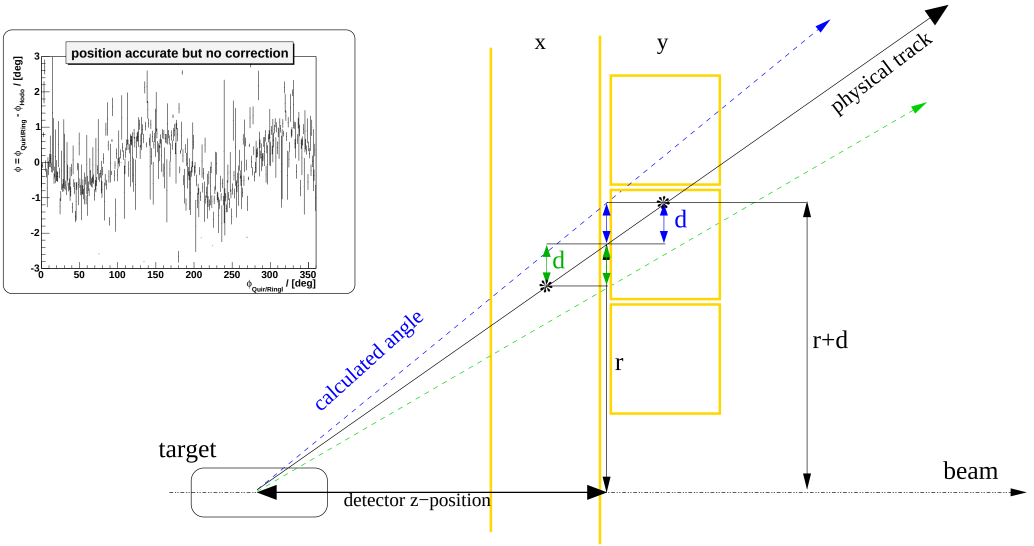

Figure 4.4: *The Erlangen-Start consists of two crossed layers of scintillating fibers (gold). Depicted here: The first (x) layer is in parallel and the second (y) is perpendicular to the picture plane. Due to the inclined angle of the particle, the measurement of y is "too big" and leads to an error in the calculation of the polar angle (blue). However, turning the detector (or the particle) by* 90° *around the z-axis revolves this effect and the x-layer underestimates the x-position (green). Hence, we find an error of the x and the y value, which is also dependent on the azimuthal angle of the particle. Without correction, this leads to a cyclical error of $\vartheta = \vartheta(\varphi)$ and $\varphi = \varphi(\varphi)$ using the equations 4.6 and 4.7. The magnitude of this effect is shown in the upper left: Without correction the azimuthal angle is miscalculated in the order of* $\pm 1°$.

on the position measurement in the second layer (y). If we define the z-position of the detector to be between both layers, the calculated angle ϑ is wrong (blue arrow): The z-position of the radius-measurement does not match the defined z-position of the detector; the y-position (hence, the radius) is overestimated by the additional distance d. To correct for this effect, in Eq. 4.6 either the z-position has to be set to the middle of the second layer, or the y-value has to be corrected for the additional distance d. It was chosen to correct for the latter, since (intuitively) a detector is believed to have *one*, fixed z-position.

It is important to mention that both layers are affected: Turning the detector (or the particle) by 90° around the z-axis interchanges the roles of the x- and y-layer (green arrow). Hence, the error of the measurement of x *and* y is not only depending on the polar but also on the *azimuthal angle* ($\Delta x = \Delta x(\vartheta, \varphi)$, $\Delta y = \Delta y(\vartheta, \varphi)$). This leads to a miscalculation of the *azimuthal angle* as well. The strength of this effect is shown in Fig. 4.4 at the left, where the difference of the measured angle in the hodoscope and the Quirl is plotted against the azimuthal angle. Here, the correction was not applied, but the detector position is correct (same as Fig. 4.3 in the middle). Without correction, a two-fold cyclical miscalculation of φ in the order of $\pm 1°$ is inevitable. Although apparently an important effect, it was never taken into account by any preceding analysis package.

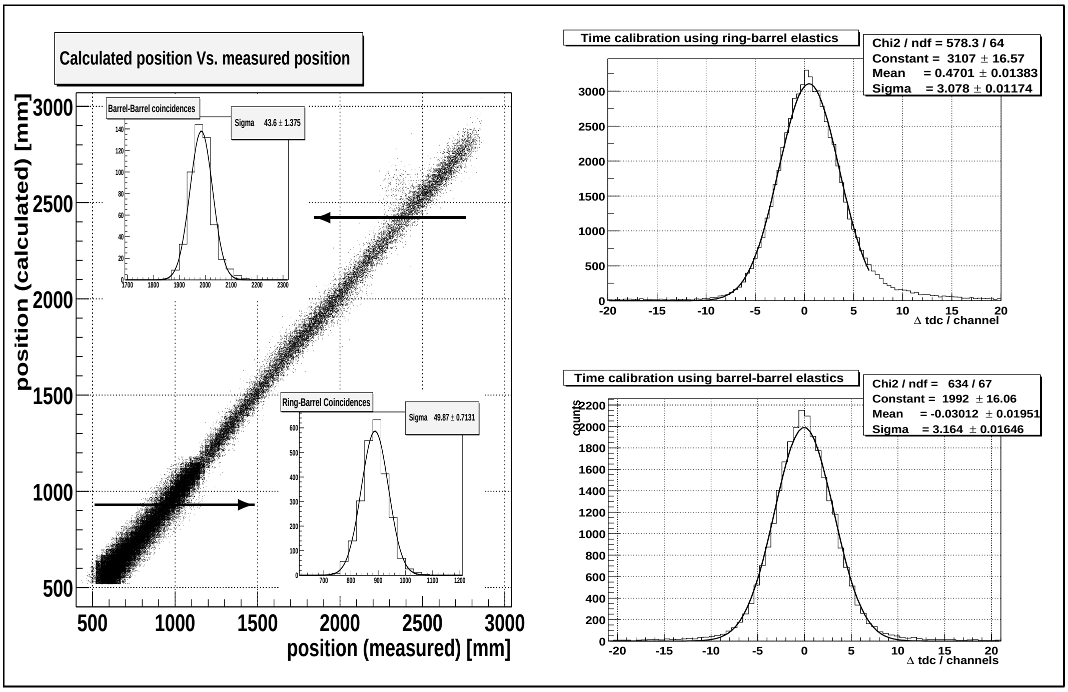

Figure 4.5: *Results of the Barrel calibration for the Ring-Barrel and Barrel-Barrel coincidence regions. Left: The position calculated from the "track information" is plotted against the position measured with the Barrel. The small figures represent projections (as indicated by the arrows). Right: Difference of the time-of-flight calculated from the ϑ-angle (track) subtracted from the measured time-of-flight in the Barrel.*

Barrel Position and Time Calibration

Although tracks (`TofTrackParticle`) are not present in the CALtemp format, the position- and time-calibration of the Barrel is the first application of the pixel information in the Erlangen-Start. The pixel information together with a linear fit is used to "manually" calculate[20] "tracks" (ϑ, φ), after which the direction of a particle is known to a higher precision.

The Barrel calibration mainly uses elastically scattered events, and follows the procedure presented in 4.3.2, but, due to tracking, with an enhanced performance: Using "track" information, the polar angles of particles hitting the Ring detector now are known to a *higher precision* and have a *continuous* distribution; and from this information the angles of the particle hitting the Barrel is calculated using the Equations 4.1-4.3. Hence, the calculated angular distribution of the elastic partner is known with a higher precision and is continuous as well, which already improves the calibration quality. However, Ring-Barrel coincidences only cover the Barrel at $\vartheta > 45°$. The region from $25° < \vartheta < 45°$ has to be calibrated using Barrel-Barrel coincidences. Here, *no* particle angle was formerly measurable with satisfactory precision. Heuris-

---

[20] Historically, this is the nucleus of the track-search routines later used in 4.5.1.

tically motivated methods had to be used to perform a simultaneous calibration of both Barrel-hits. Using "tracks" in the Erlangen-Start enormously simplifies matters: *Both* particles are within the angular acceptance of the tracking detectors. Hence, the direction[21] of each track now is actually *measured* and can directly be used for calibration.

The position[22] and time calibration of the Barrel is accomplished by a set of programs residing in the `$ROOTSYS/BarrelCalib` directory. To minimize statistical uncertainty they should be launched for a set of at least 100000 elastic events. For most cases, this implies a loop over more than one run and should be set in the main *run-script* (`RunRAW2CAL`). The output (offsets) is automatically stored in the `TofCal` database and later used by the track-search algorithm.

The result of the Barrel calibration is shown in Fig. 4.5. In the left, the difference of measured and calculated position on (all) Barrel bars is shown. The broadened section below $1200\,mm$ belongs to Ring-Barrel coincidences, where only one "track" has pixels within the Erlangen-Start. Utilizing Barrel-Barrel events improves the picture. The uncertainty of the position measurement in the Barrel is found to be better than $\sigma = 35\,mm$[23] over the full angular range. The result of the Barrel time calibration is shown in Fig. 4.5 on the right, where the difference of measured and calculated time-of-flight is shown. The output is a Gaussian with a standard deviation of $\sigma = 3.1$ channels ($310\,ps$), which reflects the hardware resolution of the TOF-detector itself (see 5.3).

Angular Dependence of the Time-Information in the Torte Detector

The Torte detector consists of 24 trapezoidal scintillator pieces with a photomultiplier located at the outer end of each segment. Particles passing the Torte at different polar angles produce light at different distances to these readout devices. Hence, depending on the polar angle, the produced light will experience different *transit times* within the Torte detector. In the angular range of the Barrel detector, the maximum difference in transit time is in the order of three TDC-channels ($300\,ps$). Since this is in the order of the time-resolution itself, it certainly has to be corrected[24].

The radial time correction can be calculated as

$$\Delta t_{start} = (r_{max} - r_{\vartheta})/c_{start}, \tag{4.8}$$

where r_{max}, r_{ϑ} are the maximum and particle radii in the Start-detector, respectively, and c_{start} is the speed of light in the scintillator. During the Barrel calibration, c_{start} was found to be $12\,cm/ns$, which is considerably slower than $c_{vac}/n_{sci} \approx 19\,cm/ns$. This value seems nevertheless reasonable, since the effective pathlength is enlarged due to reflections of the light within the $1\,mm$ thick detector.

The value of c_{start} is stored in the `TofCal` file and the time correction is automatically applied when using the track-class `TofTrackParticle`.

---

[21] And also the momentum and the time-of-flight, since $p = p(\vartheta)$, $\texttt{tof} = \mathrm{tof}(\vartheta, \mathrm{geom}, \mathrm{m_p})$.

[22] Implemented by Leonhard Karsch [Kar04]

[23] The (small) "slice" histograms in Fig. 4.5 are horizontal cuts. The σ of the Gauss fit therefore has to be divided by $\sqrt{2}$.

[24] Particles hitting the Quirl/Ring-hodoscopes need no correction, because the transit time in the Torte is already taken account of during the stop pixel calibration.

4.5 The CAL Format

The last step of calibration/conversion - the track-search - is implemented in the program `caltemp2cal`. The use of tracks will allow easy access to all "physical information" and therefore permit to concentrate on the actual analysis.

The track search is a very CPU-time consuming process. Programs which calculate the tracks on-the-fly, always have to accept compromises between required CPU-time and track reconstruction efficiency/accuracy. This is not necessary in TofRoot. *All* possible permutations of *all* clusters in each of the three Erlangen-Start detectors are tested with a linear fit. Considering the exponential growth of possible permutations with the number of participating clusters, this surely is a very expensive approach. And in fact, the event rate drops to about 100 events/CPUs ($1\,GHz$ CPU). However, since in TofRoot the track search is executed only once, this approach is justified[25].

The "standard histograms" of a CAL-file can interactively be viewed using the macro `cal_anguck.C`. They allow a quick and comprehensive check of track quality and acceptance.

4.5.1 Converting CALtemp to CAL format: The Track Search

Using the Erlangen-Start in combination with the stop components (Quirl, Ring, Barrel) enables the ("real") tracking of charged particles. The track search is launched for each stop pixel[26] participating in an event, and the procedure applied is rather straightforward:

1. Each stop pixel is checked for a Torte hit within the "same" azimuthal range.
2. Candidates with velocities of $0.3<\beta<1.2$ are considered "physically possible".
3. The clusters of each Erlangen-Start-detector are combined to pixels.
4. The position (x,y,z) of each pixel in each Erlangen-Start detector is calculated.
5. All possible permutations of the pixels are subjected to a linear fit ($\rightarrow \chi^2$-value).
6. The χ^2-value is used as the criterion to define a "good" track.

If a track is found, the class `TofTrackParticle` is filled with the track information and added to the "track array" in `TofTracks` (see 3.2).

The requirement for a Torte-hit implies that all tracks in TofRoot are *primary tracks*; i.e. tracks emerging from the vicinity of the target, passing the Torte detector, and hitting the stop-detector without considerable change of direction[27]. If the β cut is passed, but no pixels in the Erlangen-Start are found, this track is called an *only-stop* track, and added to the track collection. This procedure is correct, since not every particle can generate a track: The tracking devices do not cover angles larger than 45° and the Erlangen-Start track-efficiency is smaller than 100%. If two or three pixels

---

[25] 8×10^6 events are processed within 24 CPUh.

[26] A Barrel hit is also considered a pixel in this context.

[27] Routines to search secondary tracks (decay products) are implemented by L. Karsch [Kar04] and G.Y. Sun and soon will be added into the official TofRoot framework.

are found within the Erlangen-Start, this track is called a "real-track" and added to the track collection. "One-pixel" tracks are not evaluated, because in this case the linear fit (only two points) always returns a χ^2 of zero. If more than one permutation passes the cutoff test, the track with more contributing pixels is chosen, and if equal numbers are found, then the track with the smaller χ^2-value is selected.

Twin Tracks

At the transition of Quirl/Ring and Ring/Barrel the stop detectors have a small physical overlap. Here, a particle in general generates *two* stop signals. In addition, cross talk, due to photon leakage or secondary reaction products, can trigger signals in neighboring stop channels. Since the track search is invoked for each stop pixel, and these pixels have similar angular and time information, the probability to find two almost identical tracks is high. These tracks are called *twin tracks*. The number of twin tracks is in the order of 6% of all tracks, and they can be a source of considerable error: For physical analysis often a cut requiring an exact number of tracks is applied (`if(gevTracks->GetTracksTotal()==4){...}`). If one of the reconstructed tracks is a twin track, this cut is not passed since *more* tracks are found. The examination of twin tracks using Monte-Carlo methods is difficult, since the basic processes (cross talk) are very hard to implement in a quantitatively correct way.

An interesting feature of the TofRoot track search is the *flagging* of these twin tracks. Each track "knows" if it has a twin, how many twins[28] are involved and where these twins are located in the track array. This procedure was chosen, since during the track search it is not possible to decide which of the twins is the "correct" track. Later, considering the whole reaction pattern, the user has the possibility to decide which of the twin tracks should be used for analysis. However, this approach often may be considered too expensive and too complex, since the track information of the twin tracks is rather similar. Therefore, a very convenient and simple way to loop over "twin-purified" data is implemented:

```
Int_t poscarry[20];
Int_t nof = gevTracks->CalcPositionList(&poscarry[0]);
for(i=0;i<nof;i++){
    TofTrackParticle *evTP = gevTracks->GetTrack(poscarry[i]);
    // ... analysis ...
}
```

Here, the positions of all single tracks and the *best* twin tracks are stored in the array `poscarry`, where the best twin is chosen according to the number of pixels found in the Erlangen-Start and the χ^2-value.

4.5.2 Calibration Routines Reading CAL format

A "complete calibration of a detector system" can be defined as complete conversion *and complete calibration*. Therefore, it is not a contradiction to use the CAL format

---

[28] Triplets, quadruplets, ... are all named "twins".

Task	**Author**[a]
dE/dx-measurement in the Quirl-, Barrel-, and Torte-detector.	cp,lk,wu,msw
Cluster-analysis in the calorimeter.	wu,rj
Particle ID, using the "dE/dx vs. E" method.	lk,wu,rj
Neutron detection in the calorimeter.	wu,rj
Fitting of more than two tracks to a common origin.	gys,msw
Generic method for a kinematic fit.	lk
3d - visualization of the detector and the reaction pattern (tracks).	wu,msw
Online and offline determination of the beam-polarization	wu,msw

---

[a] rj=R.Jäkel, lk=L.Karsch[Kar04], cp=C. Plettner, msw=M.Schulte-Wissermann, gys=G.Y.Sun, wu=W.Ullrich

Table 4.3: *Further developments for TofRoot. The involved authors are listed in the second column.*

as input for further calibration (even though the name may indicate the contrary)[29]. So far one calibration routine exists, but further developments are under construction (see next section).

dE/dx Measurement in the Microstripdetector

The QDC-conversion of a microstrip detector is directly proportional to the amount of ionization caused by the particle; and the amount of ionization is directly proportional to the *energy deposition*. Since, according to the Bethe-Bloch formula, the energy deposition is proportional to $1/\beta^2$, the QDC-value of the Microstrip directly measures the velocity of the particle.

The calibration of the Microstrip for dE/dx-measurement was implemented by L. Karsch [Kar04]. The β-resolution is ≈ 0.1 (FWHM), which at high particle velocity ($\beta > 0.85$) is comparable to the resolution obtained using the time-of-flight. The main disadvantage of this method is its acceptance: It is only about 90% in the acceptance range $5^\circ < \vartheta < 45^\circ$ and zero for all other polar angles. This limited its use for this work, but could be of interest for other data analysis. Especially in combination with dE/dx-measurement in the Quirl/Torte detectors and the energy measurement of the newly installed calorimeter, it will be possible to perform direct particle ID using the "$dE/dx\, vs.\, E$"-method.

4.5.3 Outlook

The calibration of the TOF-detector using the TofRoot-routines and the data conversion up to the CAL format enables direct access to the physical observables. According to the aims defined in 2.2.2 (see also Tab. 2.2), the calibration of the COSY-TOF detector can be considered to be complete. In many cases the calibration is of higher

---

[29] Of course, it is tempting to skip calibration reading the CAL format, since the provided functionality is already high - but is is not at all advisory!

precision compared to any previously used analysis framework. Some calibration features are completely new.

However, since the (hardware) development of the TOF-detector is not completed and there is always a desire for improvement, additional calibration routines will be implemented in the future. The tasks presently under construction are listed in Tab. 4.3, some of the new developments will be described in [Kar04] and [Ull04].

Part II

Meson Production in Proton-Proton Collisions

Chapter 5

Elastic Scattering

5.1 Introduction

Elastic scattering is the most elementary process in proton-proton interactions. Although considered a “simple” reaction, elastic scattering is of substantial interest. The forces involved are of *nucleonic* origin, where the theoretical description is nested within the typical models of each energy region: Meson exchange (potential) models provide a satisfactory description of elastic scattering below the pion threshold. Beyond the pion threshold, inelastic channels have to be included into the theoretical description, and above $T_p \approx 1\,\mathrm{GeV}$ the probed distance between the nucleons can be small enough ($d_{pp} < 0.8 fm$) for the hadron structure of the nucleon to come into play. Here heavy mesons exchange and/or the quark-gluon interactions are responsible for the presence of a strong repulsive force. Since elastic scattering continuously traverses all energy regions, the (overall) theoretical description should also migrate continuously from one model region to the other. This is presently under debate [Mac01].

Elastic scattering has been extensively measured in the past at beam momenta below 1020 MeV/c (IUCF, [Rat98]) and above 2570 MeV/c (SATURNE, [All99]), rendering an enormous amount of data covering differential cross sections, excitation functions, spin correlation parameters, partial wave amplitudes, and analyzing powers. Using this data set as input, phase-shift analyzes ([Arn97],[Bys98]) achieve remarkable results in describing the physical observables in the measured energy region, but their predictive power is limited.

Recently, the EDDA collaboration (located at COSY) closed the experimental lack of knowledge at intermediate beam momenta ($800-3300$ MeV/c) [Sco01][Alt00]. EDDA utilizes a detector which is especially designed for the measurement of elastic scattering (high solid-angle coverage, good angular resolution, azimuthal symmetry). It measures the excitation functions (during the ramp phase of the accelerator) in small energy steps and with a high relative accuracy. Since EDDA is located at COSY, scanning the whole energy range up to the COSY-limit, it provides an ideal experimental database for luminosity determination to all other COSY experiments.

The TOF detector was not designed exclusively for (absolute) measurements of elastic proton-proton scattering. Quite the contrary, since TOF is an external experiment it *depends on* elastic scattering for luminosity determination[1]. It should not at all be claimed that TOF will provide fundamentally new experimental data regarding elastic scattering. However, the angular resolution of the TOF detector is comparable to the resolution of EDDA, and utilizing the time-of-flight information as additional input, a practically background-free signal is obtained. From this, differential cross sections can be extracted. Therefore, in the case of a specific question (e.g. evidence for a di-baryonic resonance), and in conjuction with an improved beam monitor, TOF could, by all means, quickly provide supplementary data.

For the rest of this chapter, the following two aspects shall be examined in detail:

1. The event-selection procedure for two-prong events using the angular and time-of-flight information will be described. All available information will be used as input to a *likelihood fit*. This will yield a χ^2-value, which is used to discriminate elastically scattered events from background. The angular distribution of the protons in the CMS is then compared to the result of EDDA. This allows to determine the (relative) integral luminosity $\tilde{\mathcal{L}}$ with very small uncertainty of better than 3%. This is of paramount importance for the subsequent analysis of other reaction channels ($pp \rightarrow d\pi^+, pp \rightarrow pp\omega$). After the luminosity is fixed, differential cross sections ($d\sigma/d\cos(\vartheta) \rightarrow$ Legendre fit parameters) for both energies will be given.

2. The performance of the TOF detector and the quality of the calibration will be demonstrated using elastic scattering as an example.

5.2 Data Analysis

In a typical TOF experiment, the main trigger settings focus on enhancing complex reactions (e.g. $pp \rightarrow pK^+\Lambda$) which usually have cross sections at least two orders of magnitude below the elastic scattering. For luminosity determination, elastic events are selected in parallel using an *elastics trigger* where in general only two entries in the Torte are required[2]. This trigger pattern is usually scaled down with respect to the main trigger by a factor of 2^8.

During off-line analysis, kinematic constraints are used to further select true $pp \rightarrow pp$ events. In principle, cuts on two observables calculated from the measured *directions* allow a clear enhancement of elastic-scattering events:

$$\gamma^2_{CM} = \frac{1}{tan(\vartheta_1)\cdot tan(\vartheta_2)} \approx \overline{\gamma}^2_{CM} \tag{5.1}$$

$$\Delta\varphi = \varphi_1 - \varphi_2 \approx 180^\circ, \tag{5.2}$$

where $\gamma_{CM}, \overline{\gamma}_{CM}$ are the measured and "exact" Lorentz factors of the CMS in the laboratory frame; and $\vartheta_{1,2}, \varphi_{1,2}$ are the measured polar and azimuthal angles in the

---

[1] The luminosity could in principle be determined by other means (e.g. $pp \rightarrow d\pi^+$, beam counting). However, these methods are not competitive considering the experimental uncertainty. An improved beam-monitor could free the TOF of the necessity to use elastic scattering for luminosity determination.

[2] Using a MLU (**M**emory **L**ookup **U**nit), the coplanarity of (two) hits in the start detector may be used as a first selection criterion.

laboratory frame, respectively.

This is the method used in the past at TOF and also by the EDDA collaboration. It results in a very clean signal, which, nevertheless, always resides upon a non reducible background. This has three main reasons:

- Using the ϑ/φ-information separately (Eq. 5.1, 5.2) has the disadvantage that their mutual dependence is neglected.
- The significance of the coplanarity $\Delta\varphi$ decreases as the tracks come close to the beam axis[3].
- Combinatorial background accidentally resulting in "quasi-elastic" angles is inevitable.

Therefore, a new analysis method has been developed where the angle information is treated in an improved manner. In addition, the time-of-flight information is used to considerably improve the event selection. It is important to mention that this new analysis method is applicable for *any* kind of two-prong event, and it will also be used to discriminate the reaction $pp \rightarrow d\pi^+$ (see Chapter 6).

5.2.1 Event Selection: Two-Prong Events

The start region the TOF detector is equipped with tracking devices (Microstrip, small/big hodoscope), which, together with the track-finding routines of TofRoot, allow very good track reconstruction. Having tracks ($\vec{r}_0 + \lambda \cdot \vec{r}$) rather than only the directions allows an additional vertex fit: Using the point-of-closest-approach as additional information, both tracks are successively re-fitted until they have a common origin. This procedure results in high-quality angular resolution, which is needed for the following steps.

Figure 5.1 shows a schematic picture of the kinematic situation for *any* two-prong event. Using a mass-hypothesis, momentum conservation relates the momenta of both prongs to the incident momentum and the two measured polar angles ($\vartheta_{1,2}$) by simple algebra. Thus, the measurement of these two angles alone allows to *calculate* the momenta of the involved particles. Assigning the masses (mass hypothesis) of the particles to the momentum vectors we obtain the four-momentum vectors. These four-momenta now can be transformed into the CMS. Here, a true two-prong event has to be back-to-back, i.e. with a collinearity $\Delta\vartheta^*$ of

$$\Delta\vartheta^* = \sphericalangle(\vec{p}_1, \vec{p}_1) \simeq 180°, \tag{5.3}$$

where $\vec{p}_{1,2}$ are the momentum vectors in the CMS. It should be emphasized that using $\Delta\vartheta^*$ as a discriminating observable already leads to a comparatively cleaner picture than both Eq. 5.1 and 5.2 separately.

---

[3] (Dramatic) example: a $\Delta\vartheta = -2°$ deviation of a track with $(\vartheta, \varphi) = (1°, +180°)$ results in a new direction $(\vartheta, \varphi) = (1°, -180°)$.

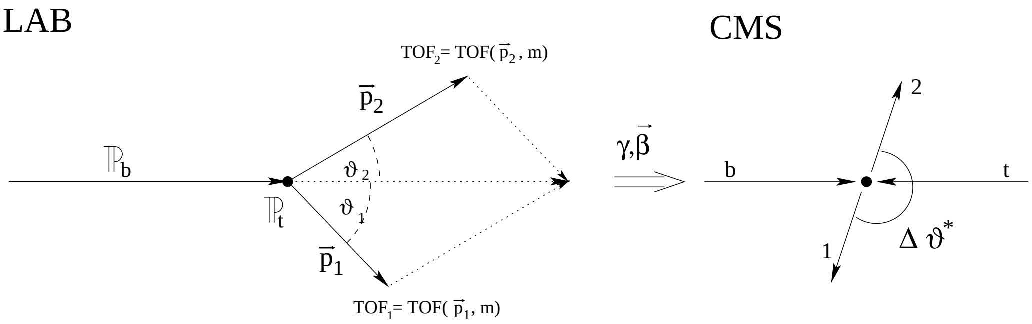

Figure 5.1: *In any two-body reaction, the measured angles and the initial beam momentum allow the calculation of the momenta of the two ejectiles in the lab system. Using a mass hypothesis the four-momenta can be assigned. From this, and using the detector geometry, the* expected *time-of-flight can be calculated. In addition, the four-momenta can be boosted into the CMS. Here, a true two-body reaction must be collinear.*

Utilizing the Time-of-Flight Information

In contrast to EDDA, the TOF detector also measures the time-of-flight of particles. Unfortunately, at the high beam momenta used (2950 and 3200 MeV/c), the involved velocities of elastically scattered protons are so close to the speed of light that it is not possible to calculate the particle momenta with reasonable resolution. This has two main reasons: (1) at $\beta \approx 0.95$ the time-of-flight (t_{tof}) is so small that the relative time-of-flight uncertainty is very large ($\sigma_{t_{tof}}/t_{tof} \approx 0.3\,ns/10\,ns$); and (2) the calculation of the momentum diverges as β gets close to the speed of light[4]. This is illustrated in Fig. 5.2, where the kinematic ellipse of the elastic protons is shown. While momentum resolution from the time-of-flight measurement clearly is inadequate (upper frame), the calculated momenta from the measured polar angles agree very well with the kinematical expectation (lower frame).

The diminishing momentum resolution from the time-of-flight measurement prohibits its use for "classical" missing mass analysis. It is impossible, for instance, to separate the elastic channel from $pp \rightarrow pp\pi^0$. However, the time-of-flight information can be utilized very advantageously through a different approach: Including the detector geometry, the *expected* time-of-flight can be *calculated* from the assigned four-momenta. This then is compared to the *actually measured* time-of-flight, which yields the observable

$$\Delta TOF_{1,2} = TOF_{1,2_{measured}} - TOF_{1,2_{calculated}} \tag{5.4}$$

for both particles.

The three observables ($2 \times \Delta TOF$ and $\Delta\vartheta^*$) are then the main ingredients to a χ^2-test. Additional input to the fit, although not that significant, is the deviation from the expected invariant mass and the difference between β calculated by time-of-flight and via dE/dx-measurement in the Microstrip. The fit is performed using the functionality of the ROOT class `TPrincipal`, which automatically ensures an orthonormal pattern-space of all physical observables. Figure 5.3 shows the distribution

---

[4] $\lim_{\beta\rightarrow 1} p = m\gamma v = m\sqrt{\frac{1}{1-\beta^2}}\,v = \infty$.

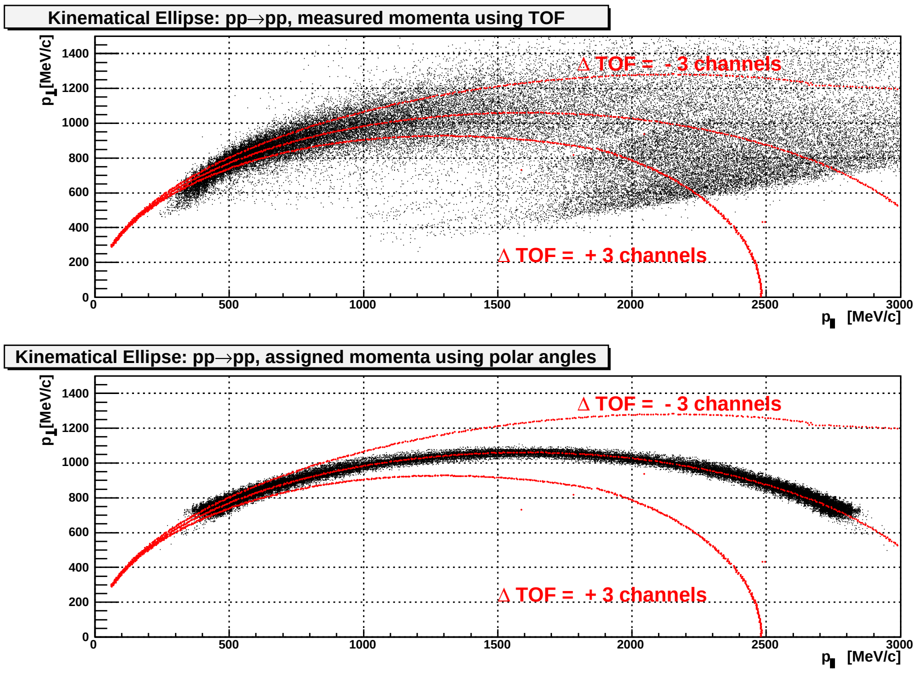

Figure 5.2: *In the upper picture, the longitudinal and transverse momenta, as calculated with the* time-of-flight *measurement, is shown. The red lines correspond to a deviation of* $0, \pm 3$ *channels from an ideal time-of-flight measurement, respectively. This corresponds to* $\approx \pm 1\sigma$ *of the experimental time-resolution. At these high beam momenta (*3200 MeV/c*) the time-of-flight resolution is NOT sufficient to calculate the momenta of particles within reasonable limits. Below, the situation for* calculated *momenta using the polar angles of the particle is shown.*

of χ^2 for experimental data. A peak at small χ^2 values is visible which clearly is separated from background. The entries of this peak correspond to elastically scattered events.

5.2.2 Monte-Carlo : Background and Acceptance Correction

The primary motivation for examining the elastic scattering is the need to determine the (integral) luminosity. An uncertainty of the luminosity will directly add to the experimental uncertainty of any subsequently deduced total cross section. Therefore the background contribution as well as the detector/software deficits have to be analyzed quantitatively. Both tasks are in general solved by the use of Monte-Carlo simulation, which in case of TofRoot, is the Monte-Carlo solution LasVegas (see. 2.2.5).

Background

At the experiment, the trigger setting to select elastic scattering usually demands *two* entries in the Torte. This certainly is a very weak requirement and is fulfilled by many reactions. Besides $pp \rightarrow pp$, especially $pp \rightarrow pn\pi^+$, $pp \rightarrow pp\pi^0$ and $pp \rightarrow d\pi^+$ all have only two charged particles in the exit channel. To quantitatively examine their contri-

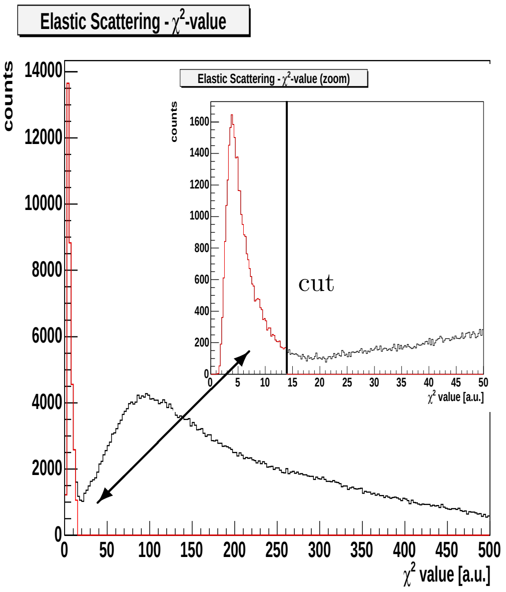

Figure 5.3: *The χ^2 distribution of experiment data shows a prominent peak at small values. The smaller histogram shows a zoom into the region below $\chi^2 = 50$, where also the cut at $\chi^2 = 14$ is shown. The agreement with the Monte-Carlo result (Fig. 5.4) is rather well and gives confidence in the method used.*

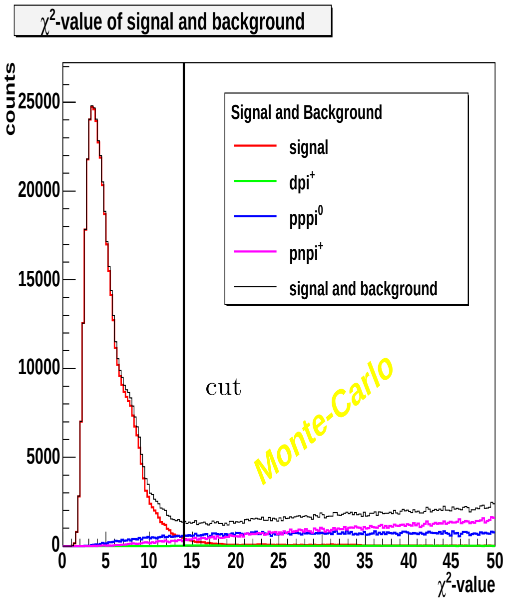

Figure 5.4: *Monte-Carlo simulation of signal and background reactions. The background reactions ($pp \to pn\pi^+$, $pp \to pp\pi^0$, $pp \to d\pi^+$) enter the analysis with realistic cross sections ratios (1 to 4 : 1 : 0.01). A quantitative analysis yields the overall background contribution to be below 6%.*

bution to the "elastic signal", all these reactions were simulated by means of LasVegas. The background reactions enter the analysis with realistic total cross sections with respect to the elastic channel. The result of such an analysis is presented in Fig. 5.4, where the χ^2-distribution of $pp \to pp$ shows the same prominent peak as experimental data (Fig. 5.3). The main background reactions are visible in the same picture. All show only a few entries at small χ^2-values. A quantitative analysis yields the overall background contamination to be 5.0% (5.5%) at 2950 MeV/c (3200 MeV/c).

Acceptance Correction

The ratio of positively identified to initially produced events is called the *acceptance of detector and analysis*, or simply acceptance[5]. It accounts for the *geometrical acceptance* (solid angle coverage), the *detector efficiency* (detected/incident particles) and the *software efficiency* (reconstructed/offered events). Observables depending on the measurement of a "count rate" in general have to be acceptance corrected.

The acceptance of all reactions considered in this work is determined by means of Monte-Carlo simulations: A known number of events is generated, propagated through the (virtual) detector, and the output is analyzed with the very same software as ex-

---

[5] To emphasize the difference to the *geometrical acceptance*, some authors may also use the word *effectivity* or *efficiency*.

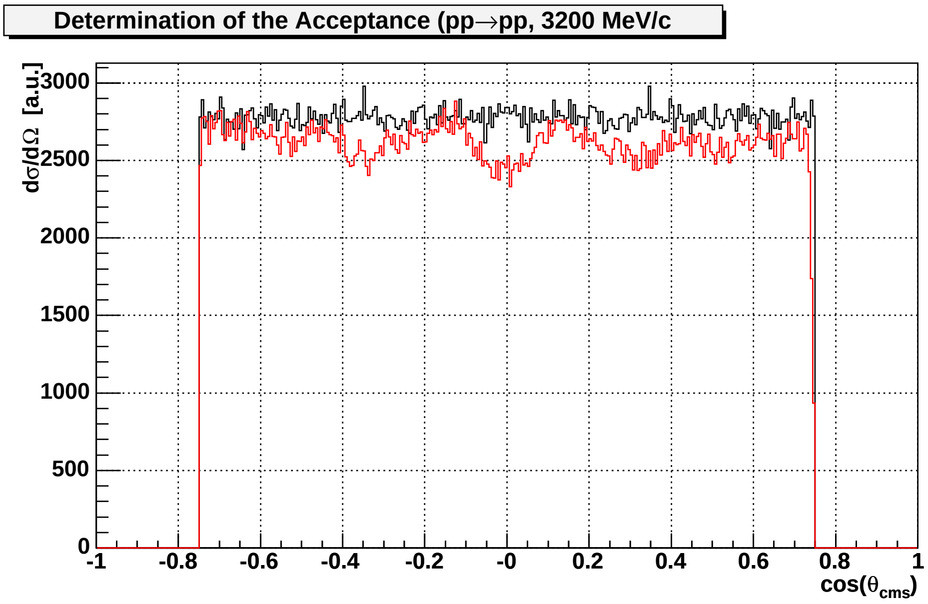

Figure 5.5: *Monte-Carlo methods are used to determine the acceptance for elastic scattering at* 3200 MeV/c *(analogous behavior for* 2950 MeV/c*). The distribution of the protons (CMS) for cos(*ϑ*) as created by the event-generator is plotted in black. The reconstructed events, using the very same analysis as for experimental data, are plotted in red. Dividing both histograms yields a correction factor for each bin. The "dips" at* $\cos(\vartheta_{CM}) \approx 0$ *and* $\cos(\vartheta_{CM}) \approx \pm 0.3$ *are well understood (see text).*

perimental detector data. To determine the ratio of generated and detected events, each observable of interest is filled into two histograms:

- **The "input" data**: The information of all *original* Monte-Carlo events, i.e. as it was initially produced by the event generator.
- **The "analysis" data**: The information of the *reconstructed* Monte-Carlo event, i.e. including all effects such as data loss due to geometric acceptance and software cuts, physical smearing, track-reconstruction uncertainties, and analysis (in)efficiencies.

The acceptance is then determined from the ratio of both histograms, which yields a correction factor for each bin. "Detector data" can now be acceptance-corrected by simply applying this factor to the measured bin-content.

Fig. 5.5 illustrates this procedure for the Monte-Carlo distribution ($\cos(\vartheta_{CMS})$) of the protons in the CMS. The original $\cos(\vartheta)$ distribution, as produced by the event generator, is isotropic (black)[6]. The reconstructed events are plotted into the same histogram (red). Within the (geometrical) acceptance range of $|\cos(\vartheta)|<0.7$, the average acceptance is 94.4% (94.1%) for 2950 MeV/c (3200 MeV/c). Apart from the

---

[6] The quantity of interest is the *ratio* of detected to offered events *per bin*. In case of a "two-body" exit channel this ratio is independent of the physical angular distribution. Hence, using an isotropic "input-distribution" is sufficient.

three "dips", the distribution of the reconstructed events is rather smooth over the whole acceptable angular range. The dip at $\cos(\vartheta) \approx 0$ is caused by "symmetric" events, where both particles emerge at similar polar angles ($\vartheta_1 \simeq \vartheta_2$). In this case, both particles hit the same (or closely neighboring) ring of the Microstrip detector. This leads to a "broadening" of the cluster, which deteriorates the quality of the pixel information. Since the pixel quality directly influences the track quality, these events have a higher possibility of not passing the χ^2 test.

The dips at $\cos(\vartheta) \approx \pm 0.3$ are caused by two different effects, which influence both protons simultaneously. At $\cos(\vartheta) \approx +0.3$ ($\vartheta_{lab} \approx 25°$), a particle can hit the light-guide of the Barrel photomultipliers, causing Cherenkov light that adds to the signal. At $\cos(\vartheta) \approx -0.3$ ($\vartheta_{lab} \approx 45°$) the angular acceptance of the fiber hodoscopes ends. The particles do not create pixel-information aiding the track reconstruction, but still have to pass the light guides or the mounting material. Both effects reduce the track quality, thus enlarge the possibility that such an event does not pass the χ^2-test.

5.2.3 Angular Distribution

The angular distributions of the protons in the CMS is shown for both incident beam momenta (2950 and 3200 MeV/c) in Fig. 5.6 (blue). The error bars reflect the statistical errors only. The events were selected according to their χ^2-value as seen in Fig. 5.3. The cut-value of $\chi^2 = 14$ was optimized by Monte-Carlo, to have approximately the same percentage of background contamination as data loss due to acceptance inefficiencies. The contribution of background was determined to be less than 6% for both energies (see Fig. 5.4). Since the angular distribution of the background is rather smooth, each bin is corrected with a fixed background contribution. The acceptance correction has been applied bin-per-bin using Monte-Carlo data, as described previously. The geometrical acceptance is limited to $|\cos(\vartheta_{CMS})| \lesssim 0.7$, since in the January 2000 beamtime, the setup of the TOF detector permitted only polar angles in the laboratory frame of $\vartheta_{lab} \lesssim 60°$.

The measured angular distribution is scaled to data published by the EDDA-collaboration at virtually the same beam momenta ($\Delta p_{beam} < 2 MeV/c$). The EDDA data is plotted into the same picture (red) as well as a fit using the first four even Legendre polynomials[7]. The numerical values of these fits are listed in Tab. 5.1. The agreement of TOF and EDDA is perfect within uncertainty limits. However, compared to EDDA, the TOF data has a smaller binning and smaller statistical uncertainties, hence a higher statistical significance. This is, of course, because EDDA measures *many* incident energies during the ramp-phase of the accelerator. If EDDA would exclusively measure one beam momentum, the statistical basis would also improve. However, the smallest possible bin-size is determined by the angular resolution of a detector, and the binning of the TOF measurement already reflects the resolution of the TOF detector. Since the angular resolution of EDDA is not superior to TOF (see Tab. 5.3), the binning of EDDA will also not surpass the binning of TOF.

A detailed look at Fig. 5.6 shows that the TOF data were *not* symmetrized. This was done to emphasize that the TOF detector independently measures the angles in the forward and backward hemisphere (CMS), but with slightly different angular

---

[7] Since the entrance channel is symmetric, only even polynomials contribute.

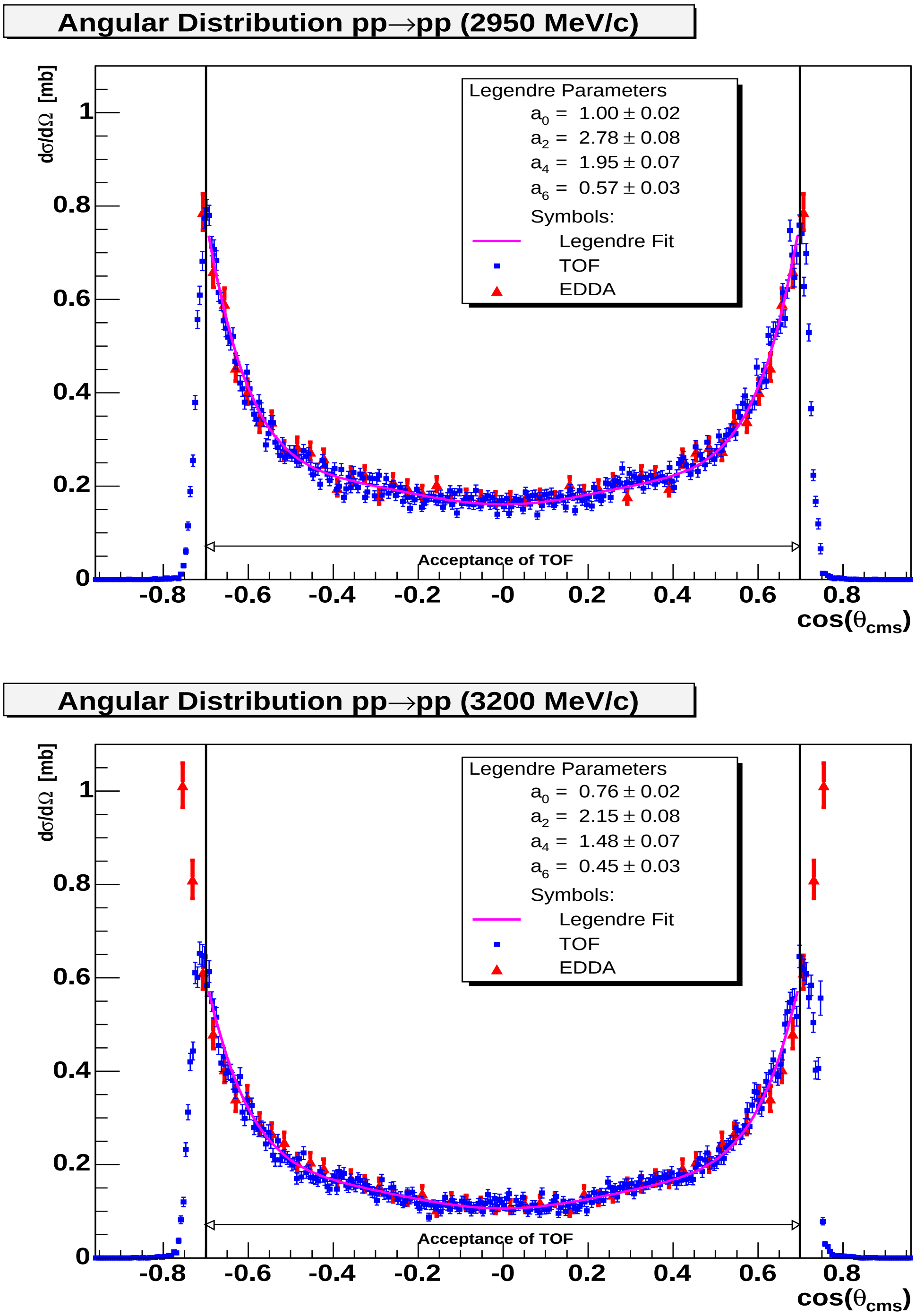

Figure 5.6: *Angular distribution of elastically scattered protons in the CMS. The data measured with the TOF detector (blue) is scaled to the results of EDDA (red, [Alb97]). The acceptance limits of the TOF detector are shown as vertical lines. The full line through the data (magenta) represents a Legendre fit using the first four even Legendre terms.*

resolutions: At $\cos(\vartheta) \gtrsim 0.3$ an intended (software) smearing of "only-stop tracks[8]" hitting the Ring had to be applied. Otherwise, the pixel structure of the ring detector would lead to discrete spikes in the spectrum. The polar angle information of the Barrel detector ($\cos(\vartheta) \lesssim 0.3$) always is continuous and smearing is not necessary. Therefore, a peculiar (narrow) structure could be observed only in one hemisphere, although it must be present in both, since the exit channel is symmetric. A detailed inspection of the measured angular distribution does not show any deviation of the smooth slope described by the Legendre fit. Even so, the human eye may "want" to see a correlation of the EDDA and the TOF data at $\cos(\vartheta) \leq -0.3$ ($2950\,MeV/c$) and $|\cos(\vartheta)| = 0.2$ ($3200\,MeV/c$). In the publication [EDD97b], EDDA claims that "minor structures" are visible which are caused by detector effects[9]. If they were reproduced by TOF, this (at least) would be surprising. If present at all, these "structures" most probably originate from the comparable design of both detectors or from a slight admixture of background, i.e. from a similar error during the acceptance correction or a similar misapplication of the background subtraction. If both can be excluded, a (so far unknown) physical effect could be responsible. At present, this is highly speculative. However, for future beamtimes of the TOF detector, it is planned to set the suppression factor for two-prong events to a smaller value. Hence, a higher statistical basis for $pp \to pp$ will be available, hopefully clarifying this issue.

Legendre Coefficients	$p_{beam} = 2950\,\mathrm{MeV}/c$	$p_{beam} = 3200\,\mathrm{MeV}/c$
a_0	1.00 ± 0.02	0.76 ± 0.02
a_2	2.78 ± 0.08	2.15 ± 0.08
a_4	1.95 ± 0.07	1.48 ± 0.07
a_6	0.57 ± 0.03	0.45 ± 0.03

Table 5.1: *Legendre coefficients of the angular distribution of elastic scattering ($\mu b/sr$).*

5.2.4 Luminosity Determination

The main intention of the (quantitative) examination of the elastic scattering is to determine the luminosity $\tilde{\mathcal{L}}$. This problem is equivalent to finding the scaling factor ℓ needed to adjust the TOF angular distribution to the data of EDDA.

$$d\sigma_{EDDA}/d\cos\vartheta = \ell \cdot d\sigma_{TOF}/d\cos\vartheta \qquad (5.5)$$

This scaling factor was found by fitting both distributions with a polynomial, then minimizing the quadratic error of both fit-functions

$$\chi^2 = \sum_{x=-0.7}^{x=-0.7} (f_{EDDA}(x_i) - \ell \cdot g_{TOF}(x_i))^2, i \in [0, 300]. \qquad (5.6)$$

---

[8] "Tracks", which do not have fit-points in the Erlangen-Start.

[9] Quotation EDDA [EDD97b]: "The data contained in this distribution when viewed as a whole shows some minor structures due to deficiencies in angular reconstruction. These structures are traced back to fixed laboratory scattering angles and are known detector artefacts to be removed in the refined analysis."

This yields a scaling value with a numerical error of less than 1 ‰ and a systematic uncertainty of $< 0.3\,\%$. The influence of the different incident beam momenta in the TOF and EDDA measurements ($\Delta p_{beam} < 2 MeV/c$ for both beam momenta) can be neglected. As shown in Fig. 5.4, a small background is still present in the measured elastic sample. Monte-Carlo studies determine the background contribution to be $5.0 \pm 1\%$ ($5.5 \pm 1\%$) for 2950 MeV/c ($3200 MeV/c$).

The systematic error of $\tilde{\mathcal{L}}$ is dominated by the uncertainty of the acceptance correction, which is in the order of $\pm 2\%$. The total systematic uncertainty for the luminosity can then be calculated to $\sigma_{lum} = \sqrt{\sigma_\ell + \sigma_{bg} + \sigma_{acc}} = \sqrt{0.3^2 + 1.0^2 + 2.0^2}\,\% = 2.3\%$. Compared to this value, the statistical uncertainty ($n_{pp} > 25000 \;\rightarrow\; 1/\sqrt{n} \approx 0.5\%$) is small so that both uncertainties (statistical and systematical) add up to a total uncertainty of the TOF measurement of 2.4%. This is smaller than the total uncertainty of the EDDA measurement, which is quoted to be $< 2.9\%$. However, since the TOF measurement is scaled to the "known" EDDA distribution, the uncertainty of the EDDA measurement has to be added to the experimental uncertainty; and combining the TOF and the EDDA uncertainties in quadrature finally yields a value of 3.8 % for the total uncertainty of the luminosity determination. This value is a very conservative estimation and is valid for both beam momenta. The (relative[10]) integrated luminosity is listed in the table below.

Reaction	scale	$p_{beam} = 2950\,\mathrm{MeV}/c$	σ	$p_{beam} = 3200\,\mathrm{MeV}/c$	σ
$pp \rightarrow d\pi^+$	1	45.2 μb^{-1}	1.72	33.2 μb^{-1}	1.26
$pp \rightarrow pp\omega$	32	779.6 μb^{-1}	29.6	772.8 μb^{-1}	29.3

Table 5.2: *The (relative) integral luminosities for the January-2000 beamtime and for different reaction channels. The reaction $pp \rightarrow d\pi^+$ is analyzed using the same trigger pattern and the same data as elastic scattering. This also includes* calibration-runs*, where the aim is to enhance two-prong events. The reaction $pp \rightarrow pp\omega$ is studied only in "data-runs", but the trigger setting favors this reaction type by a factor of 32 with respect to elastic scattering.*

5.3 Performance of the TOF Detector

In this section, benchmarks for angular, time-of-flight and vertex resolution will be quantitatively examined using the elastic scattering as demonstrative example.

As described in 4.5.1 three types of tracks exist within the TofRoot framework. They can be discriminated by the number of participating pixels found in the three sub-detectors[11] of the Erlangen-Start detector: A track having three (two) pixels in the Erlangen-Start is named '3'-track ('2'-track); since in this case a "real" linear fit is performed these tracks are also called "real-tracks"; a track providing only the stop-

---

[10] Relative to the relevant trigger pattern, which has different pre-scaler settings for $pp \rightarrow d\pi^+$ and $pp \rightarrow pp\omega$.

[11] The Erlangen-Start has four sub-detectors (see Fig. 4.2), but only the Microstrip, the Small- and the Big-hodoscope provide pixel information.

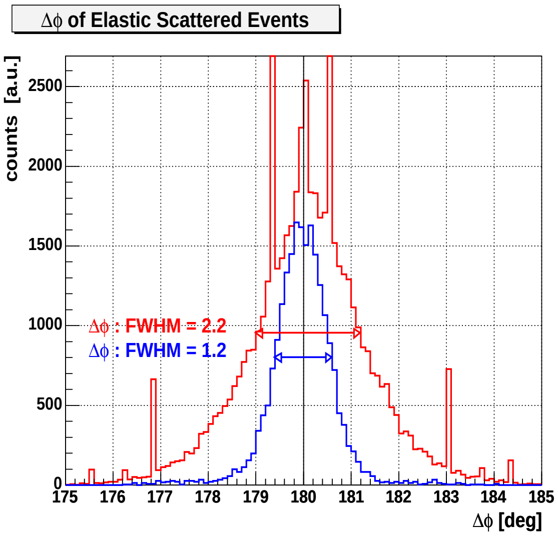

Figure 5.7: *Using elastically scattered events, the azimuthal angular resolution can be determined from the variation between the "ideal" relative angle of both tracks (red: all events; blue: only '3':'3' events). The* ideal *value is* 180°, *but due to small angle scattering and the detector granularity, the* measured *values are distributed around the central value. The spikes are due to the discrete φ-values of tracks not possessing fit-points in the Erlangen-Start. Quantitative results are given in Tab. 5.3.*

pixel information is called a '0'-track (or "only-stop")[12]. In general, the resolution of the tracks improves with the increasing number of participating pixels. Since the elements of the Erlangen-Start only cover polar angles up to $\approx 45°$ and the real-track efficiency at smaller angles is $\approx 85\%$, a mixture of all three track-modes is always present in the data.

Depending on the observed reaction (e.g. $pp \rightarrow pK^+\Lambda^0$), it may be required to demand only real-tracks (or even only '3'-tracks). This improves the track resolution, but at the (expensive) cost of count rate, overall acceptance, and acceptance uncertainties. For this work, all three possible track modes were always considered in order to exploit the advantage of the (almost) 4π-acceptance of the TOF detector. Therefore, the following discussion will focus on the achievable resolutions when "all track" modes are present in the data sample used. To show the possible resolution attainable allowing only '3'-tracks, events where *both* tracks have to be '3'-tracks will be presented as well. This type of event is then called '3':'3' event.

Angular Resolution

The *azimuthal* angular resolution can be obtained as shown in Fig. 5.7, where the deviation from the ideal coplanarity ($180° \simeq \Delta\varphi = (\varphi_1 - \varphi_2)$) is plotted. The histogram yields a FWHM of 2.2° for "all track" combinations (red). In addition, the result for '3':'3' events is shown (scaled, blue, FWHM = 1.2°). Since there are two independent measurements involved (two tracks with independent $\varphi_{1,2}$), simple error propagation then yields the following:

$$\sigma_{measured} = \sqrt{{\sigma_1}^2 + {\sigma_2}^2} = \sqrt{2 \cdot {\sigma_{1,2}}^2} = \sqrt{2} \cdot \sigma_{1,2} \tag{5.7}$$

$$\sigma_{1,2} = \frac{\sigma_{measured}}{\sqrt{2}} \quad . \tag{5.8}$$

---

[12] Tracks with only one pixel in the Erlangen-Start are not considered, since a linear fit using only two points (Erlangen-Start and stop) is always possible with a $\chi^2 = 0$.

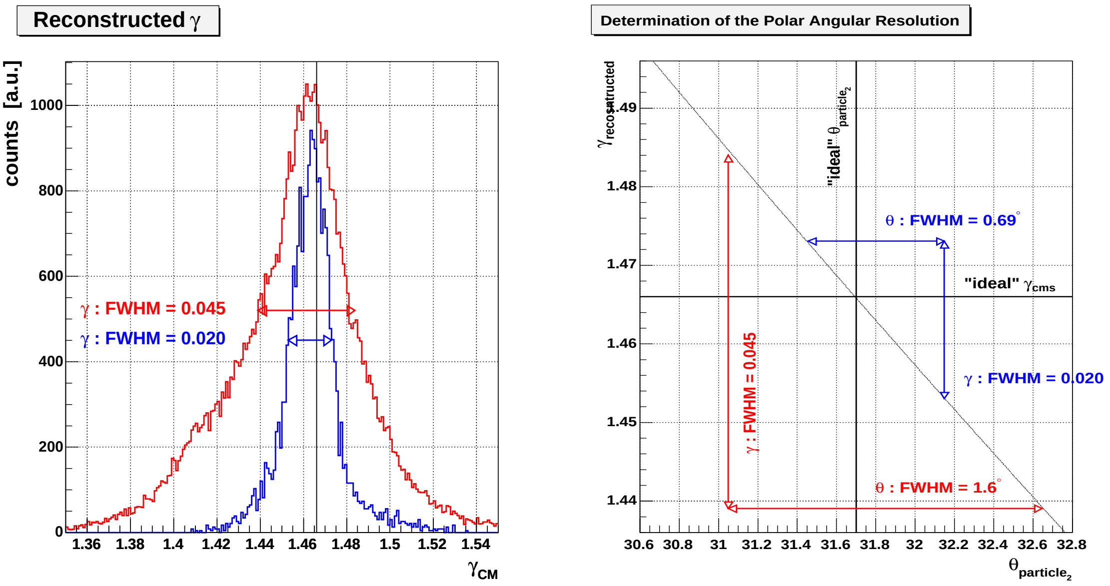

Figure 5.8: *The polar angle resolution can be determined from the reconstructed CM Lorentz factor (γ_{CMS}, Eq. 5.1). The value of γ_{CMS} is plotted in the left frame (all-events: red, '3':'3'-events: blue). The right frame shows how this translates into angular resolution (see text).*

where $\sigma_{1,2}$ is the angular resolution of a (single) track. The distribution shown here is fairly Gaussian, so that Eq. 5.8 is applicable also for the FWHM values, thus yielding an azimuthal resolution of 1.56° (0.85°) for all-tracks ('3'-tracks).

The determination of the *polar* angle resolution is more difficult, and it is performed using an intermediate step. Figure 5.8 shows the reconstructed center-of-mass Lorentz factor (γ_{CM}) on the left, which easily can be calculated using Eq. 5.1. The figure on the right shows how this translates into an angular resolution of the polar angle if one track would have an *ideal* value and the *other* track would be the only source of experimental uncertainty. An uncertainty of $FWHM = 1.60°$ (all events) and 0.69° ('3':'3'-events) is obtained. Since, in experimental data, this is the *combined* uncertainty of two independent measurements, division by $\sqrt{2}$ yields $FWHM_{all} = 1.13°$ and $FWHM_{'3'} = 0.48°$ as the experimental uncertainty for all-tracks and '3'-tracks, respectively. The results are summarized in Tab. 5.3.

<u>T</u>ime-<u>O</u>f-<u>F</u>light Resolution

The time-of-flight of a particle is the time difference between the Torte-detector and a stop component (Quirl, Ring, Barrel). Obviously, a good time-of-flight resolution is of crucial importance for the *<u>TOF</u>* detector. In this regard, the TOF-calibration was described in chapter 4 as a main pillar in the TofRoot-system.

The photomultipliers used at the experiment mainly are Hamamatsu R1450 [R1450] (start) and Phillips XP2020 [Phi94a][Phi94b] (stop). The (intrinsic) time resolution of the Torte detector is $FWHM \approx 400\,ps$ [Fri02], for the Ring $FWHM \approx 450\,ps$,

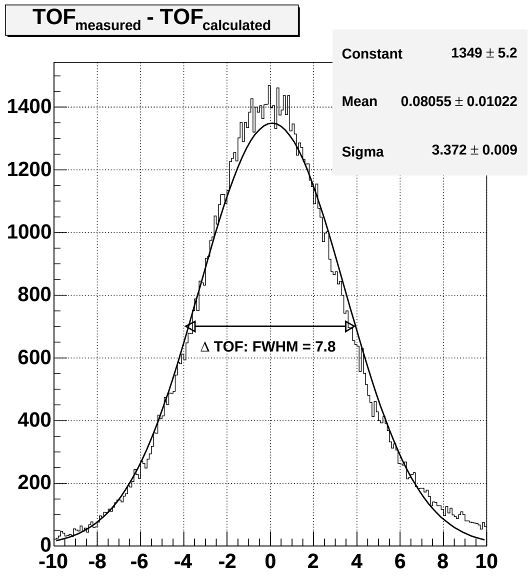

Figure 5.9: *The difference between the* measured *($tdc_{start} - tdc_{stop}$) and the* calculated *time-of-flight. The resolution $\sigma = 337\,ps$ ($FWHM = 780\,ps$) reflects the hardware resolution of the photomultipliers.*

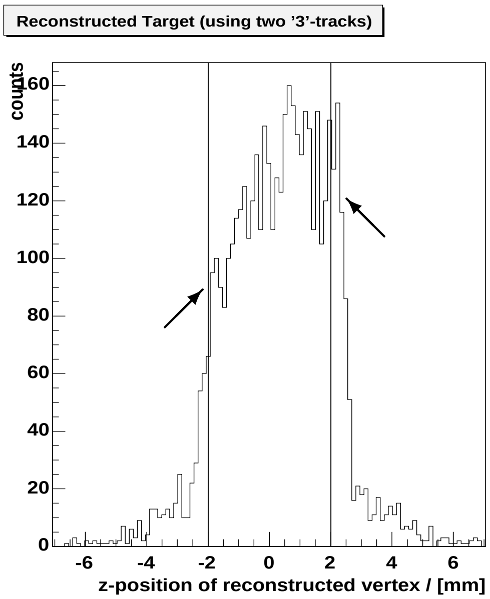

Figure 5.10: *Reconstructed z-position of the proton-proton vertex (only '3':'3' events). Along with the target position (lines at $\pm 2mm$), the target foils are also clearly visible (arrows).*

and $FWHM \approx 500\,ps$ for the Barrel. Measuring a time difference (TOF) requires two independent measurements, and therefore the *ideal* time-of-flight resolution is $\sqrt{400^2 + 500^2}\,ps \cong 640\,ps$. In Fig. 5.9, the deviation between calculated and measured time-of-flight, as used for selecting elastically scattered events, is shown. All track-modes in the full angular acceptance range were considered (including 24 start and 384 stop TDCs!). The figure renders a time-of-flight resolution of $780\,ps$ ($FWHM$). Considering that in Fig. 5.9 also the *angular resolution* is convoluted (the expected time-of-flight is calculated from an angle measurement), the measured time resolution can be considered to coincided with the “theoretically” possible value, which is simply given by the hardware resolution[13].

Vertex Reconstruction

The vertex (point of interaction of the protons) is calculated by successively re-fitting both tracks, until they emerge from a common origin. In this procedure, the point-

---

[13] A word of caution: The time-of-flight resolution in this case is of such outstanding quality because the calibration is based on elastic scattering! The detector is always hit with a *proton* having a *fixed velocity* for each solid angle. However, the TDCs show slight nonlinearities with time and signal height. As a result the TOF measurement can be *systematically* shifted (up to $\pm 300\,ps = 3$ channels) when detecting other particles (different energy deposit) with different velocities (different time-of-flight). This was accounted for in the analysis of $pp \rightarrow d\pi^+$, where the time-of-flight was manually adjusted by $\approx$ 1.5 channels.

of-closest-approach is used as an additional fitting point for both tracks (taking the distance-of-closest-approach as fitting error). Using only '3':'3' events results in a precise vertex reconstruction. First evidence was already shown in Fig. 1.3 in the introductory chapter where the x/y-distribution of the vertex is shown. It perfectly reflected the expected spatial distribution of the beam ("pencil-beam" with $\varnothing \cong 1mm$). Since no other means for the estimation of the beam distribution is available, only upper limits for the x/y-resolution can be given. An estimate of $\Delta x = \Delta y \leq 0.3\,mm$ seems reasonable. The situation is improved for the resolution along the beam axis (z). Here, the position of the target, and, in particular, the positions of the (extremely thin) target windows, are known. Figure 5.10 shows the distribution of the reconstructed z-value of the vertex. The target center is at $z = 0$ with an extension of $\pm\,2\,mm$ (lines). The positions of the target windows are clearly visible as narrow peaks, from which the vertex resolution along the z-axis can be estimated to be better than $\Delta z < 0.3\,mm$. The slight tail at $|z| > 2mm$ is due to symmetric ($\vartheta_1 \simeq \vartheta_2$) events, where resolution drops because of a "broadening" of the pixels in the Microstrip (see section 5.2.2).

Observable (FWHM)	**all-tracks**	**'3'-tracks**	**EDDA**
azimuthal angle : $\Delta\varphi$	1.56°	0.85°	1.9°
polar angle : $\Delta\vartheta$	1.13°	0.48°	1.0°
vertex-position z : Δz $[mm]$	—	< 0.3	—
vertex-position x/y : $\Delta x/\Delta y$ $[mm]$	—	≤ 0.3	—
TOF : ΔTOF $[ps]$	≈ 780	< 780	—

Table 5.3: *Performance of the TOF detector using elastically scattered events and after TofRoot-calibration. All values represent the FWHM of the observable under consideration. For a comparison, the performance of the EDDA detector, as cited in [Sco01], is given in the last column.*

Chapter 6

Measurement of the Reaction $pp \rightarrow d\pi^+$

6.1 Introduction

The reaction $pp \rightarrow d\pi^+$ has been extensively studied during the past four decades and has considerably aided a deeper understanding of the hadronic force and the properties of hadronic matter. For example, the spin and the parity of the pion (π^+) were deduced[1] from $pp \rightarrow d\pi^+$ and its inverse reaction $\pi^+ d \rightarrow pp$ [Loc70]. Today, the experimental data (e.g. [Bet01], [Ply99], [Dro96], [Fel91], [Gla84], [Bar88], [Sah83]) and the theoretical description (e.g. [Hor94], [Nis96], [Arn93]) seem to be quite complete. However, the majority of experiments examined the low-energy region close to threshold and the influence of the $\Delta(1232)$ around $p_{beam} \approx 1260\,MeV/c$. At higher beam momenta ($p_b > 2000\,MeV/c$) the data is rather incomplete compared to the low-energy region. This situation is depicted in Fig. 6.1, where a compilation of the world data on total cross sections is shown.

The "fading" of experimental results above $p_b > 2000\,MeV/c$ has three main reasons:

1. With increasing excess energy the total cross section rapidly decreases ($\propto p^{-4}$), as higher relative energies in the exit channel suppress the formation of the deuteron.

2. Most accelerators cannot provide (proton) beams in the necessary (intermediate) energy range.

3. Due to the reaction pattern, it is not at all easy to separate $pp \rightarrow d\pi^+$ from the background reactions $pp \rightarrow pp\pi^0$, $pp \rightarrow pn\pi^+$, and elastic scattering; the more so as all background reactions have two orders of magnitude larger cross sections.

The currently available experimental data above $2000\,MeV/c$ were mainly provided by three experiments, performed during the last three decades. In the early 1970s, Anderson [And74][And71a] has examined $pp \rightarrow d\pi^+$ in a series of measurements ranging from $3000\,MeV/c$ to $5000\,MeV/c$. The measured angular distributions stand out

---

[1] Using the principle of *detailed balance* and "spin-gymnastics".

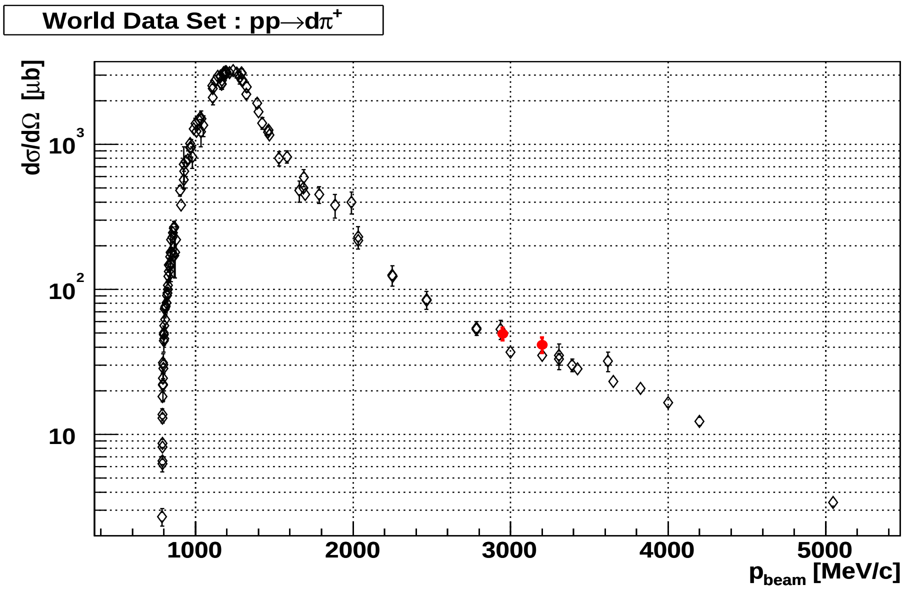

Figure 6.1: *Collection of the world data on total cross sections for the reaction* $pp \to d\pi^+$*. While for small incident beam momenta a wealth of data is present, the data set becomes rather scarce for higher momenta. The results of this work are added to the picture in red (*$2950\,MeV/c$ *and* $3200\,MeV/c$*)*

for their impressing accuracy, and they show a strong energy dependence. This is shown in Fig. 6.2: Starting from closely below $3000\,MeV/c$ a new process governs the production dynamics, which leads to the emission of the reaction products predominantly to small CMS angles. This indicates the contribution of a nuclear resonance, which could be the $\Delta(1950)$. Bertini [Ber88][Ber85] has extended the data towards smaller beam momenta ($p_b < 3000\,MeV/c$), one decade later. Using a polarization experiment, the results provide deeper insight into the production dynamics by the observation of analyzing powers. Finally, the data published by Yonnet [Yon93] in the 1990s extend polarization measurements up to $3200\,MeV/c$. Here, a *polarized* proton beam ($2000\,MeV/c \leq p_b \leq 3200\,MeV/c$) incident on a liquid hydrogen target was used. Significant structures in various excitation functions are observed. The reason for these structures is so far not completely understood by theory. They may be caused by the opening of higher $N\Delta$ orbital momentum channels (predicted by [Nis78]) or by a production mechanism which is correlated to the free π^+p elastic cross section [And71b]. Dibarionic resonances or heavy meson exchange may also be a possible scenario [Hai96].

Today, experimental and theoretical progress, for the reaction $pp \to d\pi^+$ at higher energies, seems to be in a vicious circle: The theoretical interest is modest, mainly because of the difficulty to include the (many) contributing partial waves into the theoretical description [Sib03][Han03]; therefore, this reaction channel is moved out of focus also from the experimental point of view, which, in return, slows down theoretical progress. However, the physics of this system is exciting, as, for instance,

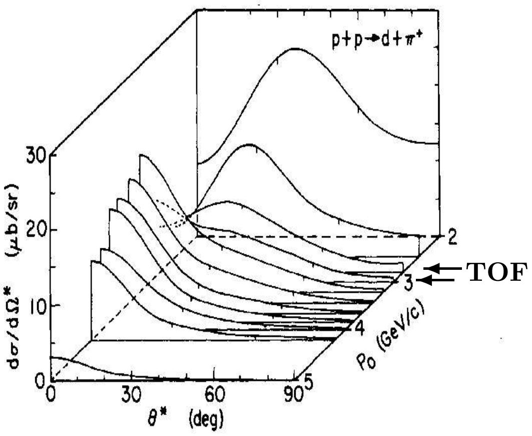

Figure 6.2: *The angular distribution of the reaction* $pp \to d\pi^+$ *(CMS) is shown as a function of the incident beam momentum. It reveals a drastic change for the production mechanisms involved: The "bump" at* $\vartheta_{CMS} \approx 40°$ *diminishes and a clear preference for forward angles appears. This could indicate the contribution of a resonance such as the* $\Delta(1950)$ *to the production dynamics. The most dramatic change occurs just at the momenta examined in this work (arrows).*
The figure is taken from [And74].

Fig. 6.2 shows clear evidence for a process, which since three decades is not (finally) understood. Further experimental data are needed, ideally obtained without too much effort, to reanimate theoretical work.

The Reaction $pp \to d\pi^+$at COSY-TOF

The COSY accelerator provides a (polarized) beam of high quality and the available beam momenta can range up to $\approx 3680\,MeV/c$. Therefore, the COSY facility is ideal in order to verify and extend the previously obtained experimental findings. However, the design of the TOF detector was not optimized to detect $pp \to d\pi^+$: Missing particle identification complicates the event reconstruction. On the other hand, the large solid angle coverage may be an enormous advantage, especially for polarization experiments.

The data discussed in this work originates from a beamtime, where an unpolarized beam was incident on a liquid-hydrogen target (January 2000, $p_{beam} = 2950\,MeV/c$ and $3200\,MeV/c$). The reaction $pp \to d\pi^+$ was preselected by the same trigger as elastic scattering (two-prong trigger), which was suppressed by a factor of 256 with regard to the "main" trigger. This implies that the data presented here (one week for each energy) represents ≈ 40 minutes of a measurement without scale-down. Still, about 1000 (500) events could be extracted for the lower (higher) energy. From this, total as well as differential cross sections could be evaluated which agree reasonably well with the data published so far. This demonstrates the performance of the TOF detector as well as the quality of the TofRoot calibration.

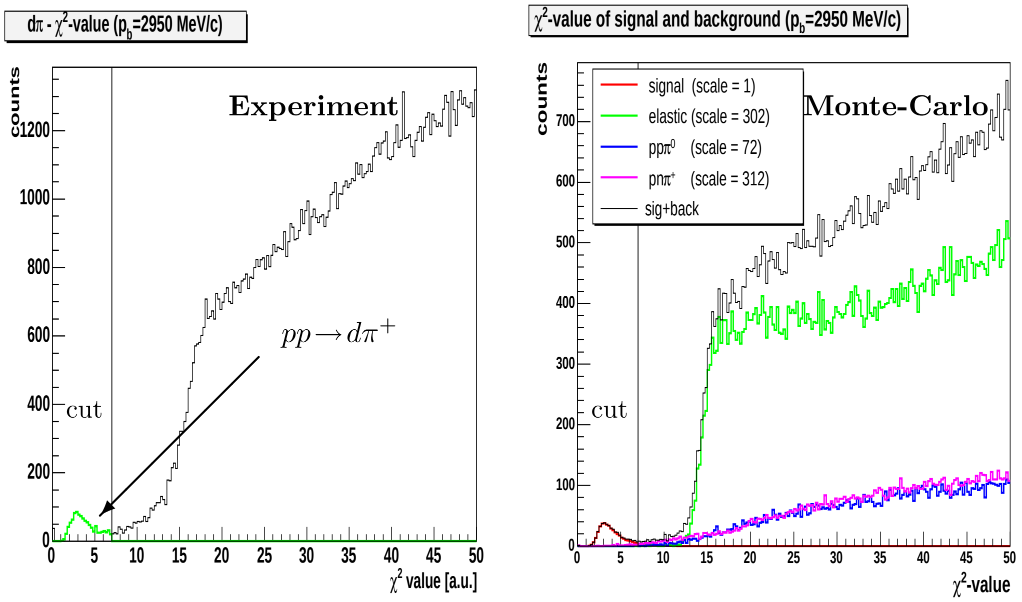

Figure 6.3: *$pp \to d\pi^+$: Separation of signal and background. The distribution of the χ^2-value is shown for detector and Monte-Carlo data. The background reactions are considered with their realistic total cross sections. In both cases a clear separation of the signal is visible (cut at $\chi^2 = 7$). The background-admixture is found to be $< 10\%$ for both energies.*

6.2 Data Analysis

6.2.1 Event Selection and Background Correction

The event selection is carried out in an analogous manner as described in the last chapter: A χ^2 value is calculated using all available information (ΔTOF^2, collinearity in the CMS, β-measurement in the Microstrip, point of closest approach, distance of closest approach, track fit quality). Compared to elastic scattering, the situation here is aggravated by the missing particle identification[3]. The only measured observables are two *velocity vectors*, and it is not known beforehand which of the two prongs is the deuteron/pion. Therefore, the χ^2 value is calculated for both possibilities, interchanging the deuteron and pion masses. Figure 6.3 depicts the χ^2-distribution for experimental and Monte-Carlo data, where for the latter the main background reactions are also shown: Elastic scattering, $pp \to pp\pi^0$ and $pp \to pn\pi^+$. The background reactions enter analysis according to the ratio of their total cross section compared to the desired reaction[4] ($N_{bg} = \sigma_{bg}/\sigma_{pp\to d\pi^+}$). A look at these factors illustrates the

---

[2] See footnote on page 78.

[3] Since late 2000, particle ID is possible using the newly installed Calorimeter ($\vartheta < 10°$).

[4] In practice, a fixed number of events is generated for all reactions. The proper adjustment for the cross sections is then achieved by *scaling* the output. This is necessary since otherwise 31.2×10^6 $pp \to pn\pi^+$events would have to be generated in order to be compared with 10^5 $pp \to d\pi^+$ events.

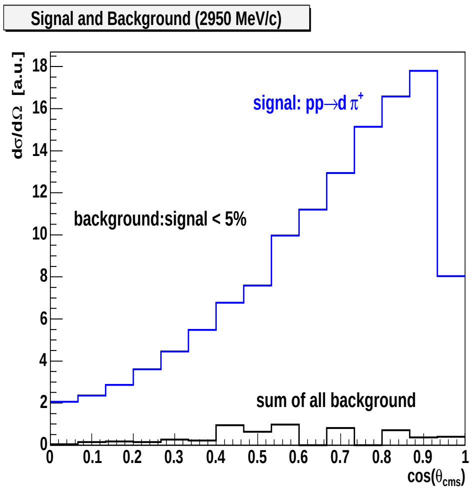

Figure 6.4: *The contamination of the signal (w/o acceptance correction) with background reactions is quantitatively examined using Monte-Carlo methods. The background reactions enter the analysis with weights according to their total cross section. The angular distribution of* $pp \to pp$ *is considered as measured in the previous chapter. The other two reactions are assumed to have a similar angular distribution as* $pp \to d\pi^+$. *The resulting background distribution is rather flat. Each bin of the measured angular distribution is therefore corrected by multiplication with a constant factor.*

difficulty to cleanly extract the signal:

$$N_{d\pi^+} : N_{pp} : N_{pp\pi^0} : N_{pn\pi^+} = \sigma_{d\pi^+} : \sigma_{pp} : \sigma_{pp\pi^0} : \sigma_{pn\pi^+} = 1 : 72 : 72 : 312 \qquad (6.1)$$

In spite of the unfavorable cross section ratios, a clear enhancement of $d\pi^+$ occurs at small χ^2-values. An event is positively identified as $pp \to d\pi^+$ if $\chi^2 < 7$. The main contribution of background is caused by $pp \to pn\pi^+$, and the total contribution can be evaluated to be 4.6% (9.8%) for 2950 MeV/c (3200 MeV/c). The χ^2-distribution of signal *as well as* background is rather similar for experiment and Monte-Carlo, which gives confidence in the method used.

Although the total contamination of the signal by background is small (< 10%), figure 6.3 does not establish to which extent the background contributes to the angular distribution. If only particular phase-space volumes of the background reactions are allowed to be "mis-identified" as $pp \to d\pi^+$, this could manifest itself in an enhanced contribution to particular bins of the angular distribution. In addition, the angular distribution of the background itself has to be considered. Unfortunately, at these high energies, $d\sigma/d\cos\vartheta$ is fairly unknown for $pp \to pp\pi^0$and $pp \to pn\pi^+$. Therefore, the background was assumed to be distributed similar to $pp \to d\pi^+$, which enhances events at $\cos(\vartheta) \to \pm 1$. This, in first order, is probably adequate, since the production of *one* (light) pion should be favored at small momentum transfers q^2. In this case, one of the nucleons is emitted to forward angles[5]. The angular distribution of elastic scattering enters analysis with the measured distribution as determined in the previous chapter. The resulting background distribution is shown in Fig. 6.4. Fortunately, no peculiar "spikes" are observed; the background rather adds with equal strength to each bin of the angular distribution. Since the uncertainty due to the "guessed" angular distribution is large, and the statistical significance of the background distributions is low[6], the background was subtracted with uniform weight from each bin of the experimental data.

---

[5] First results of an ongoing analysis of $pp \to pp\pi^0$support this assumption.

[6] For Fig. 6.4, already 10^6 Monte-Carlo events are used as input.

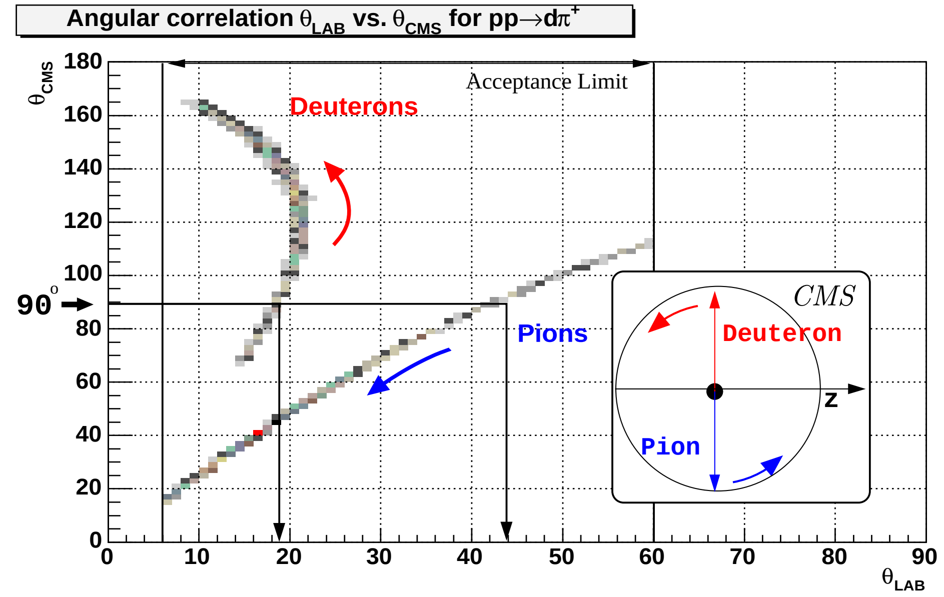

Figure 6.5: *The pion and the deuteron have to be detected in coincidence. Hence, both particles have to be within the acceptance range of* $6^\circ \leq \vartheta_{lab} \leq 60^\circ$*. While the deuterons are kinematically constrained to angles smaller 25° this is not true for the pions. However, all pions emitted into the forward hemisphere in the CMS are found in the laboratory system with angles smaller than 45°. (The acceptance range is chosen more strictly then the total acceptance of the TOF-spectrometer. This improves the quality of the acceptance correction.)*

6.2.2 Acceptance Correction

The kinematic situation for $pp \rightarrow d\pi^+$is sketched in Fig. 6.5, where the CMS angle of the pions and the deuterons is shown as a function of the their laboratory angle. While the (heavy) deuterons all are constrained to angles smaller 25° in the laboratory frame, this is not true for the pions. A considerable amount of pions leave the detector undetected at angles larger 60°, since the pion mass is much smaller than the deuteron mass and the excess energy is high. However, a kinematic specialty of this channel still allows the measurement of the *full* angular range ($\cos(\vartheta_{CMS}) \in [-1, 1]$), as will be explained in the following:

In the CMS, the reaction products have to be “back to back”, which is depicted in Fig. 6.5 on the right. Pions emitted at $\vartheta_{CMS} < 90^\circ$ (forward hemisphere) coincide with deuterons at $\vartheta_{CMS} > 90^\circ$ (backward hemisphere). Following the red and blue arrows in the same picture shows where these particles are found in the laboratory frame: *Both* the pions *and* the deuterons are found at $\vartheta < 45^\circ$. Hence, both tracks are not only within the (general) detector acceptance, but also in the acceptance range of the Erlangen-Start, i.e. *both* tracks provide high-quality track information. Therefore, the whole angular range of $pp \rightarrow d\pi^+$ is accessible, if we restrict the analysis to pions in the “forward” and deuterons in the “backward” CMS hemisphere. This restriction only reduces the number of total events by a factor of two, but does not effect the

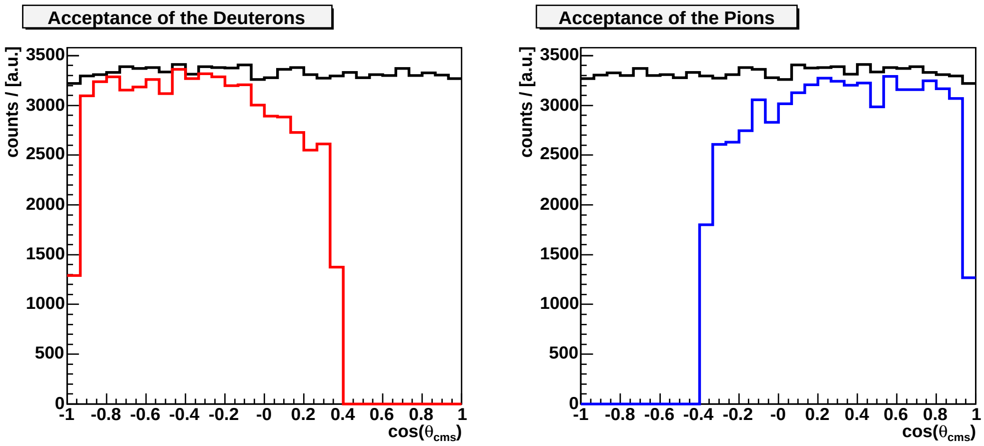

Figure 6.6: *Determination of the acceptance for the reaction $pp \to d\pi^+$: The isotropically distributed input (from the event-generator) is plotted in black, and the reconstructed events (same analysis as "experiment data") are plotted in red/blue. Events with Pions (right) can only be detected with high acceptance if they emerge into the forward hemisphere in the CMS, which corresponds also to "forward" angles in the laboratory system. The reaction partner (the heavier deuteron) is found at backward CMS angles.*

physical output (angular distribution), since the observed reaction is symmetric in the entrance channel.

The result for the acceptance determination is shown in Fig. 6.6. Monte-Carlo data is used where, analogously to elastic scattering, the cosine of the polar angle in the CMS is sampled twice: (a) for all *input* events created by the event generator; (b) for the *reconstructed* events. The ratio (a/b) of both yields the acceptance for each bin, which then is applied bin-per-bin to the experiment data. Considering the pions and deuterons separately in "their" hemisphere, the acceptance is well above 85%, except for the bin at $\cos\vartheta \approx \pm 1$. Here, acceptance drops due to an intended software-cut ($\vartheta_{lab} > 6°$): When approaching the kinematical limit of a reaction, it often is advantageous to use a clearly defined software-cut. This cut is used for both detector *and* Monte-Carlo data, which enhances the comparability of the data sets and leads to a higher quality of the acceptance correction.

6.2.3 Angular Distribution

The angular distributions of $pp \to d\pi^+$ for both beam momenta ($2950\,MeV/c$ and $3200\,MeV/c$) are shown in Fig. 6.7. The colors indicate which particle was actually measured (pions=blue, deuterons=red). The error bars (x,y) reflect the bin-size and the statistical uncertainty, respectively. As in elastic scattering, the graph is not symmetrized in order to underline the independence of the measurements[7]. The data is background and acceptance corrected for each bin as described above. The normalization was carried out using the luminosity determined from elastic scattering. A

---

[7] Of course, both tracks are strongly correlated kinematically, but are measured independently.

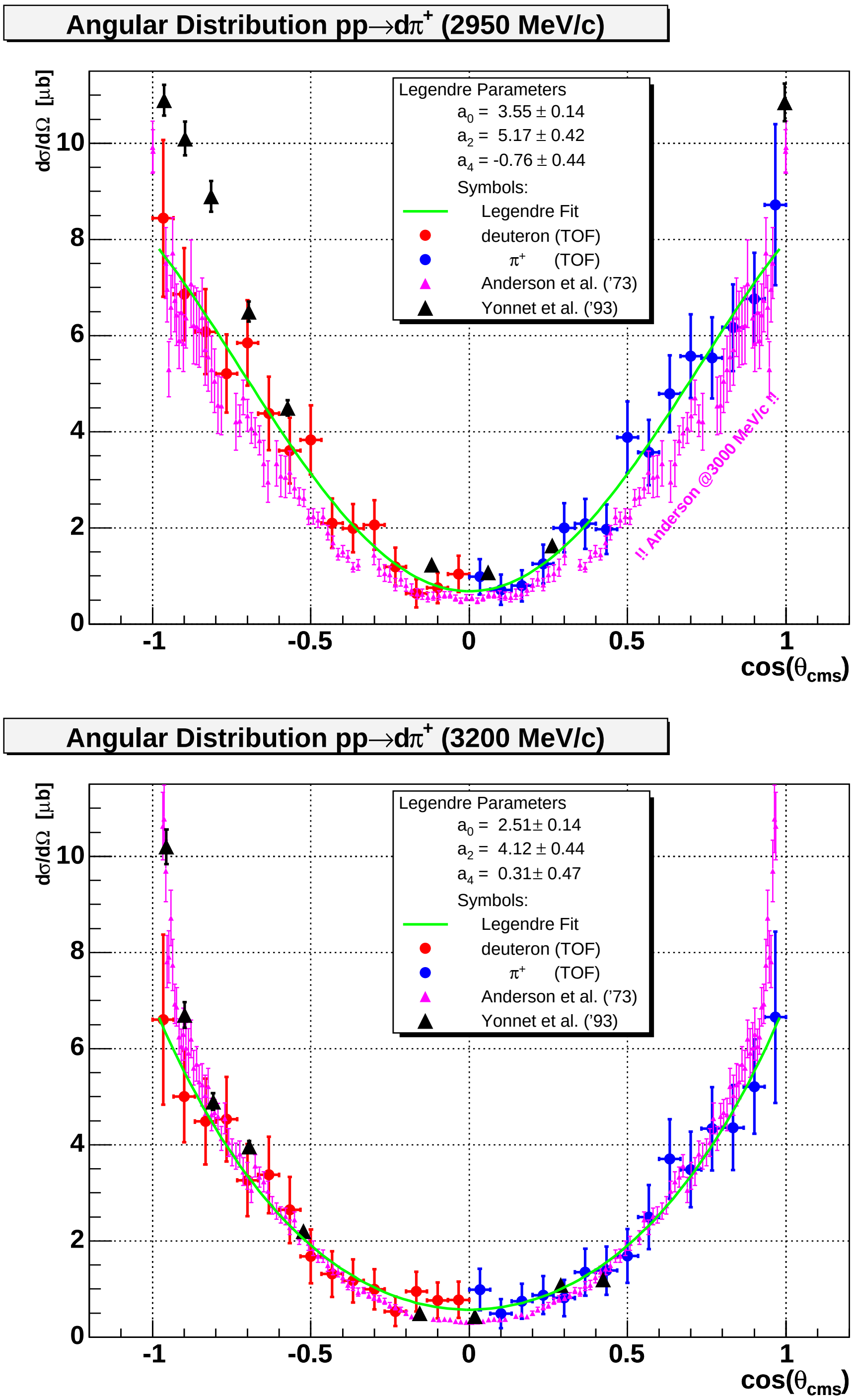

Figure 6.7: *Angular distributions for* $pp \to d\pi^+$ *measured with the the TOF detector (acceptance corrected, background subtracted, luminosity applied). The error bars reflect the bin size and statistical uncertainty, respectively. The measurements of Anderson [And74] and Yonnet [Yon93] are depicted as well. The incident beam momenta of all three experiments are identical, except for Anderson at the smaller beam momentum (Anderson:* $3000\,MeV/c$*). The green lines are Legendre-fits to the presented data (first three even coefficients:* a_0, a_2, a_4*).*

Legendre fit is applied to the data (green line), which yields results for a_0, a_2, a_4 as listed in Tab. 6.1.

The data of Yonnet [Yon93] and Anderson et al. [And74] are added in the figure. At “2950MeV/c” the beam momentum used by Anderson is slightly different (3000 MeV/c). This difference in incident beam momentum is responsible for the absolute shift towards smaller cross sections. Besides this shift, the agreement with Anderson's data is perfect within uncertainty limits. The overall distribution and even the discontinuities at $\cos(\vartheta) = \pm 0.3, \pm 0.6, \pm 0.8$ are “reproduced” by the TOF-measurement. Yonnet's data show a slight trend to higher cross sections at angles near the beam axis. At 3200 MeV/c the beam momenta used in all three experiments are alike. The agreement of Anderson and Yonnet is superb. The TOF-data compares to these rather well, although near $\cos\vartheta = 0$ TOF overestimates the differential cross section by a factor of ≈ 2 compared to the other experiments. Near $|\cos(\vartheta)| = 1$ the trend towards a steep slope is considerably smaller, although reproduced in general (a_2 and $a_4 > 0$). However, the statistical uncertainty limits the significance of the TOF-result at this energy with only ≈ 500 counts divided inhomogeneously into 15 bins.

Observable	**2950 MeV/c**	**3200 MeV/c**
a_0 $[\mu b/sr]$	3.55 ± 0.14	2.51 ± 0.14
a_2 $[\mu b/sr]$	5.17 ± 0.42	4.12 ± 0.44
a_4 $[\mu b/sr]$	-0.76 ± 0.44	0.31 ± 0.47
σ_{tot} $(4\pi a_0)$ $[\mu b]$	$46.6 \pm 1.8 \pm 4.1$	$31.5 \pm 1.8 \pm 3.2$
σ_{tot} $(\Sigma\#)$ $[\mu b]$	$48.2 \pm 1.5 \pm 4.2$	$34.0 \pm 1.5 \pm 3.4$

Table 6.1: *Results for $pp \rightarrow d\pi^+$: The Legendre parameters are taken from the fit shown in Fig. 6.7. The total cross section is calculated twice; (1) by multiplying the leading Legendre parameter (a_0) by 4π, and (2) by the total number of counts. For the first method, the uncertainty is taken from the variance of the fit parameter a_0. For the second, the uncertainty reflects the statistical error. For discussion of the systematical uncertainty please refer to the text.*

6.2.4 Total Cross Section

The total cross section can be calculated using two different methods:

1. Counting the total number of events positively identified to come from the desired reaction, subtracting the background, correcting for acceptance, and then considering the integral luminosity.

2. Since all positively identified events contribute to the angular distribution, the total cross section can be extracted from its integration over the full angular range. This task can be fulfilled by integrating a numerical parameterization of the angular distribution. As is shown in Fig. 6.7 and Tab. 6.1, one possible parameterization is to use a sum of even[8] Legendre polynomials

---

[8] Since the entrance channel is symmetric only even coefficients contribute.

($\frac{d\sigma}{d\Omega} = \Sigma_{l=0}^{n} a_{2l} P_{2l}(\cos\vartheta)$). In order to determine the total cross section this parameterization is very advantageous: It is a characteristic of Legendre polynomials that the integral over the full angular range vanishes for *all but the first* addend, i.e. ($\int_{-1}^{1} P_l(\cos\vartheta) d\cos\vartheta = \delta_{0l}$). Therefore, the total cross section can be calculated using

$$\sigma_{tot} = \int_{-1}^{1} a_0 \cdot P_0(\cos\vartheta) d\cos\vartheta = \int_{-1}^{1} a_0 \cdot 1 \cdot d\cos\vartheta = 4\pi \cdot a_0, \tag{6.2}$$

i.e. simply multiplying the leading Legendre parameter a_0 by 4π.

The total event count of 1028 (549) at 2950 MeV/c (3200 MeV/c) yield a total cross section of $(48.2 \pm 1.5)\,\mu b$ ($(34.0 \pm 1.5)\,\mu b$), while $4\pi \cdot a_0$ results in $(46.6 \pm 1.8)\,\mu b$ ($(31.5 \pm 1.8)\,\mu b$). Both methods fully agree within uncertainty limits, which are discussed in more detail below. Figure 6.1 shows the final result in comparison with the world data.

Experimental Uncertainties

The modus operandi to analyze $pp \rightarrow d\pi^+$ is very similar to the elastic scattering, but the experimental uncertainties are much higher[9]. The small cross section leads to a total of about 1000 events only, which causes a significant statistical uncertainty of 3.1%. In addition, the unfavorably small cross section leads to a very sensitive behavior of the background estimation: Shifting the χ^2-cut value by ±1, the percentage of the background contribution changes from $\approx 5\%$ to $\approx 12\%$ and $\approx 2\%$, respectively. Therefore, although the background seems to be well understood (see. 6.3), the contribution to the systematic uncertainty is estimated to be ±6%. The situation is slightly better for the acceptance correction, because the method used is similar to the procedure for elastic scattering; since elastic scattering is used for the determination of the luminosity, any systematic error will (partly) cancel. Anyhow, the acceptance is $\approx 85\%$, hence the cut rejects a significant number of "real" events. A contribution of 5% to the total uncertainty seems to be a reasonable and conservative estimate. The statistical, systematic, and total uncertainties are listed in Tab. 6.2, where the total uncertainties are the quadratic sum of the single contributions.

In the case of the angular distribution, we have to distinguish between the uncertainty of the distribution itself (the Legendre fit), and the uncertainty of each bin. In Fig. 6.7 only the statistical uncertainty is plotted for each bin. Since the statistical basis is poor, these uncertainties are already considerably large. However, the fit accounts for these uncertainties and transforms them to errors for each Legendre coefficient. Therefore the (statistical) uncertainty of the total cross section calculated by the "$4\pi a_0$-method" is directly given by the uncertainty of the first coefficient. The systematic uncertainty is as described above, since the acceptance and the background correction is applied with the same factor for each bin.

If we now consider the uncertainty of each bin, the picture gets more complicated:

---

[9] The discussion will take the 2950 MeV/c measurement as an example. The values for the higher energy are listed in Tab. 6.2.

Uncertainty	**2950** MeV/c	**3200** MeV/c
Background Subtraction	6.0%	7.0%
Acceptance Correction	5.0%	6.0%
Luminosity	3.8%	3.8%
Total (sys)	8.7%	10.0%
Statistical	3.1%	4.3%
Total	8.9%	10.9%

Table 6.2: *Statistical and systematical uncertainties for* $pp \to d\pi^+$. *The statements are (strictly) valid only for the total cross section. The single bins of the angular distribution have a higher uncertainty due to the background subtraction.*

The overall background contamination is in the order of 10%. However, it is not excluded that the background contributes to *some of the* bins with considerable amount. This could be the case in the region around $\cos\vartheta = 0$, where the differential cross section is measured to be about double the size of the other experiments. Besides physical explanations, it could also be the origin of the discontinuities observed in the spectrum. The acceptance drops to less then 50% for the most outer bin at $|cos(\vartheta)| \approx 1$, because the acceptance limit of the detector is reached. This causes an additional uncertainty for this particular bin in the order of 20%. Unfortunately, this point is crucial for the physical interpretation of the measured spectrum, as Fig. 6.2 showed that the behavior of the angular distribution changes dramatically in the observed energy region.

6.2.5 Discussion and Outlook

Since the data used for this analysis is obtained from the “elastic trigger” (suppressed by a factor of 256!), it can not be expected that the results reveals revolutionary new physics. The statistical significance, especially for the angular distribution, is too poor. However, the analysis has proven to reproduce the previously published results with reasonable consistency.

Differential observables, and their *energy dependence*, are the key to understanding the reaction dynamics of $pp \to d\pi^+$. Therefore, angular distributions and spin observables have to be measured with high precision. The angular resolution of the TOF spectrometer is in the order of 1°, and, due to the azimuthal symmetry, it is well suited for measurements of polarization observables. Provided a sufficient statistical basis, the quality of angular distributions is superb, as was shown in the previous chapter (see Fig. 5.6). Therefore, and in conjunction with an improved background evaluation, the differential observables of $pp \to d\pi^+$are certainly measurable with the same accuracy as the elastic scattering.

It has to be pointed out that the elastic scattering, and thus also the reaction $pp \to d\pi^+$, is measured in each beamtime. Using the data acquired at beamtimes of the past will provide data (for different beam momenta) “for free”. Setting the elastic trigger scaling less stringent in future beamtimes, especially during polarization experiments, will allow to measure the excitation functions with high accuracy.

A beamtime to examine ω production is scheduled for spring 2004. The Dresden group is responsible for this beamtime, and it is planned to measure the “two-prong” channel with less suppression. COSY will provide a *polarized* beam, scanning two to four different beam momenta in the rage of $2800 - 3400\,MeV/c$. According to Fig. 6.2, this is exactly an energy range, where dramatic changes of the reaction dynamics are to be expected. In addition with polarization observables, TOF will (hopefully) provide new and interesting data for theory regarding the reaction $pp \rightarrow d\pi^+$.

Chapter 7

Measurement of $pp \rightarrow pp\omega$

7.1 Introduction

The mesons of the pseudoscalar ($J^p = 0^-$) and the vector ($J^p = 1^-$) nonets have been known to modern particle physics for a very long time. In fact, the lightest participating meson - the pion - was already postulated by Hideki Yukawa in 1935 [Yuk35], and experimentally proven by C.F. Powell in 1947 [Pow59]. Since then, the experimental and theoretical progress has been tremendously successful in predicting, identifying, and organizing the meson families, mainly using pion or electron beams. However, in spite of the fact that mesons are believed to be the exchange bosons of the nucleon force, it was not until the early 1990s that meson production was studied comprehensively in *nucleon-nucleon (NN)* interactions. Since then, a wealth of data has been accumulated for the relatively easy-to-measure pseudoscalar family ($J^P = 0^- : \pi^{+,0,-}, \eta, \eta', K^{+,0,-}$). A compilation of the world data on total cross sections was already shown in Fig. 1.1.

The production of vector mesons ($J^P = 1^-$) in NN-collisions came into focus later, as in 1996 A.A. Sibirtsev pointed out that "*heavy-meson production in proton-proton collisions is one of the most unstudied subjects in nuclear physics*" [Sib96]. He proposed a one-pion-exchange model which holds up remarkable well even today. This triggered an considerable interest in vector meson production, both experimentally and theoretically.

7.1.1 Motivation

The measurement of vector meson production is inherently of interest to experimental and theoretical nuclear physics, since new results will allow a deeper insight into the *nature* of meson production itself, viz. an understanding of the fundamental processes involved. However, the reaction dynamics are of crucial importance also for many other fields of modern physics. This will be discussed briefly in the following.

Nucleon-Nucleon Force

The (repulsive) short range part of the NN-forces is dominated by the isoscalar ω-meson exchange [Mac89]. According to the uncertainty principle, the spatial scale of these interactions is on the order of $1 - 0.2\,fm$, i.e. at the boundary between nuclear physics and QCD. A theoretical description of these interactions should therefore include both: (1) meson exchange, and (2) the onset of a contribution of QCD (quark-gluon interactions). To discriminate between different theoretical approaches, the properties of the "free" vector meson production (scattering lengths, coupling constants, spin observables) have to be known precisely.

Dense Matter

The physics of (extremely) dense matter is of growing interest in the field of cosmology (neutron stars, big-bang) and (U)RHICs[1]. Dilepton spectroscopy [CER95] discovered a significant enhancement of vector mesons within dense matter, compared to thermodynamical predictions. This can be explained by a change of the quark condensate which manifests itself in a mass shift of vector mesons [Bro91]. The same behavior is also suggested by QDC sum rules [Koi93][Hat92]. Alternatively, vN resonances are proposed to explain in-medium effects: These resonances do not (or only weakly) couple to the πN-, but predominantly to the vN-channel. In dense matter the probability of nucleon excitation is high so that vN-resonances could significantly contribute to vector meson production.

In the case of the ω meson no experimental evidence for a ωN-resonance is found, up to now. However, their existence is predicted by many theoretical models[2] ([Isg79], [Koh80], [Cap94], [Oh01], [Pen02a], [Pen02b], [Tit02a], [Tit02b]). Only additional experimental data can clarify the situation, as any description of dense nuclear matter needs an accurate knowledge of the elementary processes involved in vector meson production as an inevitable prerequisite.

Strangeness Content of Nucleons

We already know from deep inelastic scattering (DIS), that the picture of just three valence quarks composing a nucleon is too simple - gluons and sea-quarks also have to be taken into account. However, the flavor decomposition of the sea is not precisely known, especially for small momentum transfers q^2. Recently, the ZEUS collaboration has found first evidence for the strange sea ($s\overline{s}$) at "small" momentum transfers 10 $\text{GeV}^2 < |q^2| < 100\,GeV^2$ [ZEUS03]. However, ZEUS also used DIS, which probes the nucleon only using electromagnetic interactions. A comprehensive picture of the $s\overline{s}$-contribution to the nucleonic wave function is believed to be achievable only by use of hadronic probes.

Especially the comparison of the reaction dynamics of ω and ϕ mesons is a promising subject of present theoretical and experimental studies. This comes about, since the flavor eigenstates (ω_0, ω_8) of the vector nonet are arranged in such a way that the mass eigenstates (ϕ, ω) form a (quasi) ideally decoupled system ($|\phi\rangle \cong |s\overline{s}\rangle, |\omega\rangle \cong |u\overline{u}\rangle \oplus |d\overline{d}\rangle$). The small deviation of 3.7° from the "ideal mixing angle" of 35.3° ($\Leftrightarrow \sin(\theta) = 1/\sqrt{3}$) yields the $|u\overline{u}\rangle \oplus |d\overline{d}\rangle$ admixture in the ϕ wave function.

According to the OZI-rule [Zwe64], processes involving disconnected quark lines are

---

[1] (**U**ltra) **R**elativistic **H**eavy **I**on **C**olliders (**C**ollisions)

[2] Due to the lack of experimental confirmation these resonances are often called *missing resonances*.

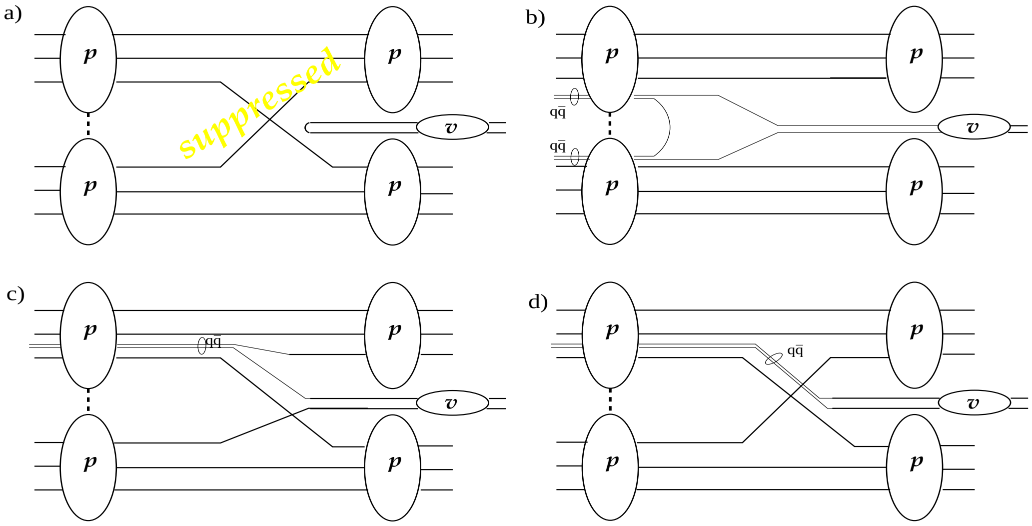

Figure 7.1: *Schematic quark-line diagrams for the vector meson production. a) According to the OZI-rule, processes including disconnected quark lines (production* from the "vacuum"*) are strongly suppressed. The other three diagrams show the OZI-allowed cases for "pure sea-quark production" (b),* rearrangement *(c), and* shakeout *(d), respectively.*

strongly suppressed[3]. This is sketched in Fig. 7.1: The production of (vector) mesons "from the vacuum" should be strongly suppressed (a) with respect to processes where a $q\overline{q}$-pair is "present" in the nucleon. However, if the nucleon is composed purely of non-strange u and d quarks (*no* $s\overline{s}$ content), then also the other three cases depicted in Fig. 7.1 can not contribute to the $|\phi\rangle \cong |s\overline{s}\rangle$ meson production. The dominant mechanism to create a ϕ meson is then via the small, *and calculable*, admixture of *non-strange* quarks to the ϕ meson's wave function. The ω-meson, on the other hand, can be created by "normal", non-strange sea quarks with a larger abundance. Using the assumption of zero strangeness content in the nucleon wave function, we can calculate the expected ratio of the cross sections for ϕ to ω mesons[4],

$$\mathcal{R}_{\phi/\omega} = \frac{\sigma_{pp \to pp\phi}}{\sigma_{pp \to pp\omega}} = 4.2 \times 10^{-3}. \tag{7.1}$$

yet, experiment shows a strong deviation from this naive picture: $p\overline{p}$ annihilation[5] revealed a dramatic enhancement (×30) of the number of ϕ mesons produced, compared to the predictions based on the OZI-rule. In proton-proton interactions the experimental value of $\mathcal{R}_{\phi/\omega}$ is $(3 \pm 1)\%$, which is about 7 times larger than the OZI-prediction. This experimental finding often is denoted as *"violation of the OZI-rule"*[6]

---

[3] In the context of experimental hadronic physics "strongly suppressed" actually means "undetectable" or simply "forbidden".

[4] It is important to ensure the same volume of the phase space, i.e. to calculate the ratio at the same excess energy ϵ (= "total kinetic energy in the CMS" $= \sqrt{s} - 2 \cdot m_p - m_v$).

[5] Mainly provided by OBELIX [Fil00] and Crystal Barrel [Ams98] located at LEAR, CERN.

[6] Which is, exactly speaking, wrong: The OZI-rule is assumed to be *precise*, but the abundance of measured ϕ mesons is greater than the expectation.

or *"deviation from the SU(3) prediction"*.

To clarify this situation, the total cross sections of ϕ *and* ω meson production have to be available as input to theory. In addition, further observables (angular distributions, spin correlations) have to be measured to pin down the reaction dynamics. For further discussion please refer to 7.3.3.

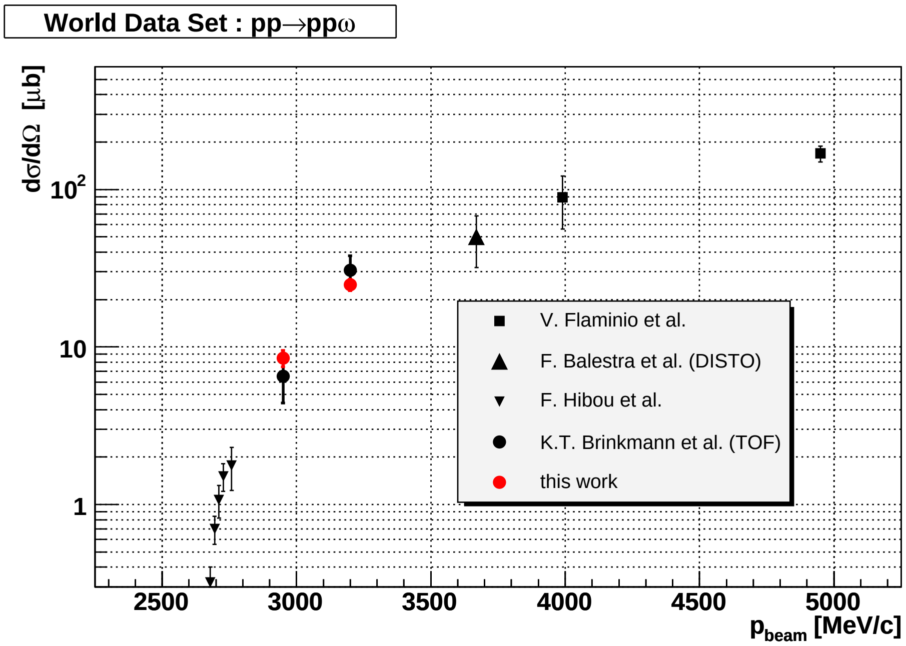

Figure 7.2: *A collection of the total cross sections for the reaction* $pp \rightarrow pp\omega$. *Except for the bubble-chamber measurements at the highest beam momenta, all error bars reflect the combination of statistical and systematic uncertainties. The TOF-data nicely closes the gap between 2800 and 3600 MeV/c. The results of this work are added in red.*

The presented cross sections are taken from [Fla84][Bal01][Hib99][Bri01] (top down).

7.1.2 Status Quo and Objectives: Experiment

Vector meson production (ρ, ω, ϕ) in nucleon-nucleon interactions remained largely unstudied in the last century. Experimental data (if any) was scarcely available and resulted from hydrogen bubble chambers. Data near production thresholds were completely lacking. Due to the advent of a new generation of accelerators and detectors[7], first data on vector meson production started to be available in the late 1990s. A summary on all available total cross sections for the reaction $pp \rightarrow pp\omega$ (below $p_{beam} = 5\,GeV/c$) is given in Fig. 7.2. The two data points above $p_b = 4000\,MeV/c$ are taken from a data compilation [Fla84]. They are measured with bubble chambers, and therefore provide poor statistical significance. First experimental data for ω-meson production in the direct vicinity of the threshold was measured at the

---

[7] see 1.2.1

SPESIII-spectrometer located at SATURNE. They report total cross sections up to excess energies of $\epsilon = 30\,MeV$ [Hib99]. The error bars reflect statistical and systematical uncertainties, which are comparable in size in this case. However, close to the threshold, the uncertainty of the beam momentum and the non-zero width of the ω-meson considerably influences the determination of the excess energy. Thus, these measurements also have a considerable uncertainty along the beam-momentum-axis, which aggravates the determination of the exact slope of the excitation function. The DISTO-collaboration contributed to the world data set in 1998 with a measurement at a beam momentum of $p_b = 3670\,MeV/c$ [Bal98][Bal01]. This yielded total cross sections and *angular distributions* not only for the ω meson ($\epsilon = 320\,MeV$), but also for the heavier ϕ meson ($\epsilon = 83\,MeV$). The systematical uncertainty of these measurements are large ($\approx 26\%$), due to normalization to the not very well known η cross section.

In the same year, the TOF-collaboration published data on ω production for beam momenta of $2950\,MeV/c$ and $3200\,MeV/c$ [Bri01]. For both energies ($\epsilon = 93\,MeV$ and $\epsilon = 173\,MeV$) total cross sections, and for the higher energy, also differential cross sections could be elaborated. The data nicely closes the lack of experimental knowledge at intermediate beam momenta, and the angular distribution has attracted considerable interest on the part of theory.

Finally, this work will present total and differential cross sections for the same beam momenta as the preceding TOF analysis[8] ($2950\,MeV/c$,$3200\,MeV/c$). Due to the improved calibration provided by TofRoot the experimental uncertainties are smaller. The total cross sections are added in red to Fig. 7.2 and coincide with the previously published data within uncertainty limits. The angular distributions and invariant-mass spectra will be presented later in this chapter, but it should be pointed out already here that for the smaller energy, both distributions are new to the world data set.

In conclusion, the knowledge of even the most elementary processes in vector meson production near threshold is still very poor. Therefore, the aim of an experimentalist must be to first provide basic input to theory, where this is presently missing (e.g. total cross sections). After this, the dynamics of heavy-meson production will come into focus by measuring angular distributions, invariant-mass spectra, and spin observables.

7.1.3 Status Quo and Objectives: Theory

The advent of new experimental data has spurred considerable theoretical activity. This has led to the development of different theoretical models describing the elementary ω meson production in nucleon-nucleon interactions[9]. A pioneering approach developed already in 1996 and two more sophisticated approaches will be described in the following.

---

[8] Actually, the raw data sample used for this work to examine $pp \rightarrow pp\omega$ properties is *identical* to the raw data analyzed and published by K.T. Brinkmann [Bri01]. It has to be emphasized that, although the same data, the work presented here uses a totally different software (TofRoot) as well as different analysis strategies.

[9] In addition to nucleon-nucleon reactions, pion- and photo-induced vector meson production is intensively studied (e.g. [Pen02a][Pen02b][Tit02a]).

The One-Pion-Exchange Model (A.A. Sibirtsev)

When A.A. Sibirtsev developed his model for vector meson production in 1996 [Sib96], the experimental data-basis was very weak. In fact, the only data on total cross sections originated from bubble-chamber experiments and covered excess energies above $400\,MeV$ ($p_{beam} > 4000\,MeV/c$). However, the proposed model covers the energy range starting at threshold to kinetic energies as high as $10\,GeV$. The vector meson production cross sections are calculated within a (simple) one-pion exchange model. This was chosen since no previous theoretical approach existed. The main goal was to "test" how far a simple ansatz could reach, and from this to "*look to find room for the contribution from other mesons*".

The pion exchange diagram used is the most simple possible, i.e. pion exchange between the nucleons with a vector meson (V) originating from a πNV-vertex. The cross section for vector meson production is then calculated using

$$\begin{aligned}\sigma(NN \to NNV;\, \sqrt{s}) = {} & \frac{3m_N^2}{2\pi^2 p_i^2 s} \int_{W_{min}}^{W_{max}} kW^2\, dW \\ & \times \int_{t^-}^{t^+} \frac{f_{\pi NN}^2}{\mu^2} F^2(t) D^2(t) \quad \sigma(\pi N \to VN;\, W,\, t) t\, dt, \qquad (7.2)\end{aligned}$$

where $\sqrt{s}$ and W are the invariant masses of the colliding nucleons and the produced VN system, respectively; Furthermore, t is the squared four-momentum transfer from the initial to the final nucleon, $F(t)$ the pion form factor, and $D(t)$ the pion propagator. Besides these kinematic variables and functions, two main ingredients appear in Eq. 7.2: The coupling constant $f_{\pi NN}$ and $\sigma(\pi N \to VN;\, W,\, t)$, which is the V-meson production cross section in πN interactions averaged over all possible members of the isospin multiplets of the initial and final states. While the first is taken from theory, the latter are experimental input parameterized in a convenient manner.

As a result, the contribution of other (heavy) meson exchanges seems to be low to negligible. The experimental results since then have demonstrated the remarkably high predictive power of this model. Even at cross sections two orders of magnitude smaller then the available data of the time, the prediction comes within a factor of two of the data[10].

The Heavy-Meson-Exchange Model (K.Tsushima and K.Nakayama)

The model of K.Tsushima and K.Nakayama was first published in 1998 [Nak98]. Since then it has experienced a series of considerable improvements, mainly guided by new experimental data [Tsu03]. Vector meson production is described within a meson exchange model, where (in addition to the pion) also heavy meson exchange is incorporated. The contributing production processes are depicted in Fig. 7.3. The guiding phenomenological idea is that the meson production is governed by two processes:

---

[10] A simple parameterization of the excitation function 7.2 will be used in the discussion part of this chapter.

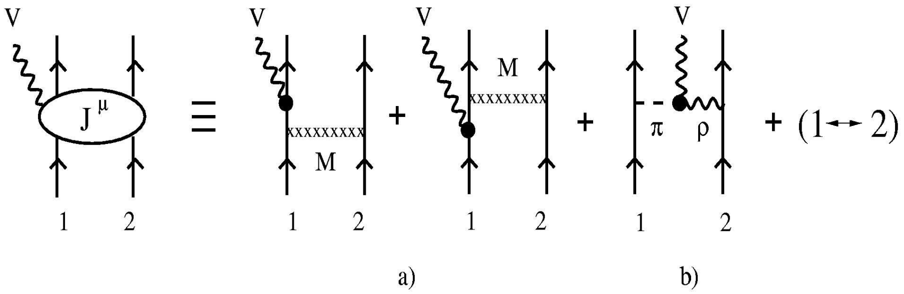

Figure 7.3: *Production currents for vector meson production ($V = \omega, \phi, \rho$): (a) nucleonic and/or resonant currents ($M = \pi, \eta, \varrho, \omega, \sigma, a_0$), (b) mesonic currents. The figure was taken from [Tsu03].*

a *nucleonic current* and a *mesonic current.* While in the first, the vector meson originates from a NVN vertex, in the latter it is emitted from a purely mesonic triple-vertex. Besides the inclusion of initial and final state interactions (ISI, FSI), the model was recently extended to also include *nucleon-resonance currents* [Tsu03]. The production currents are used to set up a relativistic effective Lagrangian. From this, vector meson production can be studied within the distorted wave Born approximation.

The relative strength of the three currents is described by a set of parameters; and as often encountered in theoretical models, a "proper" set of parameters is found to "reproduce" almost any experimental value. However, a central aim of this model is to find *one* set of parameters for the *simultaneous* description of total as well as differential cross sections. This parameter set should not only concur with established values found in modern nuclear potentials, but it should also be valid for various production channels (ω, ϕ, ρ) and the excess energies range up to $\approx 300\,MeV$. As shown in Fig. 7.4, the agreement with the experiment is quite encouraging. A parameter fit to all available data reproduces the angular distribution of the ω meson in the CMS rather well, although it indicates a more "cooking-pot like" behavior, which is in good agreement with the data which will be presented in this work (Fig. 7.12). At very small excess energies ($\epsilon < 30\,MeV$) the model underestimates the measured total cross sections by about a factor of two. This could have its reason in some unsolved model deficiencies, or originate from (experimental) threshold effects: Near threshold ($\epsilon \approx \Gamma_\omega$) it is unclear how to account for the *natural width* of the ω meson[11].

However, to further constrain the model parameters and to explore their region of validity, new experimental data is badly needed. Besides total cross sections, this means especially the measurement of differential observables (angular distribution, invariant mass distribution). Furthermore, the experimental data should cover all (charge-neutral) heavy mesons (ρ^0, ω, ϕ), preferably at various excess energies.

---

[11] Citation [Tsu03]: "*[The experimental problem] is because there is no established method to remove the multi-pion background associated with the ω-meson width from the raw data in order to extract the cross section.*"

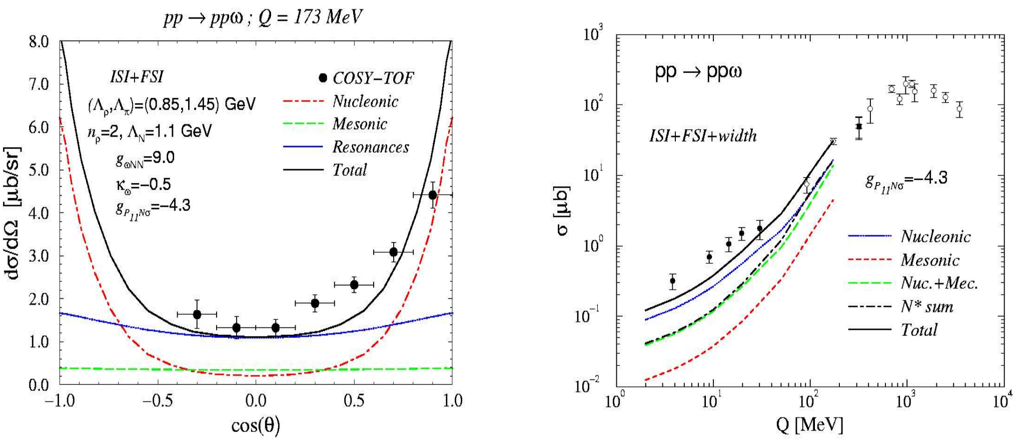

Figure 7.4: *Left: The angular distribution and the different contributions of mesonic, nuclear, and resonant currents. The parameters are adjusted to the published TOF data [Bri01]. Right: The energy dependence of the total cross section near threshold is underestimated by a factor of two. The figure was taken from [Tsu03].*

The Nucleon Resonance Model (C. Fuchs)

Recently, a new model based on nucleon resonances has been published [Fuc03]. It shows remarkable results, describing the total cross sections in the energy range from $5\,MeV$ up to several GeV above threshold. Unfortunately, this model does not provide predictions for angular distributions. In this model, the elementary ω production is described via a two step mechanism: (1) the excitation of one of the protons to a nucleon resonance ($NN \to NN^*$), and (2) the decay of this resonance into a nucleon and a vector meson ($N^* \to NV$). All well-established nucleon resonances[12] are included. The properties of these resonances (total and partial decay widths, coupling constants, form factors) are taken from fits to photo- and electoproduction data, a multichannel πN partial-wave analysis, and quark models.

In contrast to the previously discussed approaches, this model does not directly calculate the total cross section as a function of the excess energy. It rather describes *the distribution of the ω mass (M_ω)* in *pp*-interactions, which is equivalent to a description of the missing-mass spectrum[13]. A peculiarity of this model is that *real* (on-shell) as well as *virtual* (off-shell) ω mesons are considered. In case of an off-shell meson, the meson decays from on-shell nucleon resonances, but the mass of the resonance can be substantially *smaller* than the sum of the *pole* mass of the meson and the mass of the proton ($m_R \ll m_\omega + m_p$). Hence, an off-shell ω can be produced with masses far away from the pole mass. In fact, the threshold for off-shell ω production is the sum of the masses of the three-pion final state ($m_{\pi^+} + m_{\pi^-} + m_{\pi^0} = 414\,MeV/c^2 < 782\,MeV/c^2$). Experimentally, the contribution of the off-shell mesons, the *theoretical background*,

---

[12] All "4*" resonances according to [PDG]: $N^*(1440, 1520, 1535, 1650, 1675, 1680, 1720)$.

[13] Missing mass: $\vec{P}_b + \vec{P}_t = \vec{P}_1 + \vec{P}_2 + \vec{P}_\omega \Leftrightarrow \vec{P}_\omega = \vec{P}_b + \vec{P}_t - \vec{P}_1 - \vec{P}_2 =: M_\omega = \sqrt{E_\omega^2 - \vec{p}_\omega^{\,2}}$

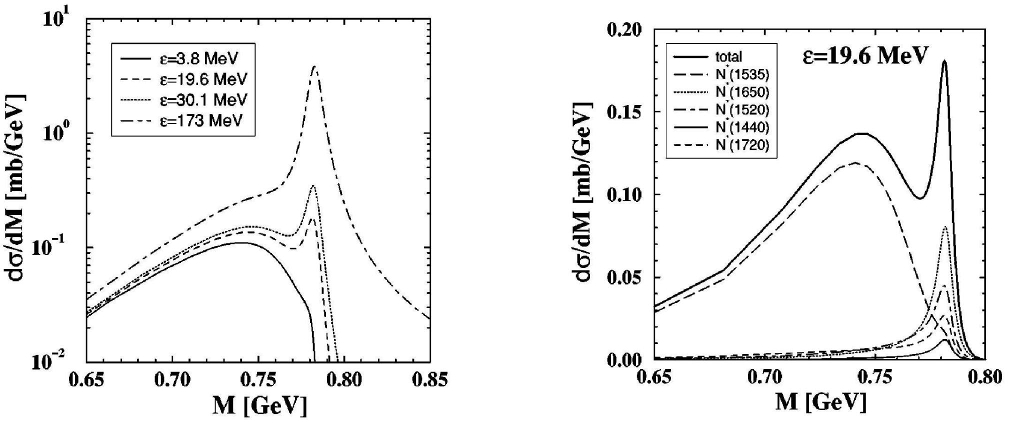

Figure 7.5: *The contribution of nucleon resonances (on- and off-shell) in ω meson production. Left: In the direct vicinity of the production threshold "off-shell" ω production dominates (solid line). With increasing excess energy a clear "on-shell" peak is visible, and the off-shell contribution slowly diminishes. The highest excess energy ($173\,MeV/c$) corresponds to a beam momentum of $3200\,MeV/c$ and can directly be compared with Fig. 7.8. Right: Decomposition of the missing-mass spectrum into the different contributions from nucleon resonances. The $N^\star(1535)$ dominates the off-shell production, while the other considered resonances mainly contribute to the "physical" ω meson production.*

The figures are taken from [Fuc03].

is indistinguishable from multi-pion reactions, since they fill an almost similar phase space[14]. The mass distribution of the ω meson (off- and on-shell) is described as follows:

$$\frac{d\sigma(s,M)^{pp\to pp\omega}}{dM^2} = \sum_R \int_{(m_p+M)^2}^{(\sqrt{s}-m_p)^2} d\mu^2 \, \frac{d\sigma(s,\mu)^{pp\to pR}}{d\mu^2} \, \frac{dB(\mu,M)^{R\to p\omega}}{dM^2}. \tag{7.3}$$

Here, μ and m_R are the running and the pole mass of the resonances, respectively; $\sqrt{s}$ is the invariant mass of the total system; $d\sigma(s,\mu)^{pp\to pR}$ is the cross section for the resonance production, which is governed by a phenomenological matrix element and phase space; and $dB(\mu,M)^{R\to p\omega}$ is the branching of each resonance to the ω decay mode. The sum in Eq. 7.3 runs over all considered nucleon resonances, while each addend is an integral over the kinematically allowed running mass (μ) of the resonance.

The resulting mass distribution is shown in Fig. 7.5. In the left picture the energy dependence is depicted, while in the right frame the contribution of each nucleon resonance to the total signal at a fixed excess energy ($\epsilon = 19.3\,MeV$) is show. Both pictures reveal a considerable contribution of off-shell ω mesons to the "theoretical background", i.e. in a mass region far away from the ω pole mass. This background

---

[14] In principle, dilepton spectroscopy could be used. If the off-shell ω production cross section is as large as predicted by this model, the number of dileptons produced in pp collisions should be significantly larger than the expectance from the on-shell ω total cross section alone. However, since the branching ratio to the dilepton channel is only $\mathcal{BR}_{e^+e^-} = 7 \times 10^{-5}$, the success of this task seems highly hypothetical.

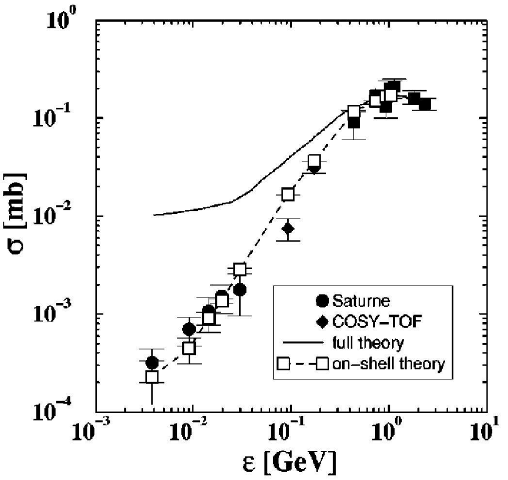

Figure 7.6: *Description of the $pp \to pp\omega$ cross section obtained in the resonance model. The solid curve shows the energy dependence of the cross section including both "on-shell" and "off-shell" ω production. The dashed line corresponds to the cross section where only the* detectable, *i.e. "on-shell", production is taken into account. Using the latter, the experimental data is perfectly reproduced within uncertainty limits.*

The figure is taken from [Fuc03].

contribution originates dominantly from the $N^*(1535)$ resonance. Confronted with the experimental results shown in Fig. 7.8, it is quite tempting to assume a correlation. However, the origin of the *experimental* background in Fig. 7.8 is not well known, as will be described later in this chapter (see 7.2.2).

Using this model, total cross sections are extracted analogously to experimental data: The signal and (theoretical) background, i.e. the on-shell and the off-shell ω production, are fitted by adequate functions, then the background is subtracted, and finally, the remaining signal function is integrated. Applying this method for different excess energies yields the energy dependence of the total cross section. As shown in Fig. 7.6, if only on-shell ω production is considered, the description of the experimental data is perfect within uncertainty limits.

7.2 Data Analysis

The reaction $pp \to pp\omega$ was examined with the COSY-TOF detector at a beamtime in January 2000. Two "runs" with beam momenta of $2950 MeV/c$ and $3200 MeV/c$ were performed, and the duration of each run was about one week. The main goal of this beamtime was the study of associated strangeness production, i.e. $pp \to pK^+\Lambda^0$ and $pp \to pK^0\Sigma^+$[Wag02][Kar04]. For ω-production, a trigger pattern aiming at four charged particles was written to tape in parallel. In order to minimize the influence on the main data taking, this trigger pattern was suppressed by a factor of 8 with respect to the main trigger. Due to this suppression, the integral amount of raw data for ω-production is equivalent to only *two days* of exclusive data collection, one day for each beam momentum.

7.2.1 Event Selection

The ω meson decays in the direct vicinity of the production vertex ($c\tau \approx 24 fm$). The prominent decay modes are either to two pions ($\mathcal{BR}_{\pi^+\pi^-} = 2.2\,\%$), to the charge-

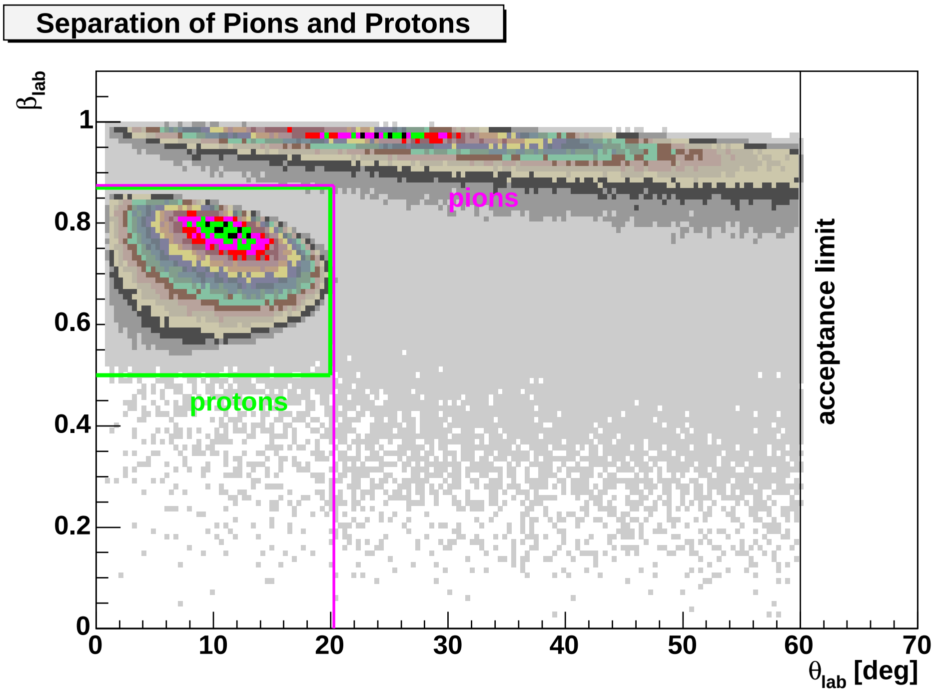

Figure 7.7: *The kinematical condition naturally separates protons from pions in the reaction $pp \to pp\omega$. Protons are constrained to angles smaller than $\vartheta \lessapprox 20°$ and a velocity of $\beta \lessapprox 0.9$. For over 90% of the pions the kinematical complement is true. The picture shows Monte-Carlo data for a beam momentum of $2950\,MeV/c$. For the higher beam momentum of $3200\,MeV/c$ an analogous situation is found; only the cut values have to be sightly shifted.*

neutral channel ($\mathcal{BR}_{\pi^0\gamma} = 8.5\,\%$), or, to three pions ($\pi^+\pi^-\pi^0$). The latter is the main decay mode with a branching ratio of $\mathcal{BR}_{\pi^+\pi^-\pi^0} = 88.8\,\%$. In the setup used, the TOF detector can only detect charged particles[15]. In addition, it has no direct means to differentiate between different species of charged particles: The only measured observables in a $pp \to pp\omega$ event are four track slopes ($4 \times (\vec{r_0} + \lambda\vec{r})$) and four velocities ($4 \times \beta$). Therefore, kinematical constraints have to be used to reconstruct (enhance) the desired event-pattern.

The analysis presented here aims at selecting ω mesons which decay into the main decay mode (three pions). The kinematical situation for this decay mode is illustrated in Fig. 7.7, where the protons and the pions show a completely different behavior in a "$\beta vs.\vartheta$"-plot: While the protons are constrained to angles below $\vartheta = 20°$ and velocities below $\beta = 0.9$, the pions are distributed over a wide angular range, mostly with very high velocities. Therefore, the strategy to enhance $pp \to pp\omega$ events is quite straightforward (as indicated by the cuts sketched in Fig. 7.7): (1) events with four charged tracks in the exit channel; (2) two tracks with $\vartheta < 20°$ and $\beta < 0.9$ ($\to$ protons) and two tracks within the kinematical complement ($\to$ pions)[16]. Applying

---

[15] The neutron detector was not used for this analysis and the calorimeter was not installed.

[16] To be precise ($\vartheta_{1,2}$=protons,$\vartheta_{\mathtt{a,b}}$=pions):

`if(` $(\vartheta_1 < 20$ `&&` $\beta_1 < 0.9$ `&&` $\vartheta_2 < 20$ `&&` $\beta_2 < 0.9$ `)`

these cuts on the measured data allows to "identify" the proton tracks. Assigning the proton masses to these tracks enables to calculate their four-momentum. Subtraction of both four-momenta from the four momentum of the entrance channel then yields the missing mass of the proton-proton system, hence the mass of the missing particle. The application of only these cuts already results in a clearly visible omega peak, although upon considerable background.

To improve the event selection additional cuts are required. Firstly, the product of both pion velocities has to be larger than 0.55 ($\beta_{\pi_1} \cdot \beta_{\pi_2} > 0.55$). This cut removes practically no signal, but slightly reduces the background. Secondly, only events with all four prongs within the angular range of $2^\circ < \vartheta < 60^\circ$ are allowed for analysis. This strongly improves the comparability of Monte-Carlo and detector data, since in this angular region their agreement is optimal. The final, and *very important*, cut is to allow only events with ω mesons emitted into the *forward* CMS hemisphere ($\cos(\vartheta_\omega) > 0$). Since the meson and the proton-proton system must be back-to-back in the CMS, for these events the proton-proton system is emitted into the *backward* CMS hemisphere. Due to the Lorentz boost of the CM the protons are found at forward angles in the laboratory frame, but with considerably smaller velocities compared to "forward hemisphere" protons. The smaller velocities, in return, considerably improve the momentum resolution of the protons. As in all proton-proton interactions, no (physical) information is lost by the restriction to one CMS hemisphere, since the entrance channel is symmetric.

The resulting distribution is shown for both beam momenta in Fig. 7.8. A peak at the pole mass ($782\,MeV/c^2$) resting upon a broad and structureless background is clearly visible. A quantitative discussion of the peaks, including acceptance, background, and uncertainty considerations will be presented later in this chapter.

7.2.2 Background

There have been many attempts to further reduce the background found in the experimental data. However, no cut combination leads to a cleaner picture: Background and signal were reduced by approximately the same factor, or the background was reduced only at small missing-mass values. Using Monte-Carlo, several background reactions ($pp \to \Delta\Delta$, $pp \to pp\pi\pi$, $pp \to pp\eta$, $pp \to pp\rho$) in several combinations were studied in detail. It turned out that the background distribution can be reproduced well by the use of the two-pion channel alone. However, this is only true for the cuts described above. If additional restrictions are applied in order to reduce the background, severe discrepancies between Monte-Carlo and experiment are found. Thus, the Monte-Carlo simulation can not be considered to mirror all processes involved.

The main reason for this unsatisfactory situation is the lack of particle identification at the TOF detector. The event selection is restricted to kinematical constraints only. In the case of ω production, this leads to a considerable amount of *combinatorial background*, i.e. four (arbitrary) particles are "identified" to be the protons and pions. All

---

```
        && ( (ϑ_a>20 && ϑ_b>20) || (ϑ_a<20 && β_a>0.9 && ϑ_b<20 && β_b>0.9 )
            || (ϑ_b>20 && ϑ_a<20 && β_a>0.9) || (ϑ_a>20 && ϑ_b<20 && β_b>0.9) ) ){/* continue */}
```

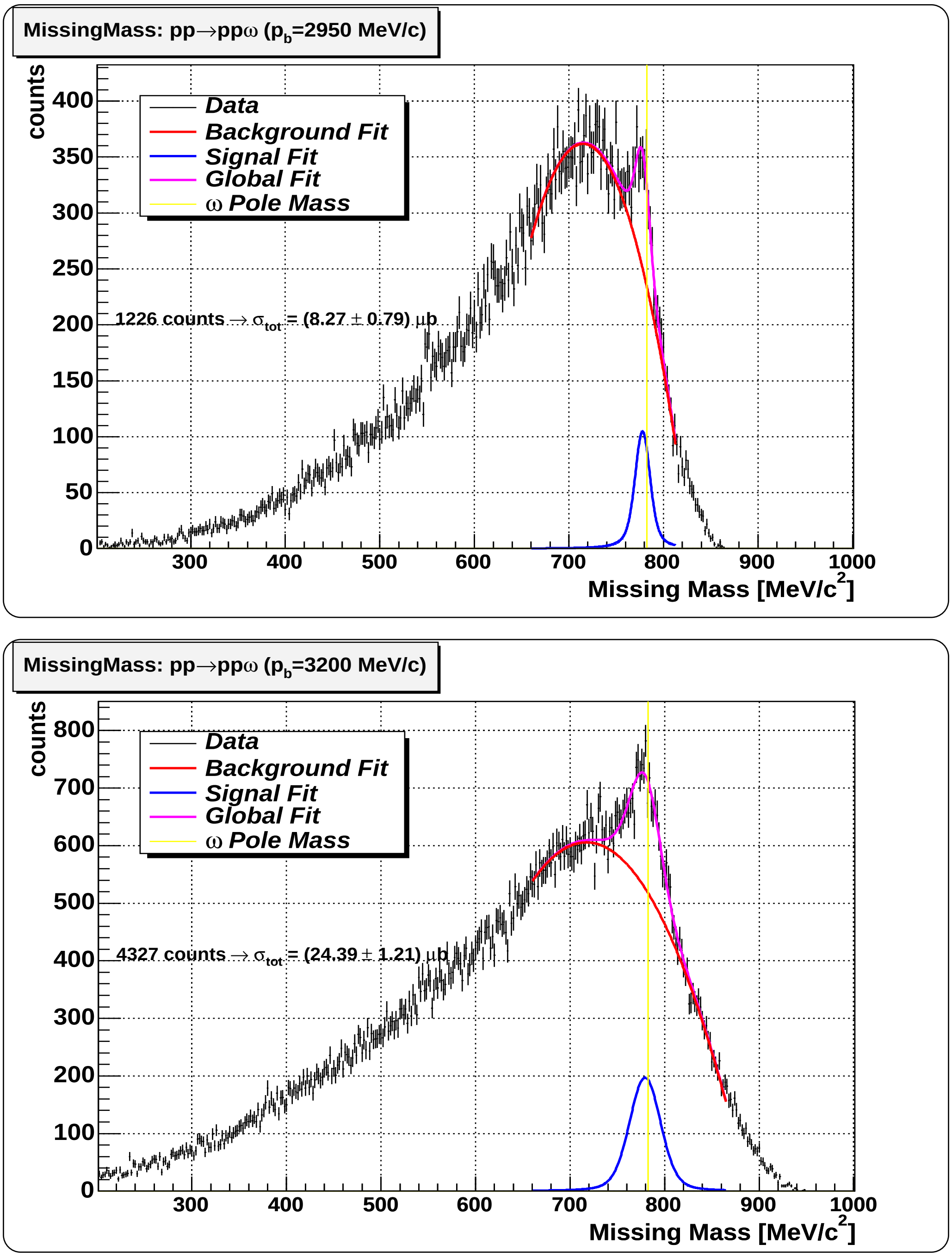

Figure 7.8: *Missing-mass reconstruction of the ω-meson. The background is fitted with a 2^{nd}-order polynomial, while the signal function is a convolution of a Gaussian and a Breit-Wigner. The width of the Breit-Wigner is fixed to the literature value, while the Gaussian width is taken from Monte-Carlo simulation and fine-tuned by maximizing the probability of the fit. The absolute strength of the signal function is a free parameter, and its statistical uncertainty determines the uncertainty of the fit. The pure signal-function is plotted as a blue line and reproduces the pole mass (yellow) well, within uncertainty limits.*

types of reactions decaying into (at least[17]) four charged particles add to this type of background, and a major contribution surely originates from *non-resonant multi-pion production*. This is, because (1) the total cross section is large (e.g. $\sigma_{pp\rightarrow pp\pi\pi} \approx 2\,mb$), and (2) up to seven pions can be produced at these high excess energies [Bri02]. However, it is difficult to account for all reactions decaying into (at least) four charged particles, especially since they have to enter the Monte-Carlo analysis with correct cross-section ratios and angular distributions. Finally, event mixing is very difficult to control using Monte-Carlo methods. Nevertheless, the background is distributed rather smoothly over the whole mass range. This makes it possible to use a polynomial to describe the background distribution and to evaluate the number of detected ω mesons by a simultaneous fit of this background function and an appropriate signal function. This will be discussed in more detail later in this chapter (7.2.4).

According to the resonance model described previously [Fuc03], the "background" could originate also from the ω-meson production itself: The $N^*(1535)$ contributes strongly to an off-shell production of ω mesons (see Fig. 7.5). These mesons never materialize outside the vertex, but they decay directly from the (on-shell) nucleon resonances. The exit channel, however, has the same signature as on-shell $pp \rightarrow pp\omega$ reactions, namely two protons and three pions. At least for (virtual) ω masses not too far off the pole mass, off-shell events will therefore have a high probability to pass all cuts applied. If this model is valid, it is simply *impossible* to separate the ω signal from the "theoretical background" with the means provided by the TOF detector. Probably only dilepton spectroscopy could reveal the contribution of off-shell ω mesons, since the kinematical information of both leptons could identify the ω meson in a cleaner ambient than hadronic decay products. However, this would require high-quality lepton-identification as well as an extremely good momentum resolution. This surely is not possible with a time-of-flight spectrometer. The very unfavorable branching ratio $\mathcal{B}_{\omega\rightarrow e^+e^-} \approx 7 \times 10^{-5}$ is an additional obstacle, so that this measurement will only be possible after the development of a new generation of detectors.

7.2.3 Acceptance Correction

The acceptance of the detector *and* of the analysis procedure is evaluated by means of Monte-Carlo simulation (see footnote on page 70). The package LasVegas (2.2.5) is used which is optimized for the TOF detector and simulates all dominant effects at the detector: Event generation, propagation of particles, secondary reactions, and triggering of detector signals (TDC/QDC conversions). The Monte-Carlo output is treated in the same manner as detector data (including calibration and data conversion). In analogy to elastic scattering, the acceptance of the detector/analysis system is determined for each observable by evaluating the ratio of the number of "input events" to the number of positively detected events. However, the reaction pattern is more complicated compared to the two-prong events discussed previously, since *five* ejectiles are found in the exit channel of $pp \rightarrow pp\omega$ ($\omega \rightarrow \pi^-\pi^0\pi^+$). In addition, only the *four* charged particles are detected (the π^0 remains unobserved). This circumstance complicates the determination of the acceptance, since different volumes of the

---

[17] In events with more than four charged particles some particles could remain undetected, thus leading to misidentified four-prong events.

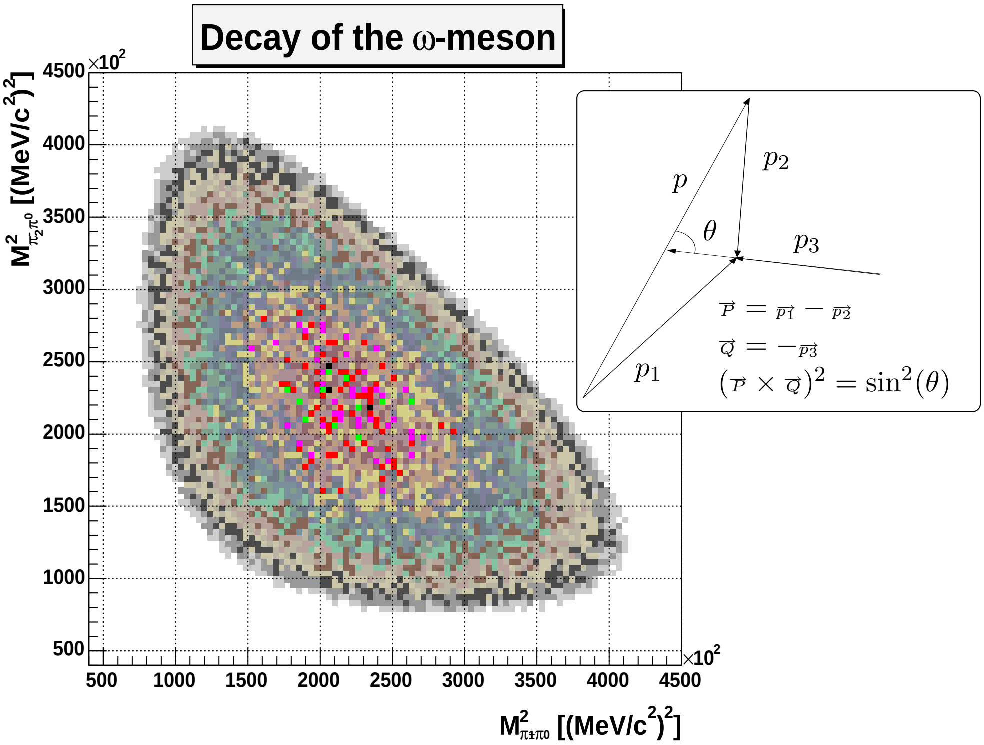

Figure 7.9: *Realistic decay of the ω-meson: As a $J^p = 1^-$ particle, the ω meson decays proportional to $(\overrightarrow{P} \times \overrightarrow{Q})^2 = \sin^2(\theta)$, where the definitions of the symbols are given in the upper right sketch. The resulting Dalitz plot shows an enhancement for "symmetric" events, i.e. where all three pions have similar momentum ("Mercedes-star").*

multi-dimensional phase-space have a different chance of being detected[18]. To ensure maximum agreement between the Monte-Carlo simulation and the data measured at the beamtime, two main effects are included in the simulation:

1. **The angular distribution of the ω with respect to the beam axis:** Since this distribution also is the measured observable, it is not (precisely) known beforehand. Therefore it is included iteratively: The measured distribution is parameterized and included into Monte-Carlo. The acceptance is determined and applied to the experimental data. This yields an improved angular distribution, which then is used as a new input to the Monte-Carlo simulation. The process converges after about three iteration loops.

2. **The intrinsic decay distribution of the ω meson:** Vector mesons are $J^p = 1^-$ particles, hence the distribution of the decay products is not isotropic according to phase space. They rather have an intrinsic decay distribution, which is shown in the Dalitz plot depicted in Fig. 7.9.

---

[18] Consider a (hypothetical) situation: One charged pion is predominantly emitted with high momentum into the backward hemisphere of the CMS. This pion would be found also in the backward hemisphere in the laboratory system, hence predominantly *outside* detector acceptance.

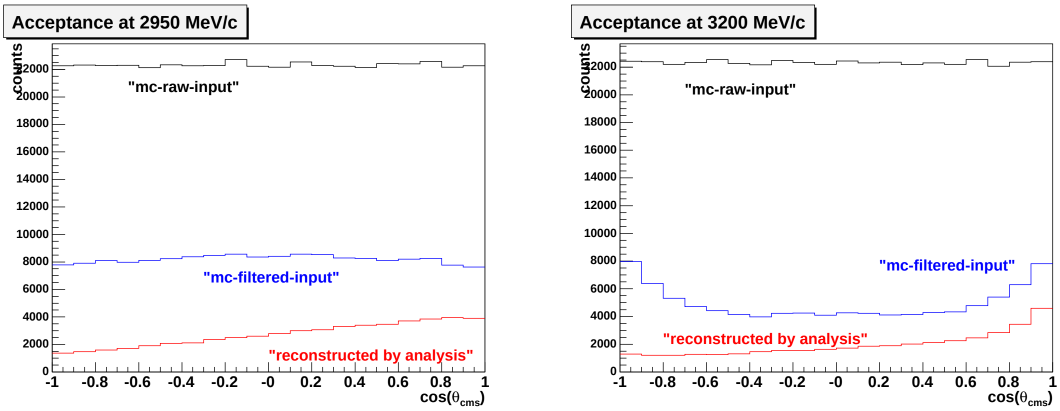

Figure 7.10: *Acceptance of the TOF detector and the TofRoot analysis for* $pp \rightarrow pp\omega$ *events plotted against the polar angle of the* ω *meson. The Monte-Carlo input (black) is filtered to emulate the angular distribution and the decay of the* ω *meson (blue). This data then is analyzed by the same software as experiment data. The output (red) are the actually detected events. Acceptance correction is applied bin-per-bin, where the scaling factor is simply the ratio* $r_{acc} = blue/red$.

In principle, both effects could be incorporated into the event generator. However, this would be a cumbersome approach, since every change would require both the generation of a new Monte-Carlo file and the full conversion into the CAL format. Therefore, the implementation of the angular distributions is carried out using a *filter*: A large file containing phase-space distributed events is prepared as input. For each event in this file a *probability* is calculated. This probability accounts for the angular distribution and the non-isotropic decay of the ω. Using this value, each event is tested (filtered) if it survives a (uniformly distributed) random number test[19]. The events which have passed the filter then are the actual input to analysis. From these events, the amount of detected ω mesons is deduced. The result of this analysis is shown in Fig. 7.10 for both energies; the isotropically distributed Monte-Carlo input, the filtered input, and the positively reconstructed events are shown as a function of the CMS angle of the ω meson. The acceptance is remarkably high and in the order of 50% for “forward hemisphere” ω mesons ($cos(\vartheta_\omega) > 0$).

Table 7.1 shows the contributions of the different cuts to the (loss of) acceptance. In addition, it shows the (estimated) contribution to the total uncertainty of the acceptance correction. This will be discussed in the following: Starting with a fixed number of Monte-Carlo events over 97% are successfully transformed into the final CAL format. The requirement for exactly four tracks then reduces the number of events by about 40%. This cut incorporates the data-loss due to *geometrical acceptance* and *detector efficiency*: If one of the particles is not detected, less than four tracks are found. In addition, this cut also removes events having *more* than four tracks due to cross talk or secondary particles[20]. These effects are difficult to control, and

---

[19] $p_{tot} = p_{cos(\vartheta)} \cdot p_{Dalitz}$, $p_{tot} \in [0, 1[$; $p_{test} \in [0, 1[$; $\texttt{if}(\texttt{p}_{\texttt{tot}} > \texttt{p}_{\texttt{test}})\{/ * \texttt{analysis} * /\}$

[20] The twin purifying method described in 4.5.1 is used; still about one percent of the tracks trigger a twin track.

Quantitative Evaluation of the Total Acceptance Using Monte-Carlo Methods			
Description	**Acceptance**	**Reduction**	**Uncertainty [%]**
Simulated $pp \to pp\omega$, $\omega \to \pi^+\pi^0\pi^-$	100.0 %	—	—
Survived calibration chain	97.4%	2.6%	1%
Exactly four tracks	59.6%	38.8%	5%
Found “protons” and “pions”	52.8%	11.4%	1%
No veto	52.8%	0.0%	3%
Both pions with $\vartheta < 60°$	41.2%	22.0%	0.5%
All tracks with $\vartheta > 2°$	40.7%	1.2%	0.5%
$\beta_{\pi_1} \cdot \beta_{\pi_2} > 0.55$	39.4%	3.2%	0.2%
ω emitted into forward hemisphere	25.4%	35.5%	0.5%
Total	25.4%	74.6%	6.1%

Table 7.1: *Quantitative analysis of the Monte-Carlo acceptance by observing the influence of the successively applied cuts (see text). The first column contains a brief description of the cut and the second the percentage of “survived” events. In the third column, the relative reduction with respect to this specific cut is given, and the last column shown the contribution to the overall uncertainty of the acceptance determination. The last row contains the final results. In the last column the uncertainties were added quadratically.*

in general lead to a relatively high contribution to the overall acceptance uncertainty. Starting from this data set, the proper mapping of the tracks to the two protons and pions works for about 90% of the events. The treatment of the veto cut has to be discussed in more detail: The influence of the veto is not measurable with Monte-Carlo; still the contribution to the total uncertainty is estimated to be 3%. This can be explained simply by the fact that the veto counters are not yet implemented in the Monte-Carlo framework LasVegas[21]. In addition, the Monte-Carlo simulation does not include the halo of the beam, the activation of the target region, other reactions creating “backward” particles which hit the veto, and event mixing. For experimental data, the overall reduction due to a veto count is about 6% (regarding the four-prong trigger). However, the experimental data is polluted by many other reactions, and especially multi-pion events have a higher probability to trigger the veto. Therefore, we assume that the actual ω signal is less affected by veto counts than the background, and a reduction of 3% seems reasonable. Due to the difficulty of comprehensively simulating the background and the absence of the veto in LasVegas, an uncertainty of (relative) 100% is estimated, thus the uncertainty is ±3% (absolute).

The next two cuts on the polar angles, on first sight, seem to have a huge effect. However, Monte-Carlo strongly overestimates the acceptance at angles above $\vartheta = 65°$. This cut therefore should be rather considered to ensure comparable results for Monte-Carlo and experimental data, hence can be considered to be geometrical acceptance. Finally about 39% pass all cuts, and about 25% of all $pp \to pp\omega$ events have a ω meson emitted into the “forward hemisphere”. Only these events are used for the missing-mass analysis, so that the (relative) acceptance in this angular region is of the order of 50% .

---

[21] The implementation is currently under construction.

7.2.4 Total Cross Section

The missing-mass distributions of signal and background after applying the cuts described previously are shown in Fig. 7.8. A ω peak is clearly visible for both incident beam momenta. To evaluate the total number of $pp \rightarrow pp\omega$ events, the spectra are fitted with a 2^{nd}-order polynomial added to a convolution of a Breit-Wigner and a Gaussian. All three parameters of the background function are free fit parameters. The convoluted signal function has as free parameters the absolute strength and the mean mass of the vector meson. The width of the Breit-Wigner is fixed to the width of the ω, as taken from the particle data group ($\Gamma = 8.4\,MeV$). The width of the Gaussian reflects the experimental resolution. It is roughly fixed by means of Monte-Carlo and fine-tuned by maximizing the probability of the overall fit. At least for the smaller energy the experimental resolution is in the order of the natural line width of the ω meson: $\sigma_{Gauss} \approx 6.5\,MeV$ and $\sigma_{Gauss} \approx 14.0\,MeV$ for the beam momenta of $2950\,MeV/c$ and $3200\,MeV/c$, respectively. The pure signal function is plotted in Fig. 7.8 in blue, and integration yields 1226 (4327) events for $2950\,MeV/c$ ($3200MeV/c$). In a naive approach, this would fix the statistical error to 2.8% and 1.5%, respectively. However, it is more appropriate to take the uncertainty of the integration, i.e. the uncertainty of the signal fit, to specify the uncertainty of the determination of the total counts. This is, since this value incorporates the contribution of the statistical fluctuations of the background as well. This procedure then yields an uncertainty of 9.6% for the smaller and 5.0% for the larger beam momentum.

The total cross section is then calculated applying the acceptance correction, considering the luminosity, correcting for the veto counter, multiplying the result by two (since only one hemisphere is observed), and taking the branching ratio[22] of the $\omega \rightarrow \pi^+\pi^-\pi^0$ channel into account. The statistical and systematic uncertainties are listed in Tab. 7.2. The overall uncertainty is dominated by the statistical uncertainty (fitting) and the acceptance correction. Provided that the influence of the veto detector will be determined with a higher accuracy, and that the statistical basis will be enlarged in further beamtimes, the total experimental uncertainties are expected to be reducible by about a factor of two, in the future.

Finally, the total cross section for $pp \rightarrow pp\omega$ can be given including the statistical and systematic uncertainty as $(8.27 \pm 0.80 \pm 0.58)\,\mu b$ and $(24.39 \pm 1.22 \pm 1.73)\,\mu b$ for $2950\,MeV/c$ and $3200\,MeV/c$, respectively. The results are summarized in Table 7.3.

7.2.5 Angular Distribution

The angular distribution of the ω meson with respect to the beam axis is of paramount importance to clarify the involved reaction mechanisms. Unfortunately, the signal-to-background ratio of $\approx 1{:}3$ is too poor to plot the angular distribution of the ω meson directly, as done for elastic scattering and $pp \rightarrow d\pi^+$. It is rather necessary to divide the spectrum shown in Fig. 7.8 into different bins in $\cos(\vartheta)$, and then to evaluate the total number of events in each individual spectrum. This process is illustrated for

---

[22] The contribution of the $\omega \rightarrow \pi^+\pi^-$ and $\omega \rightarrow \gamma\pi^0$ channel was determined via Monte-Carlo and is considered correctly.

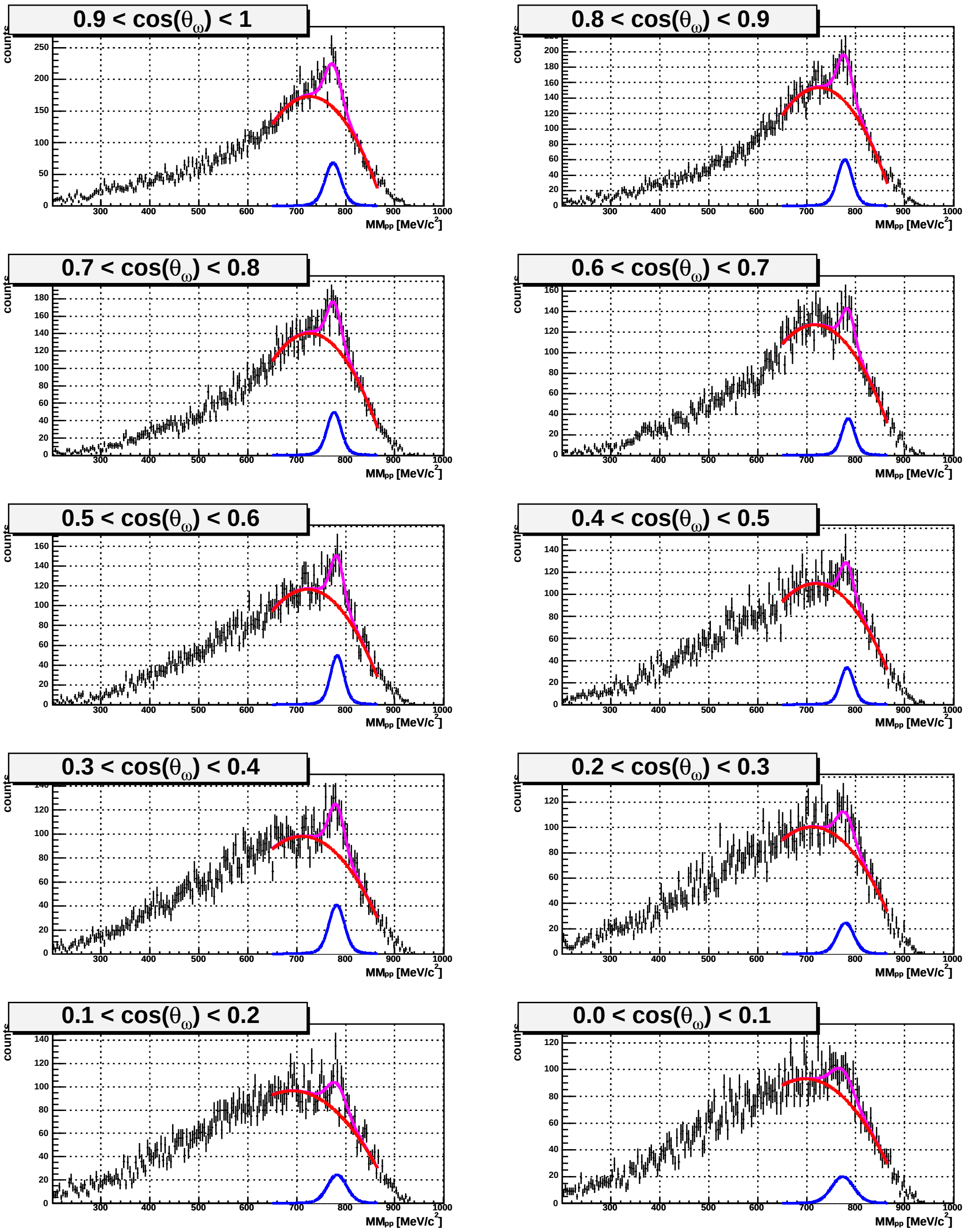

Figure 7.11: *The angular distribution is evaluated by filling missing-mass spectra for ten bins in* $\cos(\vartheta_\omega)$. *A fit-procedure similar to the one applied in Fig. 7.8 is applied. The ten signal functions are integrated and the retrieved number of counts are input for the angular distribution shown in Fig. 7.12.*

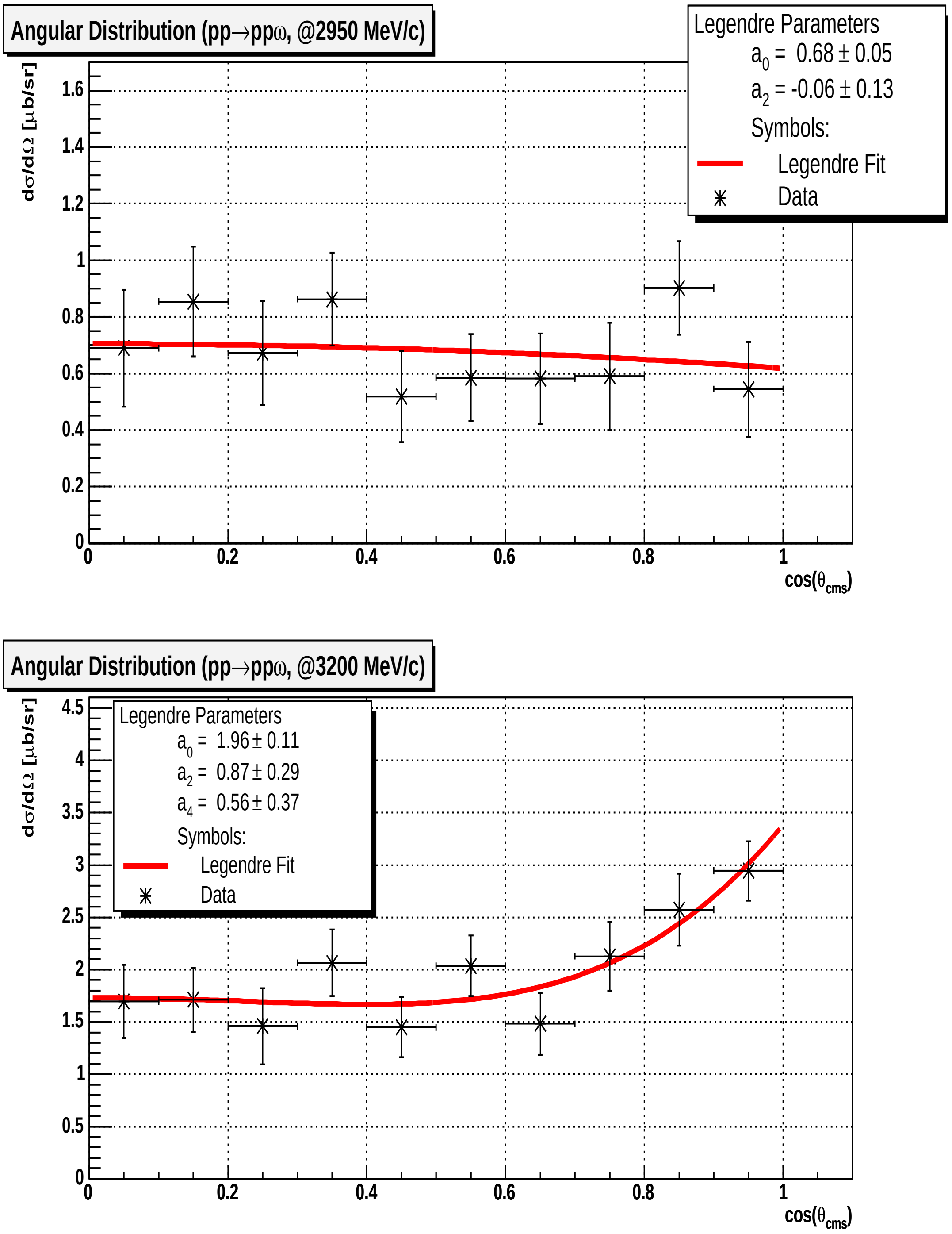

Figure 7.12: *Angular distribution of* $pp \rightarrow pp\omega$*: The number of entries is evaluated by ten independent fits (see Fig. 7.11). Acceptance and luminosity is applied as described in the text. While the distribution at the smaller energy is agrees fairly well with an isotropic behavior, is is strongly anisotropic for* $3200\,MeV/c$*. (The numerical values are summarized in Table B.1.)*

Summary of the Experimental Uncertainties		
Uncertainty	**2950 MeV/c**	**3200 MeV/c**
Acceptance Correction	6.1%	6.1%
Luminosity	3.8%	3.8%
Total (sys)	7.1%	7.1%
Fitting (stat)	9.6%	5.0%
Total (stat & sys)	12.0%	8.7%

Table 7.2: *Experimental uncertainties for the reaction $pp \rightarrow pp\omega$. The total uncertainty are calculated by adding the single contributions quadratically.*

$3200\,MeV/c$ in in Fig. 7.11 for ten bins in $\cos(\vartheta)$. The worsening of the experimental resolution towards $\cos(\vartheta) = 0$ is clearly visible. This is because the average velocities of the protons in the laboratory system increase, which limits the momentum resolution. In principle, values down to $\cos(\vartheta) = -0.2$ are extractable. However, the experimental uncertainty grows and the acceptance drops. Both effects lead to measurements of only a low significance; and since the entrance channel is symmetric, the analysis is restricted to “forward hemisphere” ω mesons only. Each individual fit was carried out in a similar manner as the determination of the total cross section: Monte-Carlo yields the width of the Gaussian for each bin. This width is scaled with the same factor determined by the fine-tuning procedure for the integral spectrum. Each signal function is integrated and yields a number of total counts. Acceptance is corrected for each bin using the ratio of input-to-output counts as shown in Fig. 7.10. Finally, the branching ratio is considered and the correction for the veto detector is applied. The obtained result for both energies is shown in Fig. 7.12. The uncertainties in “$\cos(\vartheta)$” are the bin size, while in “yield” they are taken from the individual uncertainties of the normalization factors (as provided by the fit). Into the same frame, a Legendre fit is plotted. While the smaller energy is in reasonable agreement with an isotropic distribution, the distribution at the higher beam momentum shows a strong anisotropy. Here, also the third even Legendre coefficient a_4 is needed to describe the data. The angular distributions and their implication on theory will be subject to the discussion section, later in this chapter.

Using the Angular Distribution to Calculate the Total Cross Section

As elaborated on page 88, the total cross section can be calculated alternatively from the Legendre fit of the angular distribution. For this, the leading coefficient a_0 simply has to be multiplied by 4π. In the present case, this results in values of $\sigma = (8.54 \pm 0.63)\,\mu b$ and $\sigma = (24.68 \pm 1.38)\,\mu b$ for the total cross section, respectively, where the uncertainties are calculated from the numerical error of a_0, i.e. from the output of the Legendre fit. The good agreement with the previously quoted total cross sections gives confidence into the methods used.

The results for the Legendre fit parameters and the total cross sections are summarized in Tab. 7.3.

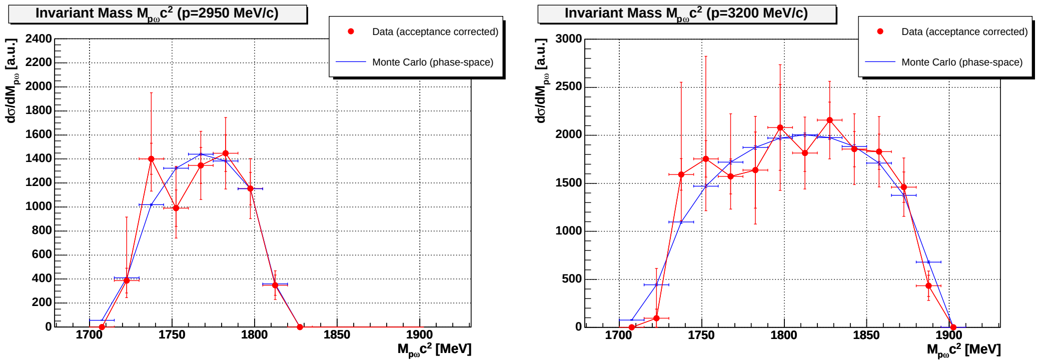

Figure 7.13: *The invariant-mass distribution of the $p\omega$ subsystem in the reaction $pp \rightarrow pp\omega$. The data (red) is acceptance corrected and compared to a phase-space distribution (blue). The phase space corresponds to a Monte-Carlo simulation* without *resonances, but including the angular distribution and the non-isotropic decay of the ω meson. The smaller error bars reflect the numerical uncertainty of the individual fits only, while for the larger bars the systematic uncertainty due to the fit procedure (range, width) are added. (The numerical values are summarized in Table B.2.)*

7.2.6 Invariant Mass Distribution

The invariant mass distribution of the $p\omega$-system is of high interest, since it could reveal $p\omega$ resonances. No resonances of this type have been observed experimentally so far, but their existence is suggested and predicted by several theoretical approaches.

The TOF detector measures two of the three primary reaction products with good momentum resolution, namely both protons. Since the entrance channel is known, the four-momentum of the ω meson can also be calculated. From this, the invariant mass of (both) proton-ω systems is evaluable. Analogous to the angular distribution, the background contribution prohibits to directly fill invariant mass spectra. Instead we have to follow the same approach as was used to determine the angular distribution, i.e. fill a missing-mass spectrum for different bins of the invariant mass. However, the situation here is worse, compared to the angular distribution: The shape of the background dramatically changes for different mass regions. This complicates a consistent and easy fitting procedure. Using Monte-Carlo, the widths of the signals have to be determined very thoroughly, and the fit intervals have to be chosen individually for each bin. This is a considerable source of systematic uncertainty. Nevertheless, it was possible to extract invariant mass spectra for both energies, which are plotted in Fig. 7.13. The smaller error-bars reflect the numerical uncertainty of each individual fit only. In order to determine the contribution of the systematic uncertainty, the boundary conditions of the fits (width of the signal, fit-range) were altered within reasonable limits. From this the size of the systematic uncertainty was estimated, and the resulting values are added to the pure numerical uncertainties in Fig. 7.13. Along with the experimental result a pure phase-space distribution is plotted (blue), which is scaled to equal the total yield of the experimental result. For a more detailed discussion of the distribution shown, please refer to 7.3.2.

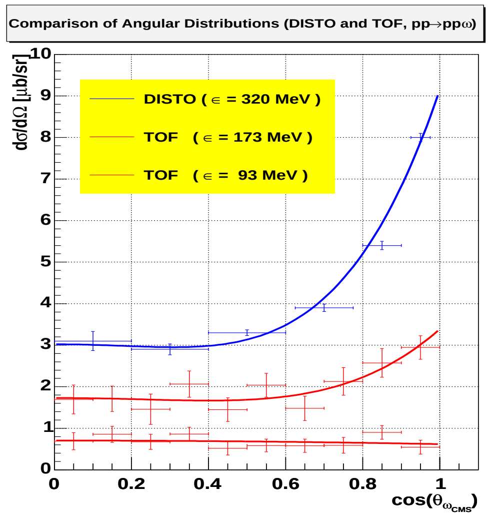

Figure 7.14: *Both measured angular distributions of this work in comparison with the data of DISTO [Bal01], where only statistical uncertainties are shown. The DISTO distribution corresponds to an excess energy of* $320\,MeV/c$. *The TOF data is identical to Fig. 7.12. While starting with a rather isotropical angular distribution, at larger excess energies higher partial waves start to contribute. The TOF data nicely fills the gap to the DISTO data. However, the energy dependency of the angular distribution distribution towards smaller excess energies still is unknown (see Fig. 7.16).*

During this work, the invariant mass distribution of the pp-system was evaluated as well, but the dependence of the background on the different pp-masses is even stronger than for the $p\omega$-system. It was not possible to determine the distribution within reasonable accuracy; the systematic uncertainties for all bins were higher than 50% of the deduced values. Therefore it was decided to not present them within this work. However, further development of the fit procedure is in progress.

7.3 Discussion

The experimental investigation of vector meson production in NN-interactions is a relatively new field of experimental nuclear physics. The available data is rather scarce, as was pointed out in the introduction to this chapter: The only published work covering ω production near threshold are currently [Bal98], [Hib99], [Bal01], [Bri01], and [Bri02]. From the theoretical point of view, ω-meson production is of particular interest; and theory eagerly awaits new experimental input. The results of this work for ω-meson production are summarized in Tab. 7.3.

In the following, firstly, the data presented in this chapter will be discussed with respect to the existing experimental data. Then, its implications for theoretical models will be sketched, after which, finally, a discussion on the “violation of the OZI-rule” will follow.

7.3.1 Comparison of the Results With Existing Data

The data presented here generally fit well into the so far available experimental picture. This was already shown in Fig. 7.2, where the total cross sections are plotted together with a compilation of the world data. The total cross section of this work is larger for $2950\,MeV/c$, but smaller for $3200\,MeV/c$ with respect to [Bri01]. This is an indication that no (large) systematic error affects the analysis. The angular distributions shown in Fig. 7.14 indicate a continuous behavior as a function of the excess energy: Starting

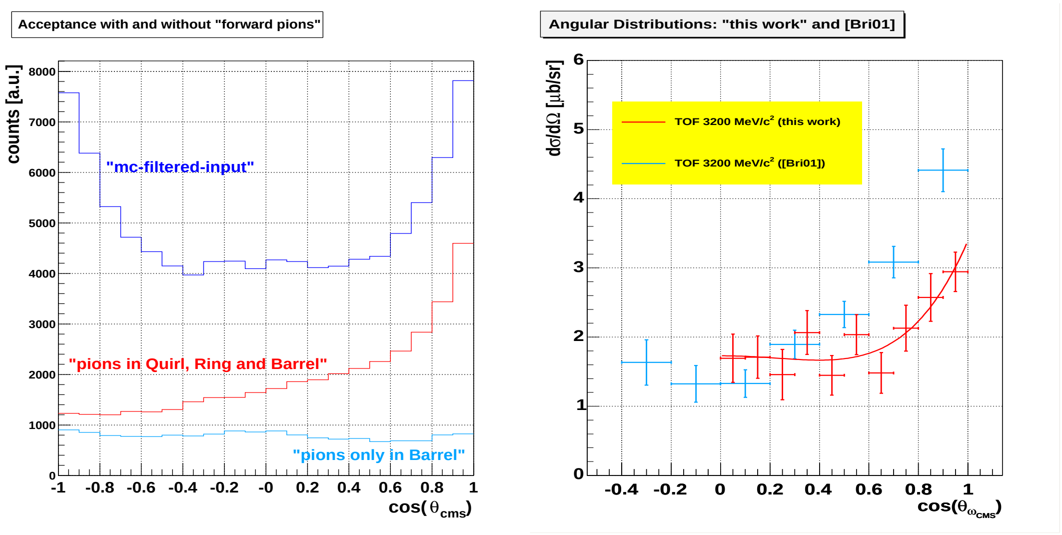

Figure 7.15: *Left: The acceptance is dramatically larger, when also pions with* $\vartheta < 25°$ *are used. Then the acceptance is rather constant* ($40\% - 55\%$)*. Without these pions, the acceptance dramatically decreases as a function of the* ω *CMS angle. Right: The measured angular distribution for* $3200\,MeV/c$ *in comparison with [Bri01].*

from an rather isotropic distribution, higher partial waves begin to contribute as excess energy increases.

However, compared with the results of [Bri01][Bri02], some differences occur. It has to be pointed out that both data agree within uncertainty limits. Nevertheless, an understanding of the *origin* of these differences is of crucial importance, since the raw-data used for analysis is identical. The fundamental difference of the analysis used for this work compared to [Bri01] is an *improved detector calibration*. As described in the first part, the analysis framework TofRoot enables a thorough and detailed calibration, which previously was not available. The use of TofRoot directly leads to an optimum time-of-flight calibration and to a high angular resolution of the detected tracks. In return, the better calibration rendered possible two main improvements for the data analysis of $pp \to pp\omega$:

1. In the previous analysis, the pion detection was restricted to larger angles, i.e. only pions in the Barrel were considered ($\vartheta > 25°$). As was shown in Fig. 7.7, the distinction between protons and pions can now be carried out also for pions below $\vartheta = 25°$.

2. The ω meson decays into three pions (π^-, π^+, π^0), but only the two charged pions are detected. Since this is a tree-body decay, the plane defined by the charged pions will (in general) not contain the momentum vector of the ω meson, i.e. they will be "non-coplanar". In the preceeding analysis, a cut on this "non-coplanarity" was necessary. This substantially reduced "two-pion" background (e.g. $pp \to pp\rho$, $\rho \to \pi^+\pi^-$), but affected the ω signal as well. This cut on the "non-coplanarity" is now omitted.

Both improvements have a large effect on the final analysis. Firstly, the number of detected ω events is roughly doubled, hence the statistical basis is enlarged. Secondly, the acceptance correction is much more straightforward. This point is very important, since both the total cross section and the angular distribution published in [Bri01] crucially depend on the acceptance correction[23]. As shown in Fig. 7.10, the acceptance of “this analysis” can be considered to be almost constant ($\approx 50\%$) for $cos(\vartheta_\omega) > 0$. The measured angular distribution without acceptance correction already describes the *slope* of the physical angular distribution (with an uncertainty of $\approx 15\%$). This was totally different in the previous analysis. At least one of the pions originating from an ω emitted into the forward hemisphere has a (very) high probability to be detected at small angles. Hence, the restriction of pions to the Barrel leads to a decreasing acceptance towards $cos(\vartheta_\omega) = 1$. This is depicted in Fig. 7.15 on the left, where, analogous to Fig. 7.10, the (filtered) Monte-Carlo input and the number of reconstructed events are plotted as a function of the CMS angle. The reconstructed events are shown *with* and *without*[24] pion detection at angles below $\vartheta = 25°$. Since the acceptance changes dramatically over the angular range, the acceptance correction in [Bri01] leads to a larger uncertainty of the angular distribution towards $cos(\vartheta_\omega) = 1$. A factor of two for the most outward bins is not excluded. In Fig. 7.15 on the right, the angular distribution of this work is shown in comparison to the distribution of [Bri01]. On first sight, a dramatic discrepancy appears. However, within the uncertainties discussed above, both distributions coincide.

The determination of the total cross section in [Bri01] is affected by the “measured” angular distribution as well. This is, since the measured distribution is used as input to the Monte-Carlo studies, which, in return, is used to determine the acceptance. The deduced acceptance, however, influences the final result of the angular distribution. If the acceptance correction “shifts” the outer bins near $cos(\vartheta_\omega) = 1$ to higher values, also the integral number of counts is overestimated. In fact, if the angular distribution is assumed to be isotropic to determine the acceptance correction, the total cross section drops from $30.8\,\mu b$ to $25.0\,\mu b$ [Bri02].

7.3.2 Implication of the Presented Data for Theory

In the following, the implication of the presented data for theory will be discussed. This will include all three measured observables: The total cross sections, the angular distributions, and the invariant-mass spectra.

Total Cross Section

The measured total cross sections fit well into the published data, so that we would not expect any larger impact on theory, on first sight. However, a closer look yields

---

[23] The acceptance correction adds to the total experimental uncertainty with 20%, but could be considerably higher for single bins of the angular distribution.

[24] The distribution for “pions only in Barrel” is *not* from [Bri01], but rather an emulation. The cut on the “non-coplanarity” described above is not applied, and the analysis is performed with TofRoot; still the overall picture is correct.

Observable	**2950 MeV/c**	**3200 MeV/c**
a_0 $[\mu b/sr]$	0.68 ± 0.05	1.96 ± 0.11
a_2 $[\mu b/sr]$	0.06 ± 0.13	0.87 ± 0.29
a_4 $[\mu b/sr]$	—	0.56 ± 0.37
σ_{tot} $(4\pi a_0)$ $[\mu b]$	$8.54 \pm 0.63 \pm 0.97$	$24.68 \pm 1.38 \pm 1.97$
σ_{tot} $(\Sigma\#)$ $[\mu b]$	$8.27 \pm 0.80 \pm 0.58$	$24.39 \pm 1.22 \pm 1.73$

Table 7.3: *Results for $pp \to pp\omega$: The Legendre parameters are taken from the fit shown in Fig. 7.12. The total cross section is calculated twice; (1) by multiplying the leading Legendre parameter (a_0) by 4π, and (2) by the total number of counts. For the first method the (statistical) uncertainty is taken from the variance of the fit parameter a_0, while for the latter it is determined by the uncertainty of the signal-fit. The systematic uncertainty is calculated for both methods using the values presented in Tab. 7.2.*

the contrary if we take also the experimental uncertainties into account: The measurements in the direct vicinity of the threshold have relatively large uncertainties due to threshold effects (beam momentum resolution, natural width of the ω, small cross sections); The DISTO point at $3670\,MeV/c$ has a large uncertainty ($\approx 26\%$), due to the normalization to the η production; and the accuracy of the measurements at even higher beam momenta is even worse. Therefore, the TOF-measurement of [Bri01] at $3200\,MeV/c$ often is used to "fix" the theoretical excitation function (see. Fig. 7.4). Since the value found here is about 25% smaller compared to that of [Bri01], this certainly will affect model calculations. In addition, doubt has been shed upon the size of the cross section published by DISTO, which, on the part of some theoreticians, is believed to be considerably too small [Sib03]. This assumption is not confirmed by the result presented here, so that this issue has to be studied in more detail now.

The cross section at $2950\,MeV/c$ is about 25% larger than the (central) value found in [Bri01]. Here, the deviation does not cause considerable difficulties, since at this energy the experimental uncertainty of [Bri01] completely covers the new value evaluated in this work.

Angular Distribution

The angular distributions presented here are of (relatively) small uncertainty, mainly due to the "constant and high" acceptance, as was previously discussed. Although within uncertainty limits at $3200\,MeV/c$, from the theoretical point of view some considerable differences to [Bri01] occur: The enhancement towards $\cos(\vartheta) = 1$ is less pronounced, but the anisotropy requires an a_4-term in the Legendre polynomial to satisfactorily describe the measured distribution. The angular distribution at $2950\,MeV/c$ is completely new. The statistical basis is inferior to the $3200\,MeV/c$ measurement, however, ten bins in $0 \leq \cos(\vartheta) \leq 1$ have been evaluated. The Legendre fit renders a contribution of $a_2 = -0.06 \pm 0.13$, which is perfectly compatible with zero. However, the result could be interpreted as a tendency towards a negative slope of the angular distribution; which is possible as well: The different contributing currents in [Tsu03] may result in either slope.

As described in 7.1.3, angular distributions are crucial input to the theory of [Tsu03]. The model parameters are fixed by a *simultaneous* fit to all available experimental data: All observables, at all energies, for all vector mesons (ρ, ω, ϕ). Using the new input, the parameters will be determined with a higher accuracy. From this, further constraints upon different reaction mechanisms may be established[25]. In this way, measurements in the $pp \rightarrow pp\omega$ channel may spur new theoretical results not only for ω production but also for all other vector meson channels. The outcome of this procedure is difficult to predict from an experimentalist's point of view. However, this model seems to provide some predictive power: The *description* of the data available before this work already showed the *prediction* of the "cooking-pot like" behavior of the angular distribution at $3200\,MeV/c$ (see Fig. 7.4). Our group is in close contact with the authors of [Tsu03], hence the new experimental input will soon lead to new model calculations.

Invariant Mass Distribution

Theory yearns for invariant mass distributions, since the existence of $N\omega$ resonances is a totally open question. As was sketched in the introductory part of this chapter, many predictions for those resonances are found in the literature. Their existence is incorporated in "secondary theory", i.e. into models *using* the existence of $N\omega$ resonances to describe more complex phenomena (e.g. dense matter, neutron stars). Unfortunately, the experimental findings presented in Fig. 7.13 do not allow a conclusive answer. Within uncertainty limits the measured distributions are in agreement with phase space[26]. However, with some imagination, a tempting "bump" at small invariant $p\omega$ masses seems to be apparent[27]. This behavior could stem from a $p\omega$-resonance at $\approx 1740\,MeV/c^2$, where the relatively sharp "signal" in the spectrum for $2950\,MeV/c$ would then be broadened at the larger beam momentum ($\approx \times 2$, due to decreasing experimental resolution). An other explanation could be a contribution of the $N^*(1710)$, which, due to its large width, would populate the lower mass region. However, the weak "signal" at $m_{p\omega} \approx 1740$ could completely results from systematic uncertainty as well: Due to the changing shape of the background, a considerable systematic uncertainty adds to each individual bin. The size of these systematic uncertainties varies, i.e. while it is "small" and in the order of the numerical uncertainty of each individual fit at medium and high $p\omega$-masses, it reaches values up to 50% of the total signal near the lower mass boundary[28]. The result is therefore in agreement with an phase-space like behavior of the $p\omega$-system, as well as with an considerable enhancement at small masses.

---

[25] Currently four different parameter sets describe the ϕ production.

[26] The final-state-interaction (FSI) is not visible in these distributions, since it only effects the reaction products on scales of the order of a few MeV/c^2. This is not resolvable in Fig. 7.13, as the bin-size is $15\,MeV/c^2$.

[27] Especially, if we consider that the "phase-space distribution" is scaled to equal the total amount of counts of the experimental distribution. If an enhancements exists, the Monte-Carlo result would have to be "smaller", hence still reproducing the distribution at medium and large masses, but showing a larger enhancement at the lower mass boundary.

[28] In this region the uncertainty is strongly asymmetric, i.e. it is larger for higher differential cross sections.

On the other hand, an experimental result should be reproduced by theory, i.e. with or without an incorporation of an $N\omega$ resonances at $m_{p\omega} \approx 1740$ and with or without a contribution of the $N^*(1710)$ resonance, the proposed models should be capable to reproduce the *measured* distribution within the experimental resolution. So far no predictions upon invariant mass spectra exist for proton-proton induced ω production; and considering that various nucleon resonances (which add constructively and destructively) are incorporated in both models of [Tsu03] and [Fuc03], it is a priori not clear, if these models can fulfill this task. In this sense, also this "weak" measurement could distinguish between different theoretical models.

7.3.3 Violation of the OZI-rule - Strangeness Content of the Nucleon

As sketched during the introductory section of this chapter, the ω/ϕ-production may provide a unique tool for establishing the strangeness content of the nucleon wavefunction (see 7.1.1). In the most naive picture, the presence of strangeness can be measured by the deviation of $\mathcal{R}_{\phi/\omega}$ (Eq. 7.1) from the value predicted by SU(3), i.e. from a comparison of the total cross sections for ϕ and ω production at an equivalent excess energy. Recently, $\sigma_{pp\to pp\phi}$ was measured for an excess energy of $83\,MeV$ at DISTO [Bal01]. The experimental value for the total cross section is $\sigma_{pp\to pp\phi} = (190 \pm 14 \pm 80)\,nb$. The uncertainty of this cross section is huge, due to the normalization to the not well known $pp \to pp\eta$ cross section and poor count rate. The same experiment measured also the ω cross section, but due to the smaller ω mass, at a higher excess energy of $320\,MeV$. A model-based extrapolation over almost an order of magnitude in cross section had to be applied in order to calculate the ω cross section at $83\,MeV$. As a result, $\mathcal{R}_{\phi/\omega}$ is determined to be 2.3×10^{-2}, which is about five times larger than the predicted value according to SU(3). Since the model dependence of this extrapolation introduces a considerable uncertainty, measurements near $\epsilon = 83\,MeV$ were strongly desired. TOF [Bri02] has measured the total cross section at $\epsilon = 93\,MeV$ which is quite close to the excess energy of DISTO's ϕ-production; a $\mathcal{R}_{\phi/\omega}$ violation by a factor of ≈ 7 was found.

The value for $\sigma_{pp\to pp\omega}$ found in this work is $8.27 \pm 0.79\mu b$, but (as in [Bri02]) at an excess energy of $93\,MeV$. To adjust the measured cross section to $\epsilon = 83\,MeV$ (which corresponds to a beam momentum of $2920\,MeV/c$), we can use a parameterization of the Sibirtsev model [Sib96]

$$\sigma_{pp\to pp\omega} = a(1 - \frac{s_0}{s})^b (\frac{s_0}{s})^c \tag{7.4}$$

where s is the squared invariant mass of the total system and s_0 the squared invariant mass at the reaction threshold. The parameters b and c are taken from [Sib96] ($b = 2.3, c = 2.4$) and $s_0 = 7.06\,GeV^2$ is fixed by the masses of the exit channel. The parameter $a = 4.9$ is fixed to reproduce the measured cross section at $\epsilon = 93\,MeV$[29] (original value $a = 5.7$). Using $s = 7.52\,GeV^2$ (s@$83\,MeV$) in Eq. 7.4 yields a total cross section of $6.7\,\mu b$, which, according to Eq. 7.1, leads to the experimental value

---

[29] Using the same parameter set, the total cross section at $3200\,MeV/c$ is calculated to be $26.9\,\mu b$. This deviates from the measured value only by $\approx 11\%$, and gives confidence to this analysis as well as to the parameterization used.

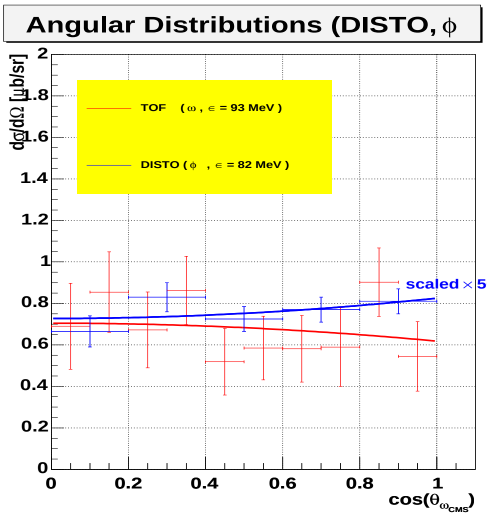

Figure 7.16: *Comparison of angular distributions: $pp \rightarrow pp\omega$ (this work) and $pp \rightarrow pp\phi$ (DISTO [Bal01]). The DISTO data reflects the statistical uncertainties only, and the data is scaled by a factor of 50. The difference in excess energy should be negligible for the angular distribution. A different behavior of both reactions is visible, although both distributions are in agreement with an isotropical distribution within uncertainty limits. Further measurements on* both *reactions are strongly desired, since similar angular distributions are needed as prerequisite for the $\mathcal{R}_{\phi/\omega}$ argument (strangeness content of the nucleon).*

$\mathcal{R}_{\phi/\omega} = 2.8 \times 10^{-2}$. The uncertainty of this value is large (about a factor of 2), mainly due to the large uncertainty of $\sigma_{pp \rightarrow pp\phi}$. Dividing the found value by the SU(3) prediction (4.2×10^{-3}) and considering an uncertainty of a factor of two then yields a “violation of the OZI-rule by a factor of $6.7^{+6.7}_{-3.4}$. This is slightly larger than the DISTO result. Although the uncertainty is large, it is a strong indication that the (naive) SU(3) prediction is wrong.

Compared to the experimental uncertainties of the ϕ-meson measurement, the total cross section of the ω can be considered to be exactly measured. Therefore, a reduction of the large uncertainty of $\mathcal{R}_{\phi/\omega}$ will only be obtained when new data for the ϕ production will be available[30].

Comments on the $\mathcal{R}_{\phi/\omega}$-Argument (I): Reaction Processes

A significant deviation of the $\mathcal{R}_{\phi/\omega}$ value from the SU(3) prediction can be explained by an intrinsic strange-quark content of the nucleon. However, with experimental and theoretical knowledge of today, it will not *confirm* the $s\bar{s}$-presence in nucleons! It only indicates that “something” is not yet understood. The available theoretical models describing this “violation” of the OZI-rule reach from a sizable $s\bar{s}$ content with fixed polarization and well-defined quantum numbers [Ell00] to models not needing $s\bar{s}$-admixture at all [Tit00]. In the latter case, doubt arises on the $\mathcal{R}_{\phi/\omega}$-argument, since it is only valid in case of *comparable production processes*: For example, if the vector meson production is a sum of two coherent amplitudes, but of *different* relative strength with respect to each reaction channel (which may be also energy dependent), then arbitrary $\mathcal{R}_{\phi/\omega}$ values can evolve - not violating the OZI-rule at all.

To clarify this issue, the $\mathcal{R}_{\phi/\omega}$-quotient has to be measured starting at threshold up to excess energies of $\approx 200 MeV$. In addition, the *reaction dynamics* have to be

---

[30] The ANKE collaboration (at COSY) is currently planning a program for ϕ-meson production near threshold [ANKE02]

examined, i.e. the contributing processes have to be understood by theory. Only then, the assumption of comparable reaction-processes in ϕ/ω-production can be validated. A first test of this assumption is now possible with the angular distribution elaborated in this work. As is shown in Fig. 7.16 and discussed previously, the angular distributions of ϕ and ω mesons are both isotropic at $\epsilon \approx 90\,MeV/c$ within experimental uncertainty. However, as much as the ϕ tends to have an increased differential cross section at $\cos(\vartheta) = 1$, the ω tends to smaller values. If this trend is confirmed in the future, the $s\bar{s}$-content of the nucleon can not be established by the use of Eq. 7.1, at least not without further model-dependent assumptions. On the other hand, if both distributions not only "converge" for $\epsilon = 83\,MeV$, but will show similar angular distributions over a broad energy range, then this would be a strong indication for intrinsic strangeness in the nucleon wave function.

Comments on the $\mathcal{R}_{\phi/\omega}$-Argument (II): Nucleon Resonances

A very interesting comment on the $\mathcal{R}_{\phi/\omega}$-argument arises from the model of C. Fuchs [Fuc03], discussed in 7.1.3: The ω meson decays into three (light) pions. The sum of the masses of the decay products ($\pi^+\pi^0\pi^-$) is well below the ω pole mass ($414\,MeV/c^2 < 782\,MeV/c^2$). Hence the available phase-space is large, allowing a sizable contribution of *off-shell* ω production. This is *not* true for the ϕ meson, which dominantly decays into the $K\overline{K}$ mode. Since the masses of the initial and final state are almost alike ($987\,MeV/c^2 \approx 1020\,MeV/c^2$), off-shell ϕ production is (strongly) limited by energy conservation. If we decide to count off-shell *and* on-shell ω mesons for the calculation of $\mathcal{R}_{\phi/\omega}$, then the deviation from the OZI-prediction may vanish, i.e. the "violation of the OZI-rule" experimentally observed today would be explained simply by the neglect of the off-shell ω-meson production.

A clarification of this issue is difficult experimentally, since off-shell mesons are un-measurable at present. In addition, the considered nucleon resonances are not accessible in an invariant mass distribution of the $p\omega$-system, since their masses are smaller compared to to $m_p + m_\omega$ (except for the $N^*(1720)$). However, theoretical work is not limited by experimental means. A further development of Fuchs' model may lead to a "precise" theoretical description of vector meson production, which then may finally bring the experimental and the SU(3) value of $\mathcal{R}_{\phi/\omega}$ in accordance. In this regard, a prediction of differential observables in [Fuc03] would surely help to establish the validity of the nuclear-resonance model.

Chapter 8

Summary and Outlook

The time-of-flight spectrometer TOF stands out for its experimental versatility. It is fed by the COSY accelerator that provides a high-luminosity (polarized) proton beam in a momentum range reaching up to $3680\,MeV/c$. Due to the large solid angle coverage of TOF in the laboratory frame ($\approx 2\pi$), the measurement of a broad variety of nuclear reactions is possible. On the one hand, this variety is very desired from the experimenter's point of view, but on the other hand, it leads to a specific difficulty, namely how to efficiently analyze the data, if a large variety of reactions in different setups and at different beam momenta are to be investigated.

The scope of this work was twofold: (1) a detailed description of the new analysis framework TofRoot, which was implemented considering the requirements of the TOF detector in particular, but also the needs of nuclear physics in general; and (2) the experimental results for three different nuclear reactions: Elastic scattering, $pp \to d\pi^+$, and the vector meson production $pp \to pp\omega$ (all for two different beam momenta).

The Analysis Framework TofRoot

The analysis framework TofRoot was developed to aid the TOF collaboration in offline analysis. The fundamental basis of TofRoot is ROOT, which is *the* analysis framework today. The main pillar of TofRoot is a set of *concepts* and *aims*, which were defined *prior* to the implementation. The most important concept of TofRoot is to *enforce* teamwork, in a sense that each contributing individual is encouraged and constrained to contribute to an integral effort. Using this guiding idea, a rapid growth of the system could be ensured and led to the implementation of a complete calibration and conversion software "from scratch". Another concept of TofRoot is *standardization*: All files of all beamtimes have the same *fixed file-format*, to each beamtime (exactly) *one* calibration database is provided (`TofCal`), and the final analysis is performed using the same loop class (`TofAna`) and a standardized track class (`TofTrackParticle`). Nonetheless, also *flexibility* is supported as the file format and the database are capable of being used for any beamtime, and the loop and the track class are *automatically* adjusted to the specific needs and setups of different beamtimes. After (semi-) automatic calibration and conversion, the data files are "ready to use", i.e. the physical information ($\beta, \gamma, \vartheta, \varphi, p, E, ...$) is directly accessible. This enables the implementation of *generic* analysis algorithms, which immediately can be reused for the data of other beamtimes. This concept of *generic programming* is crucial for the COSY-TOF detector, since the hardware setup is frequently changed. In fact, due to extensive reuse of already implemented code, an *online monitor* was rapidly developed that enables to monitor *physical observables* as the time-of-flight in real-time.

So far, one beamtime (January 2000) has been analyzed in detail, but the analysis of additional three beamtimes is ongoing and shows first results. The TofRoot project will be continued in the future, as new detectors will be added and further calibration algorithms will be implemented.

Meson Production in Proton-Proton Collisions

The analysis of data taken with the TOF detector during a beamtime in January 2000 was the subject of the second part of this work. Three different reactions were studied for two incident beam momenta ($2950\,MeV/c, 3200\,MeV/c$). Firstly, the elastic scattering was prepared with a completely new selection criterion, which yielded a virtually background-free signal. From this, the (integral) luminosity could be determined with high precision. Precise knowledge of the luminosity is crucially needed for the quantitative analysis of other reaction channels. The angular resolution and the extraction efficiency is comparable to state-of-the-art experiments specialized on elastic scattering. This is an impressive result for a multi-purpose detector.

Secondly, the same selection criterion was used to obtain total and differential observables of the reaction $pp \to d\pi^+$. Here, the available world data is rather scarce for the beam momenta used. As in elastic scattering, the results obtained can compete with the published data with respect to systematic accuracy. The output is only limited by the statistical significance, since this reaction was unfavored by the trigger setting. In future beamtimes this trigger setting will be adjusted, so that TOF certainly will provide trustworthy data for this reaction channel.

Finally, the most important reaction covered in this work is the vector meson production in nucleon-nucleon interactions ($pp \to pp\omega$), which has recently attracted considerable interest on the part of both experimental and theoretical physics. However, the elementary production processes are also of crucial importance for many other fields of physics today (cosmology, dense matter, nucleon structure). This is, because numerous theoretical models crucially depend on vector meson properties in *nucleon-nucleon* interactions, but many of these properties are simply unknown. Exploiting the good detector calibration provided by TofRoot, a clear ω signal was prepared, which resides upon a continuous background. Total as well as differential cross sections have been extracted from this, some of which are completely new to the word data set. The results are generally in good agreement with theory and previous experiments, however some peculiarities arise: The total cross section at the higher beam momentum is found to be $\approx 25\%$ smaller than previous experimental findings; the angular distribution of the ω meson shows a smaller degree of anisotropy than in a preceeding analysis, but now the third even Legendre coefficient (a_4) must be included to adequately reproduce the measured distribution; although in agreement with an isotropic distribution, the angular distribution at the smaller energy shows a (slight) maximum at $\cos(\vartheta) = 0$; the invariant mass spectra of the $p\omega$-system are in agreement with a distribution according to phase-space, however, it may indicate a resonant intermediate state coupling to the $p\omega$-channel near the lower boundary of the invariant mass.

The experimental results presented in this work are of substantial importance to theory, since they extend the data basis to formerly unknown regions. Especially the differential observables presented in this work are both an important experimental input to and a further test of the existing theoretical models.

However, further experimental input to theory is badly needed for the relatively new field of vector meson production in NN collisions. This input will be provided by TOF in the near future, since the analysis of data collected in an additional beamtime is ongoing, and a beamtime - especially set up for ω production - is scheduled for easter 2004. At this beamtime it is planned to utilize a polarized beam, hence spin observables will be accessible as well. In combination with an increase in luminosity by a factor of 50, the data is expected to be of high statistical significance. From this, further insight into the reaction dynamics of ω meson production in pp collisions will certainly be obtained.

Appendix A

Dresden **O**nline **M**onitor (**DOM**)

With the recent replacement of the DAQ[1] system (from TDAS [Schoe97] to EMS [EMS]), COSY-TOF lacked online monitoring. A new online monitor was implemented using the TofRoot framework, where strong emphasis was put on reusing previous developments. The main control histograms ("standard histograms") and the file-format are the same as is used for the RAW file format, and the GUI[2] is virtually the same as the "normal" viewing tool for RAW files. Also the software (source-file) layout, with a separation between the "user" and the "developer" section is strongly reminiscent of `TofAna`. Through this efficient modus operandi, the developing time for the whole online system was less then six weeks. Still, the development is no intermediate workaround, but a fully operational online-monitoring system. The DOM has been used in three beam-times in 2002, and has proven to be stable and convenient.

The monitoring system is separated into three main parts (Server, Client, GUI) which will be discussed in the following. A schematic view of the DOM is shown in Fig. A.1.

The Server

The online data (DAQ) is read via the net using the standard Linux command `netcat` . It then is converted, without data loss, by the Jülich program `ems2tade`[3]. The output of `ems2tade` is piped into the online-server. The online-server is a compiled program which is basically the same as the standard program which creates RAW-format files (`tape2raw`) in TofRoot. It also incorporates the same "standard histograms" (all TDC/QDC channels, correlations). The main difference is that it stores the histograms in a memory mapped file (`TMap`), which has the capability to allow read *and* write operations at the same time. The main code of the online-server is "official", i.e. it can not be edited by a normal user. Editable are only three files (UserHistoDefs, UserInitHistos, UserFillHistos), which are intended to declare, define, and fill histograms. After any change, the server has to be stopped, recompiled, and restarted to let these changes take effect. However, in combination with the client, compilation-

---

[1] **D**ata **A**c**Q**uisition

[2] **G**raphical **U**ser **I**nterface

[3] Convert EMS data to: **T**DC, **A**DC, sub-**D**etector number, **E**vent number.

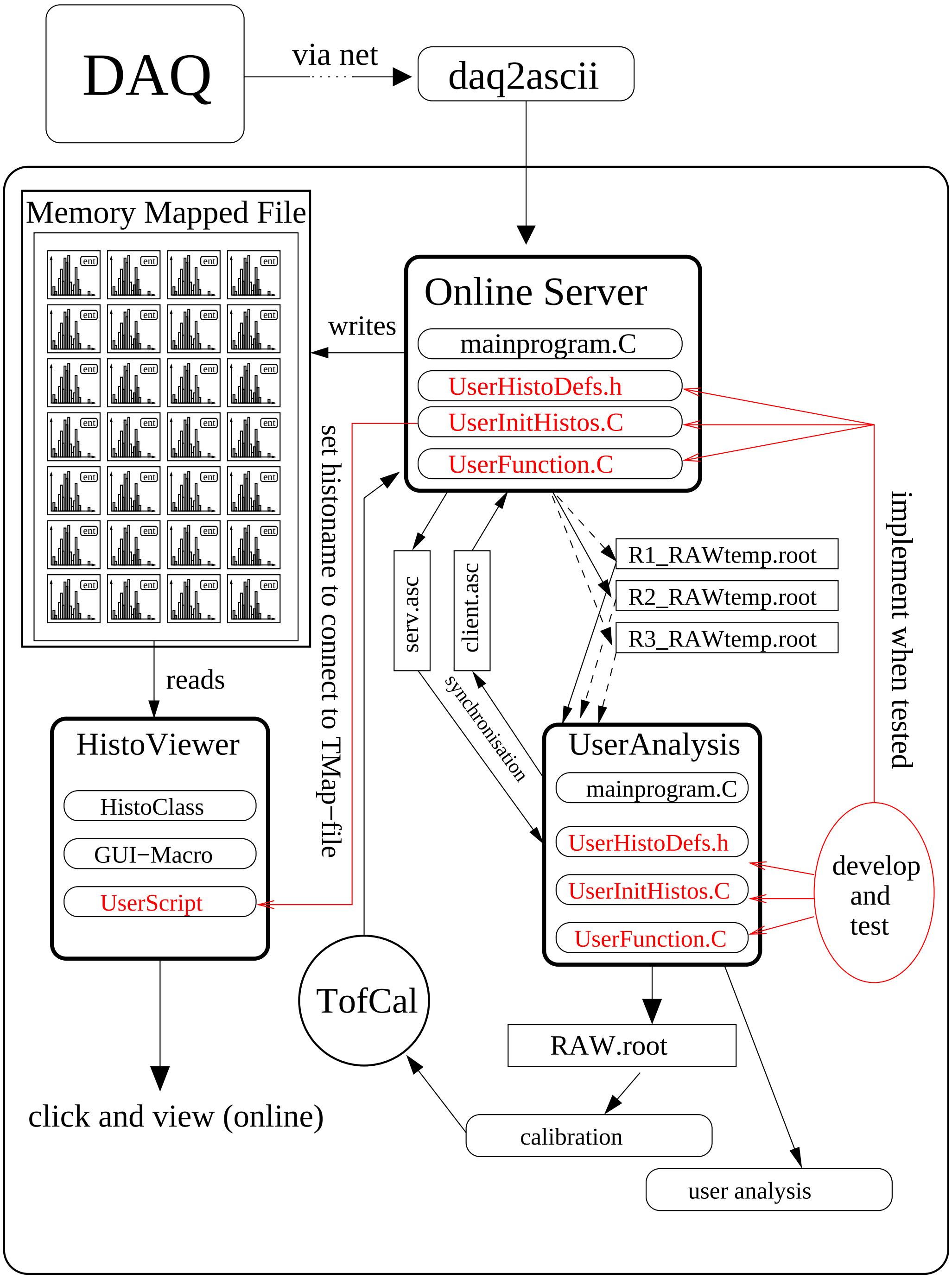

Figure A.1: *The DOM serves for monitoring the standard histograms. In addition, the user has the possibility to add histograms and interactively view them using the histogram viewer. For further studies, or for testing code before adding it to the server, the client supports the user by constantly looping over intermediate files. The sections where the user can intervene are plotted in red.*

and runtime-errors are few. This will be discussed in the next section.

The Client

While the online server fills the memory mapped file, it, in addition, cyclically writes real data (RAW) to small temporary files on hard disk. These files are input to the client program (`UserAnalysis`). The client reads these files, always taking the most recently closed file. The synchronization is thereby guaranteed by simple ASCII-files.

One advantage of this server-client modus is that the layout of the server and the client programs are identical, i.e. both provide the same user-functions, as indicated in Fig. A.1. In addition, all global variables, constants and pointers are identical. This offers the possibility that the user can test procedures that are foreseen to be implemented to the server code *prior* to actually adding it into the server program. Only after the functions have proven to be stable and useful, they will be promoted to the server program. This reduces the failing-time/recompile-cycles of the server program appreciably.

Another important feature of the client is that it can create an (eventually large) RAW-file on hard disk, while always reading the most recent data. At any time, files for further analysis can be generated quickly without having to await the classical “write-a-tape, eject, read-a-tape” cycle. This is extraordinarily important while setting up the experiment, where the whole system is not yet in a stable condition and flexibility is required. During the beam-times of December 2002 this was successfully proven. Since the first calibration routines all read the RAW format, and these routines are programmed in a generic manner, the cosmic-, pedestal-, time-, and laser-calibration could have been accomplished easily. Adding this calibration data to a `TofCal` file allowed to proceed to the LST-format. From this the Torte and Quirl detectors were time-calibrated. Using this up-to-date calibration data as input to the server program enabled to calculate the time-of-flight (→ β) *online*. At TOF this was never accomplished before.

The online determination of the particle velocities was a tremendous aid during trigger-tuning, where the aim was on enhancing the reaction $pd \to {}^3He\ \omega$. A peculiarity of this reaction is that the (heavy) ${}^3He$ is slow compared to the light decay products (pions) of the ω meson, but has a large energy in the laboratory frame. Displaying the QDC-conversion in the Calorimeter (energy) against the velocity (β), made it possible to observe *truly online* the influence of even small changes to the trigger. An online picture of two different trigger settings is shown in Fig. A.2.

The Online GUI

To establish the GUI (the `HistoViewer`), the DOM uses the “built in” ROOT features `TDialogCanvas`, `TH1F`, `TH2F`, `TCanvas`, and `TPave`. It is started by typing `rootn.exe`[4] in a shell on the online computer and then following the instructions given on the

---

[4] Note: `rootn`.exe instead of `root`. This accounts for the use of `libNew.so` needed by the memory-mapped file (`TMap`).

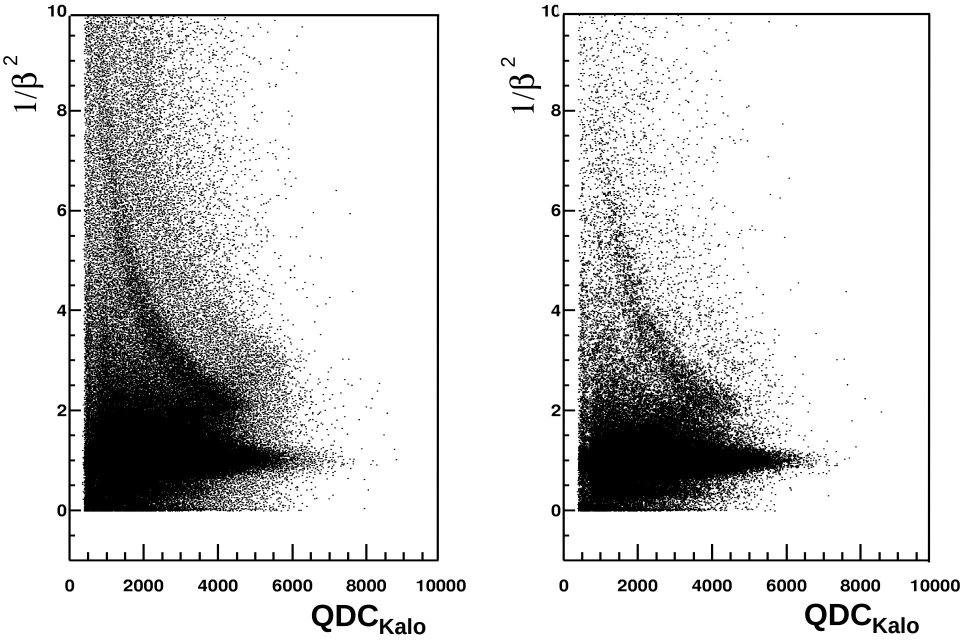

Figure A.2: *The DOM combined with the standardized calibration routines enables a quick calibration of the detector which leads to* online time-of-flight *monitoring. The energy deposit (QDC conversion) in the Calorimeter is plotted against* $1/\beta^2$*. Two different trigger settings are shown; in the left picture, a larger enhancement of* slow *particles with* high energy *is clearly visible.*

screen. The online GUI can interactively display all "standard histograms", either in "single mode" (one by one) or always 16 at a time. In addition, the user can announce user-defined histograms (added to the server) to the GUI easily by editing a self-explanatory script (`histo_viewer.C`). A "screen-shot" of the interactive GUI and 16 Barrel QDC-histograms are shown in Fig. A.3.

Once the server is running, there is no limitation to the number of online-viewers. Each physicist who has access to the online computer can log-in (remotely) and inspect the current status of the experiment. Another interesting feature of the GUI is the *automatic* conversion of *all histograms*, standard and user-defined, into (encapsulated) postscript files. The names of these files consist of a standardized 'name-body' and the current time and date (e.g. `tdcTorte_10h55m_12.5.2004.ps`). Executed once a day, this feature leads to an easy and very efficient way of creating log-histograms[5]. A LaTeX-file collects all histograms in a "histo-book", including a front page, a chapter for each subdetector, a table of contents, and a table of figures.

---

[5] Storing all histograms used to be the work assigned to the night-shift and took about two to four hours.

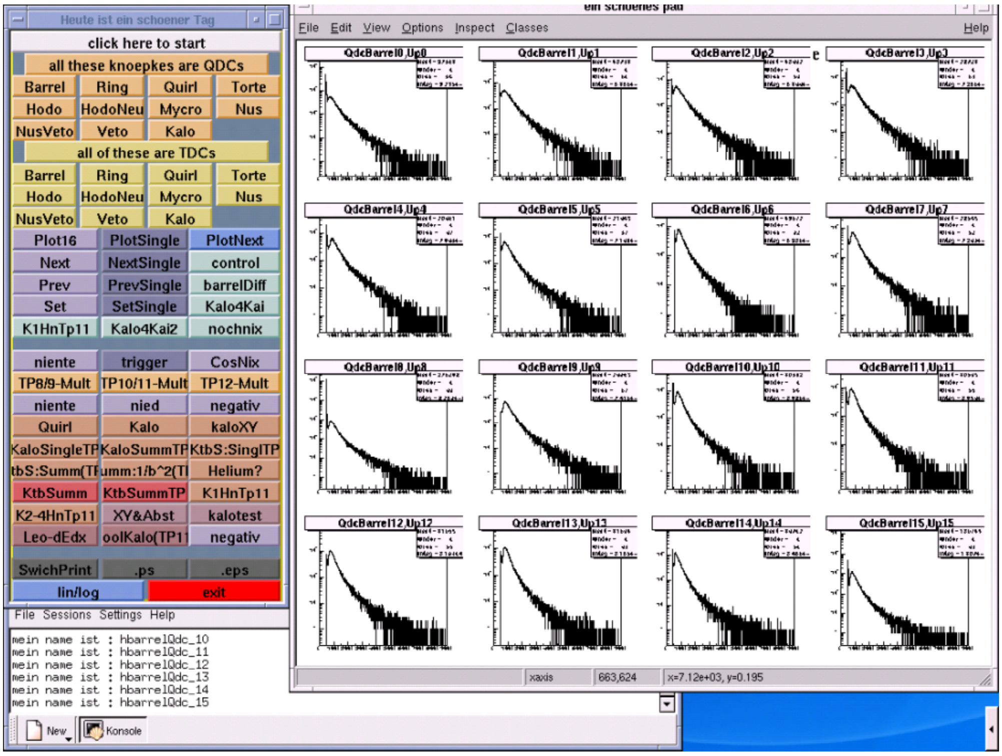

```
mein name ist : hbarrelQdc_10
mein name ist : hbarrelQdc_11
mein name ist : hbarrelQdc_12
mein name ist : hbarrelQdc_13
mein name ist : hbarrelQdc_14
mein name ist : hbarrelQdc_15
```

Figure A.3: *A "screen-shot" of the DOM. To the left the user-GUI is shown. Using the provided buttons all "standard" and user-defined histograms are displayed. Sixteen QDC spectra of the Barrel are shown at the right. In the shell where the viewer was originally started (bottom left) log-output is visible.*

Technical Specifications

The DOM is currently installed on a 1.9 GHz, 528 MB RAM Linux[6] machine with ROOT 3.10.01 installed. At present, it monitors about 2600 one-dimensional (≈4000 channels each) and 150 two-dimensional (≈400×400 channels each) histograms. With the current setup, the server uses about 150 MB of RAM, hence increasing the amount of histograms is not a problem.

Depending upon the size of each event transmitted by the DAQ the event-rate is between 30 and 600 $events/s$. These specifications are valid for pedestal calibration measurements and beamtime data, respectively. This is comparable with the speed of the DAQ itself, so that the installed computing power suffices for online monitoring.

Further Developments

Monitoring the plain QDC/TDC conversions separately confirms weather a channel contributes to the overall data stream. However the resulting one-dimensional histograms only provide rough information about the performance of this channel, and

---

[6] SuSE7.3, kernel2.4

almost no information about its stability. Therefore additional 2-dimensional correlation histograms (e.g. TDC vs. QDC) are needed[7].

Further "online" calibration along with conversion of (quasi) online data up to the CAL level, will allow the monitoring of actual physical observables, i.e. a fast look at the desired channel. Comparing this output with different trigger patterns will then permit a *fine tuning* of the trigger settings. Monitoring the elastic scattering will serve to detect acceptance deficiencies and to have a first estimate of the luminosity, and it will provide information about the actual beam distribution within the target (see Fig. 1.3). These features will be implemented in the near future (next beamtime: spring 2004).

In addition, a monitoring of the calibration parameters itself (offsets, parameters, calibration functions) is most desirable. This would be a very precise and sensitive instrument to monitor the sanity and stability of the whole system. Finally, it is investigated of how to implement an automatic feedback with the DAQ system (setting high-voltage, monitoring DAQ parameters).

---

[7] Many 2-dimensional histograms already are implemented as "user-histograms", i.e. they are declared, defined, and filled in the "user functions". The next step is to add them to the "official" part of the implementation.

Appendix B

Data Summary

In the following, the numerical values which lead to the distributions shown in Fig. 7.12 and Fig. 7.13 will be presented.

Angular Distribution of the ω Meson with Respect to the Beam Axis

Angular Distribution of $pp \longrightarrow pp\omega$		
$cos(\vartheta^{\omega}_{CMS})$	$d\sigma/d\Omega$ $[\mu/\mathrm{sr}]$ $(p_b = 2950\,MeV/c)$	$d\sigma/d\Omega$ $[\mu/\mathrm{sr}]$ $(p_b = 3200\,MeV/c)$
0.05	0.69 ± 0.21	1.69 ± 0.35
0.15	0.85 ± 0.19	1.71 ± 0.31
0.25	0.67 ± 0.18	1.46 ± 0.37
0.35	0.86 ± 0.17	2.07 ± 0.32
0.45	0.52 ± 0.16	1.45 ± 0.29
0.55	0.59 ± 0.15	2.04 ± 0.29
0.65	0.58 ± 0.16	1.48 ± 0.29
0.75	0.59 ± 0.19	2.13 ± 0.33
0.85	0.90 ± 0.17	2.57 ± 0.35
0.95	0.55 ± 0.17	2.94 ± 0.29

Table B.1: *Numeric values of the angular distribution of the ω-meson in the reaction $pp \rightarrow pp\omega$ at $p_{beam} = 2950\,MeV/c$ and $p_{beam} = 3200\,MeV/c$ (see Fig. 7.12).*

Invariant Mass Distribution of the $p\omega$ System

Invariant Mass Distribution of $\boldsymbol{pp \to pp\omega}$		
$M_{p\omega} [MeVc^2]$	$d\sigma/dM_{p\omega}$ [a.u.] $(p_b = 2950\,MeV/c)$	$d\sigma/dM_{p\omega}$ [a.u.] $(p_b = 3200\,MeV/c)$
1707.5	0	0
1722.5	$387.8 \pm 103.0^{+426.6}_{-38.8}$	$94.5 \pm 94.5^{+425.4}_{-0}$
1737.5	$1401.4 \pm 129.6^{+420.4}_{-140.1}$	$1592.7 \pm 164.4^{+796.3}_{-318.5}$
1752.5	$990.5 \pm 150.9^{+198.1}_{-99.1}$	$1754.4 \pm 190.3^{+877.3}_{-350.9}$
1767.5	$1346.3 \pm 149.1^{+134.6}_{-134.6}$	$1571.6 \pm 182.0^{+471.5}_{-157.2}$
1782.5	$1448.1 \pm 152.8^{+144.8}_{-144.8}$	$1637.1 \pm 397.0^{+163.7}_{-163.7}$
1797.5	$1153.0 \pm 135.5^{+115.3}_{-115.3}$	$2081.7 \pm 446.5^{+208.2}_{-208.2}$
1812.5	$349.3 \pm 84.6^{+34.9}_{-34.9}$	$1816.4 \pm 192.7^{+181.6}_{-181.6}$
1827.5	0	$2158.4 \pm 188.6^{+215.8}_{-215.8}$
1842.5	0	$1855.8 \pm 182.7^{+185.6}_{-185.6}$
1857.5	0	$1829.1 \pm 183.6^{+182.9}_{-182.9}$
1872.5	0	$1459.7 \pm 158.7^{+146.0}_{-146.0}$
1887.5	0	$432.5 \pm 110.2^{+43.3}_{-43.3}$
1902.5	0	0

Table B.2: *Numeric values of the invariant mass distribution ($p\omega$) for $pp \to pp\omega$ at $p_{beam} = 2950\,MeV/c$ and $p_{beam} = 3200\,MeV/c$ (see Fig. 7.13).*

List of Figures

List of Tables

Bibliography

[Alb97] The EDDA collaboration, D. Albers *et al.*,, *"Proton-proton elastic scattering excitation functions at intermediate energies"*, Phys. Rev. Lett. **78**, 1652 (1997).

[All99] C. E. Allgower *et al.*, *"Angular dependence of the pp elastic-scattering analyzing power between 0.8 and 2.8 GeV"*, Phys. Rev. C **60**, 054001/054002 (1999).

[Alt00] M. Altmeier *et al.*, *"Excitation functions of the analyzing power in pp scattering from 0.45 to 2.5 GeV"*, Phys. Rev. Lett. **85**, 1819 (2000).

[Ams98] C. Amsler *et al.*, *"Proton-antiproton annihilation and meson spectroscopy with the Crystal Barrel"*, Rev. Mod. Phys. **70**, 1265 (1998).

[And71a] H. L. Anderson *et al.*, *"Cross sections for* $pp \to d\rho^+$ *from 4.0 to* $12.3\,GeV/c$ *and a search for the* Δ^+*"*, Phys. Rev. Lett. **26**, 1971 (108).

[And71b] H. L. Anderson *et al.*, *"Forward differential cross sections for the reaction* $pp \to d\pi^+$ *in the Range* $3.4 - 12.3\,GeV/c$*"*, Phys. Rev. D **3**, 1536 (1971).

[And74] H. L. Anderson *et al.*, *"Measurements of the differential cross section of the reaction* $pp \to d\pi^+$ *from 3.0 to* $5.0\,GeV/c$*"*, Phys. Rev. D **9**, 580 (1974).

[ANKE02] The ANKE collaboration, COSY, *"ϕ-meson production in proton-proton collisions"*, URL: *http://www.fz-juelich.de/ikp/anke/doc/Proposals.shtml.*

[Arn93] R. A. Arndt *et al.*, *"Analysis of the reaction* $\pi^+ d \to pp$ *to* $500\,MeV/c$*"*, Phys. Rev. C **48**, 1926 (1993).

[Arn97] R. A. Arndt *et al.*, Phys. Rev. C **58**, 3005 (1997).

[Bal98] The DISTO collaboration, F. Balestra *et al.*, *"Production of* ϕ *and* ω *meson near threshold in pp reactions at* $p_{lab} = 3.67\,GeV/c$*"*, Phys. Rev. Lett. **81**, 4572 (1998).

[Bal01] F. Balestra *et al.*, DISTO collaboration, *"ϕ and ω meson production in pp reactions at* $p_{lab} = 3.67\,GeV/c$*"*, Phys. Rev. C **63**, 024004 (2001).

[Bal02] The DISTO collaboration, F. Balestea *et al.*, *"ρ^0 Meson production in the* $pp \to pp\pi^+\pi^-$ *reaction at* $3.67\,GeV/c$*"*, Phys. Rev. C **89**, 092001-1 (2002).

[Bar88] D. B. Barlow *et al.*, *"Measurement of the spin correlation parameters A(Ll) And A(Sl) for the reaction* $pp \rightarrow d\pi^+$ *in the energy region* $500\,MeV$ - $800\,MeV$*"*, Phys. Rev. C **37**, 1977 (1988).

[Ber85] R. Bertini *et al.*, *"A strong energy dependence of the analyzing power in the* $pp \rightarrow d\pi^+$*reaction and the question of an isovector dibaryon resonance"*, Phys. Lett. B **162**, 77 (1985).

[Ber88] R. Bertini *et al.*, *"A strong energy dependence of the analyzing power in the* $pp \rightarrow d\pi^+$*reaction and the question of an isovector dibaryon resonance (2)"*, Phys. Lett. B **203**, 18 (1988).

[Bet96] K. Bethge "*Kernphysik - Eine Einführung*", Springer-Verlag, 1996.

[Bet01] The GEM collaboration, M. Betigeri *et al.*, *"Differential cross sections measurement for the* $pp \rightarrow d\pi^+$ *reaction at* $850\,MeV/c$*"*, Phys. Rev. C **63**, 044011 (2001).

[Böh98] A. Böhm. *"Einsatz eines Neutronendetektors am COSY-TOF-Spektrometer"*, Ph.D. thesis, TU-Dresden, Dresden, Germany, 1998.

[Böh00] A. Böhm *et al.*, *"The COSY-TOF barrel detector"*, Nucl. Inst. Meth. A **443**, 238 (2000).

[Bri01] The COSY-TOF collaboration, S. Abd El-Samad and K.T. Brinkmann *et al.*, *"Production of* ω *mesons in proton-proton collisions"*, Phys. Lett. B **522**, 16 (2001).

[Bri02] K.T. Brinkmann, *"Mesonenproduktion im Proton-Proton Stoss"*, Habilitation thesis, TU-Dresden, Dresden, Germany, 2002. URL: *http://www.fz-juelich.de/ikp/COSY-TOF/publikationen/index.html.*

[Bro91] G.E. Brown and M. Rho, *"Scaling effective Lagrangians in a dense medium"*, Phys. Rev. Lett. **66**, 2720 (1991).

[Bru95] René Brun and Fonds Rademakers, *"An object-oriented data analysis framework"*, URL: *http://root.cern.ch.*

[Bru97] R. Brun, *"ROOT - An interactive OO-framework and its application to NA49 data analysis"*,
URL: *http://na49info.cern.ch/cgi-bin/wwwd-util/NA49/NOTE?122.*

[Bys98] J. Bystricky, C. Lechanoine-LeLuc, F. Lehar, *"Direct reconstruction of pp elastic scattering amplitudes and phase shift analyses at fixed energies from 1.80 to 2.70 GeV"*, Eur. Phys. J. C **4**, 607 (1998).

[Cap94] S. Capstick and W. Roberts, *"Quasi-two-body decays of nonstrange baryons"*, Phys. Rev. D **49**, 4570 (1994).

[CELSIUS] The CELSIUS/WASA collaboration, The Svedberg Laboratory, Uppsala, Sweden, URL: *http://lora.tsl.uu.se/wasa/* .

[CER95] CERES collaboration, G. Agakichiev *et al.*, Phys. Rev. Lett. **75** 1272 (1995); HELIOS collaboration, M. Masera *et al.*, Nucl. Phys. **A590** 93c (1995); DLS collaboration, W. K. Wilson *et al.*, Phys. Rev. C **57** 1865 (1998); HADES collaboration, J. Friese *et al.*, Nucl. Phys. **A654** 1017c (1999);

[COSY] U. Bechstedt, J. Dietrich, L.H.A. Leunissen, R. Maier, D. Prasuhn, A. Schnase, H. Schneider, *"The Cooler Synchrotron COSY"*, Beam Dynamics Newsletter **13**, 39 (1997).

[Dah95] M. Dahmen, *"Das Flugzeitspektrometer an COSY: Ein Detektor zur exklusiven Messung von Mehrteilchenreaktionen"*, Forschungszentrum Jülich, Bericht der KFA - 3140 (1995).

[Dro96] The GEM collaboration, M. Drochner *et al.*, *"Total and differential cross sections of* $pp \rightarrow d\pi^+$ *reactions down to* $275\,keV$ *above threshold"*, Phys. Rev. Lett. **77**, 454 (1996).

[EDD97b] The EDDA collaboration, mailto: *edda-data@iskp.uni-bonn.de.*

[Ell00] J. Ellis *et al.*, *"Hadronic probes of the polarized intrinsic strangeness of the nucleon"*, Nucl. Phys. A **673**, 256 (2000).

[EMS] Zentrallabor für Elektronik (FZ-Jülich), *"EMS - Das DAQ-System für COSY-Experimente"*, URL: *http://www.fz-juelich.de/zel/cosyda.htm.*

[Fel91] A. Feltham *et al.*, *"Spin transfer measurements of the* π^+d *(polarized)* $\rightarrow pp$ *(polarized) reaction spanning the* Δ *resonance"*, Phys. Rev. Lett. **66**, 2573 (1991).

[Fil00] A. Filippi *et al.*, *"Violation of OZI rule in* ϕ/ω *measurements with OBELIX at LEAR"*, Act. Phys. Pol. **31**, 2459 (2000).

[Fla84] V. Flaminio *et al.*, *"Compilation of cross sections III:* p *and* $\overline{p}$ *induced reactions"*, CERN-HERA 84-10, (1984).

[Fri01] M. Fritsch. priv. comm., (2001).

[Fri02] M. Fritsch, *"Assoziierte Strangnessproduktion in den Reaktionen* $pp \rightarrow pK^+\Lambda^0$ *und* $pp \rightarrow pK^+\Sigma^0$ *am COSY-Flugzeitspektromenter"*, Ph.D. thesis, University of Erlangen, Erlangen, Germany, (2002).

[Fuc03] C. Fuchs *et al.*, *"Off-shell* ω *production in proton-proton collisions near threshold"*, Phys. Rev. C **67**, 025202 (2003).

[Gla84] G. Glass *et al.*, *"Measurements of spin correlation parameter* $A(Nn)$ *and analyzing power at* $90°$ *for* $\overrightarrow{p}\,\overrightarrow{p} \rightarrow d\pi^+$ *between* $500\,MeV$ *and* $800\,MeV$*"*, Phys. Rev. Lett. **53**, 1984 (1984).

[Hai96] J. Haidenbauer, Ch. Hanhart and J. Speth, *"Threshold meson production in nucleon-nucleon collisions"*, Acta Phys. Polonica B **27**, 2893 (1996).

[Han03] Ch. Hanhart, priv. comm., (2003).

[Has99] A. Hassan, K.-Th. Brinkmann, E. Kuhlmann, K. Kilian, W. Oelert, E. Roderburg, *"A multi-functional cryo target for the external COSY experiments"*, Nucl. Inst. Meth. A **425**, 403 (1999).

[Hat92] T. Hatsuda *et al.*, *"QCD sum rules for vector mesons in the nuclear medium"*, Phys. Rev. C **46**, R34-R38 (1992).

[Hib99] F. Hibou *et al.*, *"Near-threshold production of ω mesons in the $pp \rightarrow pp\omega$ reaction"*, Phys. Rev. Lett. **83**, 492 (1999).

[Hor94] C.J. Horowitz *et al.*, *"Role of heavy-meson exchange in pion production near threshold"*, Phys. Rev. C **49**, 1337 (1994).

[IUCF] IUCF: **I**ndiana **U**niversity **C**yclotron **F**acility, Bloomington, Indiana, USA
URL: *http://www.iucf.indiana.edu.*

[Isg79] N. Isgur and G. Karl, *"Positive-parity excited baryons in a quark model with hyperfine interactions"*, Phys. Rev. D **19**, 2653 (1979).

[Jac01] B. Jakob, *"Untersuchung von Proton-Proton-Reaktionen an der Pion-Produktionsschwelle mit dem COSY-TOF-Spektrometer"* Ph.D. thesis, TU-Dresden, Dresden, Germany, 2001.

[Jae92] V. Jaekle, *"Aufbau eines Flüßig-Wasserstoff-Targets mit extrem dünnen Fenstern"*, Diploma Thesis, University of Bonn, Bonn, Germany, (1992).

[Jäk03] R. Jäkel, *"Überlegungen zur Mesonenproduktion bei der Proton-Deuteron-Fusion an COSY-TOF"*, Diploma Thesis, TU-Dresden, Dresden, Germany, (2003),
URL: *http://www.fz-juelich.de/ikp/COSY-TOF/publikationen/index.html.*

[Kar99] L. Karsch, *"Bestimmung der Ansprechwahrscheinlichkeit des Neutronendetektors COSYnus"*, Diploma Thesis, TU-Dresden, Dresden, Germany, (1999),
URL: *http://www.fz-juelich.de/ikp/COSY-TOF/publikationen/index.html.*

[Kar04] L. Karsch, *"Bestimmung der Wirkungsquerschnitte $pp \rightarrow nK^+\Sigma^+$ und $pp \rightarrow pK^0\Sigma^+$ im Proton-Proton Stoss"*, Ph.D. thesis (in preparation), TU-Dresden, Dresden, Germany, 2004,
URL: *http://www.fz-juelich.de/ikp/COSY-TOF/publikationen/index.html.*

[Kil98] K. Kilian *et al.*, *"Physik am Kühlersynchrotron COSY"*, Physikalische Blätter **10**, 911 (1998).

[Koi93] Y. Koike *et al.*, *"Pattern of chiral restoration at low temperature from QCD sum rules"*, Phys. Rev. D **47**, 1225 (1993).

[Kra88] K.S. Krane, *"Introductory Nuclear Physics"*, John Wiley & Sons, (1988).

[Koh80] R. Koniuk and N. Isgur, *"Baryon decays in a quark model whith chomodynamics"*, Phys. Rev. D **21**, 1886 (1980). *Erratum:*Phys. Rev. D **23** 818 (1981)

[Kre03] J.Kress, *"Entwicklung und Installation eines Zentralkalorimeters und Messungen der Reaktion* $pp \rightarrow pp\pi^+\pi^-$ *mit spin-polarisierten Protonen am Flugzeitspektrometer COSY-TOF"*, Ph.D. thesis, University of Tübingen, Tübingen, Germany, (2003).

[Leo94] W.R. Leo, *"Techniques for Nuclear and Particle Physics Experiments"*, Springer-Verlag, 2^{nd} edition, (1994).

[LasV] S. Brand, *"Entwicklung eines MC-Programmes für COSY-TOF"*, Ph.D. thesis, University of Bochum, Bochum, Germany, 1995;
U. Zielinski, *"Analyse- und Simulationsmethoden zur Analyse der* $pp\gamma$*-Reaktion an COSY-TOF"*, Ph.D. thesis, University of Bochum, Bochum, Germany, 1998.

[Loc70] W.O. Lock and D.F. Measday, *"Intermediate energy nuclear physics"*, London: Methuen (1970).

[Mac89] R. Machleidt, *"The meson theory of nuclear forces and nuclear structure"*, Adv. Phys. **19**, 189 (1989).

[Mac99] H. Machner and J. Haidenbauer, *"Topical Review: Meson production close to threshold"*, J. Phys. G: Nucl. Part. Phys. **25**, R231 (1999).

[Mac01] R. Machleidt and I. Slaus, *"The nucleon-nucleon interaction"*J. Phys. G.: Nucl. part. Phys. **27**, 69 (2001) and references therin.

[May84] T. Mayer-Kuckuk, *"Kernphysik - Eine Einführung"*, B. G. Teubner, (1984).

[Mic98] P. Michel *et al.*, *"MARS: A start detector system for the COSY Time-Of-Flight spectrometer TOF"*, Nucl. Inst. Meth. A **408**, 453 (1998).

[Nak98] K. Nakayama, A. Szczurek, C. Hanhart, J. Haidenbauer, and J. Speth, *"Production of* ω *meson in proton-proton collisions"*, Phys. Rev. C **57**, 1580 (1998).

[Nake93] C.J. Nake, *"Optimierung eines Flüssig-Wasserstoff/Deuterium-Targets mit äußerst dünnen Folienfenstern"*, Diploma Thesis, University of Bonn, Bonn, Germany, (1993)

[Nis78] J. Niskanen, *"The differential cross section and polarization in* $pp \rightarrow d\pi^+$*"*, Nucl. Phys. A **298-3**, 417 (1978).

[Nis96] J. Niskanen, *"Comment on 'Role of heavy-meson exchange in pion production near threshold' "*, Phys. Rev. C **53**, 526 (1996).

[Oh01] Y. Oh, A. I. Titov, T. S. H. Lee, *"Nucleon resonances in* ω *photoproduction"*, Phys. Rev. C **66**, 025201 (2001).

[PANDA] The PANDA experiment at GSI,
URL: *http://www.gsi.de/zukunftsprojekt/experimente/hesr-panda/index_e.html.*

[Pan03] S. Panacek *et al.*, *"ROOT - Users Guide 3.5"*
URL: *http://root.cern.ch/root/RootDoc.html.*

[PAW] PAW : **P**hysics **A**nalysis **W**orkstation, URL: *http://paw.web.cern.ch/paw/.*

[PDG] Particle Data Group, R.M. Barnett *et al.*, Phys. Rev. D **66** 1 (2002).

[Pen02a] G. Penner, U. Mosel, *"Vector meson production and nucleon resonance analysis in a coupled-channel approach for energies* $m_N < \sqrt{s} < 2\,GeV$*. I. Pion-induced results and hadronic parameters"*, Phys. Rev. C **66**, 055211 (2002).

[Pen02b] G. Penner, U. Mosel, *"Vector meson production and nucleon resonance analysis in a coupled-channel approach for energies* $m_N < \sqrt{s} < 2\,GeV$*. II. Photon-induced results"*, Phys. Rev. C **66**, 055212 (2002).

[Phi94a] Philips Photonics, *Photomultiplier Tubes - Principles & Applications*, 1994.

[Phi94b] Philips Photonics, *Data Handbook Photomultiplier*, 1994.

[PLUTO] M.A. Kagarlis, GSI, *"Pluto++, A Monte Carlo simulation tool for hadronic physics"*, GSI Report **3** (2000),
URL: *http://www-hades.gsi.de/computing/pluto/html/pluto.html.*

[Ply99] R. G. Pleydon *et al.*, *"Inclusive measurements of the* $pp \rightarrow pn\pi^+$ *reaction at* $420\,MeV$ *and* $500\,MeV$*"*, Phys. Rev. C **59**, 3208 (1999).

[Pow59] C.F. Powell, P.H. Fowler, and D. H. Perkins, *"The Study of Elementary Particles by the Photographic Method"*, New York: Pergamon, 1959; C. F. Powell, Rep. Prog. Phys. **13**, 350 (1950).

[Pra01] D. Prasuhn, priv. comm., (2001).

[R1450] Manual R1450, URL: *http://usa.hamamatsu.com/hcpdf/parts_R/R1450.pdf.*

[Rat98] F. Rathmann *et al.*, *"Complete angular distribution measurements of pp spin correlation parameters* A_{xx}*,* A_{yy}*, and* A_{xz} *and analyzing power* A_y *at* $197.4\,MeV$*"*, Phys. Rev. C **58**, 658 (1998).

[Rin95] Peter Ringe, *"Datenerfassung und Testmessungen an Detektorkomponenten für Mittelenergiephysik-Experimente"*, Ph.D. thesis, University of Bochum, Bochum, Germany, (1995).

[Sah83] A. Saha, K. K. Seth, D. Kielczewska, S. Iversen, M. Kaletka, D. Barlow and D. Smith, *"Energy variation of the analyzing power in the reaction* $\vec{p}p \rightarrow d\pi^+$*"*, Phys. Rev. Lett. **51**, 759 (1983).

[Schoe97] P. Schoenmeier, *"Erweiterung der Datenerfassungssoftware für das COSY-TOF-Spektrometer"*, Diploma Thesis, TU-Dresden, Dresden, Germany, (1997).

[Schr98] W. Schroeder, *"Entwicklung und Bau eines Vetodetektorsystems für das COSY-TOF Experiment am Forschungszentrum Jülich", Diploma Thesis, University of Erlangen, Erlangen, Germany, (1998).*

[Schu01] M. Schulte-Wissermann, "The use of ROOT in Nuclear Physics", ROOT 2001 workshop, Fermi National Accelerator Laboratory, (2001), URL: *http://www-root.fnal.gov/root2001/R2001Program.html.*

[Sco01] W. Scobel for the EDDA collaboration, *"Elastic pp scattering: The internal storage ring experiment EDDA and its inpact on phase shift analyzes"*, Nucl. Phys. News **11**, 4 (2001).

[Sib96] A.A. Sibirtsev, *"Heavy-meson production cross sections from proton-proton collisions"*, Nucl. Phys. A **604**, 455 (1996).

[Sib03] A.A. Sibirtsev, priv. comm., (2003).

[Ste95] M.Steinke, H.Brand, COSY-TOF-notes, Bo, 4.2 1994.

[Sto98] H. Stockhorst *et al.*, *"Longitudinal and transverse stochastic beam cooling at COSY"*, COSY NEWS **3**, 7 (1998).

[Tit00] A. I. Titov, B. Kämpfer, B. L. Reznik; *"Production of ϕ mesons in near-threshold πN and NN reactions"*, Eur. Phys. J. A **7**, 543 (2000).

[Tit02a] A. I. Titov, B. Kämpfer, and B. L. Reznik; *"Production of ω and ϕ mesons in near-threshold πN reactions: Baryon resonances and the OZI-rule"*, Phys. Rev. C **65**, 065202 (2002).

[Tit02b] A. I. Titov, T. -S. H. Lee; *"Effective Lagrangian approach to the ω photoproduction near threshold"*, Phys. Rev. C **66** 015204 (2002).

[Ull04] W. Ullrich, Diploma Thesis (in preparation), TU-Dresden, Dresden, Germany, (2004).

[Tsu03] K. Tsushima, K. Nakayama, *"Near threshold ω and Φ meson productions in pp collisions"*, Phys. Rev. C **68**, 034612 (2003).

[Wag97] M. Wagner, *"Entwicklung und Bau eines intermediären Szintillatorfaser-Hodoskops für COSY-TOF"*, Diploma Thesis, University of Erlangen, Erlangen, Germany, (1997).

[Wag02] M. Wagner, *"Assoziierte Strangness-Produktion in der Reaktion $pp \rightarrow pK^0\Sigma^+$ am COSY-Flugzeitspektrometer"*, Ph.D. thesis, University of Erlangen, Erlangen, Germany, (2002).

[Yon93] J. Yonnet *et al.*, *"Measurements of angular distributions of differential cross-sections and analyzing powers of the reaction polarized $pp \rightarrow d\pi^+$ between 1.3-GeV and 2.4-GeV"*, Nucl. Phys. A **562**, 352 (1993).

[Yuk35] H. Yukawa, *"On the interaction of elementary particles"*, Proc. Phys. Math. Soc. Jap. **17**, 48 (1935).

[Zha98] Q. Zhao and Z. Li, *"Vector meson photoproduction with an effective Lagrangian in the quark model"*, Phys. Rev. C **58**, 2393 (1998).

[ZEUS03] The ZEUS collaboration, *"Observation of the strange sea in the proton via inclusive ϕ meson production in neutral current deep inelastic scattering at HERA"*, Phys. Lett. B **553**, 141 (2003).

[Zwe64] G. Zweig, CERN Report **8419/Th**, 412 (1964); S. Okubo, Phys. Lett. **5**, 165 (1965); I. Iizuka, Prog. Theor. Phys. Suppl. **37-38**, 21 (1966).

Danksagung

Eine Doktorarbeit ist immer das Ergebnis langer und intensiver Anstrengungen, welche ohne die Unterstützung des privaten und “institutionellen” Umfeldes nicht möglich wäre. Auch ich bin zutiefst dankbar, eine große Unterstützung während der gesamten Zeit erfahren zu haben. Beginnen möchte ich mit meiner Freundin Melanie, die es wahrlich nicht leicht hatte mit mir und meiner Arbeit. Die freie Zeit war immer sehr begrenzt, und ich danke ihr, daß sie nie das Lächeln verloren hat - was auch immer geschehen ist. Meinen Eltern gebührt natürlich der zweite Dank, denn sie sind ursächlich verantwortlich für meine Existenz, und ich spüre langsam, wie sehr ich durch ihre Erziehung zu dem Menschen geworden bin, der heute diese Zeilen schreiben darf. Ihre moralische Unterstützung meines Studiums sowie der Promotionszeit ist unbeschreiblich. Und ich hoffe nie wirklich erwachsen zu werden, um diese Unterstützung noch viele Jahre weiter genießen zu können. Meine Geschwister sind an dieser Stelle auch zu nennen, denn sie haben in der gleichen Zeit “ihre” Arbeiten gemacht und stehen nun ebenfalls vor dem süßen dekadenlangen Arbeitsleben. Auch wenn ich sie durch die räumliche Trennung selten sehe, so sind sie doch immer bei mir - so wie ich bei ihnen bin. Und wenn wir uns dann mal treffen, so ist es immer so, als wäre man niemals auseinander gegangen. Schließlich möchte ich noch meiner Omi danken. Sie hat mich wohl am meisten inspiriert nicht Kraftfahrer zu werden, sondern mich auf meine eigentlichen Stärken zu besinnen. Und ich widme diese Arbeit ihr, denn wäre dieser verdammte Krieg nicht gewesen, so wäre sie sicherlich Chemikerin - und damit die erste Naturwissenschaftlerin unserer Familie - geworden. Meinem Opa danke ich ebenfalls für seinen prägenden Einfluß. Er wäre heute sicherlich sehr stolz, jetzt, hier auf Erden.

Zuletzt noch meine Freunde, die ich sträflichst vernachlässigt habe. Christian K., Christoph S., Ingo P., Jan-Peter K., Lars T., Oliver M. und noch viele andere: ihr habt euch nie beklagt, und die wenigen Stunden immer darauf verwendet, daß es voran gehen muß; mit dem Leben und dieser Arbeit. Peace euch allen - und immer schön hoch die Tassen!

Auf der wissenschaftlichen Seite muß der erste Dank meinem Doktorvater, Herrn Prof. H. Freiesleben, gelten. Es ist wohl nicht von der Hand zu weisen, daß ohne seine Unterstützung diese Arbeit nicht möglich gewesen wäre. Diese Unterstützung beginnt bei ganz pragmatischen Dingen: fehlende Hardware - kein Problem; fehlende Reisemittel - Lösung parat. Dazu der Führungsstil, welcher mir genügend Freiraum gelassen hat, mich konstruktiv und effizient meiner Arbeit widmen zu können. Aber das wichtigste war sein kritisches Interesse an allen meinen Handlungen und die prompten und substantiellen Hilfen bei allen meinen Fragen. Möge jeder Doktorand eine solche

Betreuung erfahren.

Kai Brinkmann, ja dir kann man auch nicht genug danken! In einem Zimmer zusammen hast Du mich geleitet, und beobachtet wie ich von einem “nichts-wissenden” Diplomanden zu einem “etwas-wissenden” Doktoranden wurde. Wie diese Arbeit ohne deine Korrekturen aussähe, das möchte ich mir wirklich nicht ausmalen. Und schließlich natürlich noch meinen Kollegen: GuoYan, Leo, Manfred, Martin, René und Solomon. Die letzen Jahre haben uns nicht nur bei TofRoot zu einem Team geformt, sondern uns auch die Systemadministration im “Kollektiv” beschert. Es ist so unglaublich erfrischend mit euch zu arbeiten, und nie hatten wir Streit wegen irgendwas. Den etwas “entfernteren” Kollegen Arthur, Daniel, Jochen, Mark, Miriam und Wolfgang soll nun auch noch Dank ausgesprochen werden. Entfernt waren wir eigentlich nur räumlich, und die gemeinsamen Strahlzeiten wird wohl niemand vergessen.

Und schließlich danke ich dem BMBF und dem FZ-Jülich, d.h. eigentlich der Summe aller Steuerzahler, dafür, daß ich mich in den letzten Jahren mit so etwas “weltfremden” wie der Mesonenproduktion beschäftigen durfte. Aber wer weiß, ohne die Untersuchungen des Herrn Karl Ferdinand Braun würdet ihr alle heute in eine ziemlich dunkle Röhre gucken.

Versicherung

Hiermit versichere ich, daß ich die vorliegende Arbeit ohne unzulässige Hilfe Dritter und ohne Benutzung anderer als der angegebenen Hilfsmittel angefertigt habe; die aus fremden Quellen direkt oder indirekt übernommenen Gedanken sind als solche kenntlich gemacht. Die Arbeit wurde bisher weder im Inland noch im Ausland in gleicher oder ähnlicher Form einer anderen Prüfungsbehörde vorgelegt.

Ich erkenne die Prüfungsordnung der Fakultät Mathematik und Naturwissenschaften (Technische Universität Dresden, in der Fassung vom 20.03.2000) ohne jegliche Einschrängung an.

Dresden, den 26.3.2004 Martin Schulte-Wissermann